

Correlated Polarity Noise Reduction:  
Development, Analysis, and Application of a Novel Noise Reduction Paradigm

By

Jered R Wells

Graduate Program in Medical Physics  
Duke University

Date: \_\_\_\_\_

Approved:

\_\_\_\_\_  
James T. Dobbins, III, Supervisor

\_\_\_\_\_  
Ehsan Samei

\_\_\_\_\_  
Joseph Y. Lo

\_\_\_\_\_  
Donald P. Frush

\_\_\_\_\_  
James E. Bowsher

Dissertation submitted in  
partial fulfillment of the requirements for the degree of  
Doctor of Philosophy in the Graduate Program in Medical Physics  
in the Graduate School of Duke University

2013

ABSTRACT

Correlated Polarity Noise Reduction:  
Development, Analysis, and Application of a Novel Noise Reduction Paradigm

By

Jered R Wells

Graduate Program in Medical Physics  
Duke University

Date: \_\_\_\_\_

Approved:

\_\_\_\_\_  
James T. Dobbins, III, Supervisor

\_\_\_\_\_  
Ehsan Samei

\_\_\_\_\_  
Joseph Y. Lo

\_\_\_\_\_  
Donald P. Frush

\_\_\_\_\_  
James E. Bowsher

An abstract of a dissertation submitted in  
partial fulfillment of the requirements for the degree of  
Doctor of Philosophy in the Graduate Program in Medical Physics  
in the Graduate School of Duke University

2013

Copyright by  
Jered R Wells  
2013

## **Abstract**

Image noise is a pervasive problem in medical imaging. It is a property endemic to all imaging modalities and one especially familiar in those modalities that employ ionizing radiation. Statistical uncertainty is a major limiting factor in the reduction of ionizing radiation dose; patient exposure must be minimized but high image quality must also be achieved to retain the clinical utility of medical images. One way to achieve the goal of radiation dose reduction is through the use of image post processing with noise reduction algorithms. By acquiring images at lower than normal exposure followed by algorithmic noise reduction, it is possible to restore image noise to near normal levels. However, many denoising algorithms degrade the integrity of other image quality components in the process.

In this dissertation, a new noise reduction algorithm is investigated: Correlated Polarity Noise Reduction (CPNR). CPNR is a novel noise reduction technique that uses a statistical approach to reduce noise variance while maintaining excellent resolution and a “normal” noise appearance. In this work, the algorithm is developed in detail with the introduction of several methods for improving polarity estimation accuracy and maintaining the normality of the residual noise intensity distribution. Several image quality characteristics are assessed in the production of this new algorithm including its effects on residual noise texture, residual noise magnitude distribution, resolution effects, and nonlinear distortion effects. An in-depth review of current linear methods for medical imaging system resolution analysis will be presented along with several newly discovered improvements to existing techniques. This is followed by the presentation of a new

paradigm for quantifying the frequency response and distortion properties of nonlinear algorithms. Finally, the new CPNR algorithm is applied to computed tomography (CT) to assess its efficacy as a dose reduction tool in 3-D imaging.

It was found that the CPNR algorithm can be used to reduce x ray dose in projection radiography by a factor of at least two without objectionable degradation of image resolution. This is comparable to other nonlinear image denoising algorithms such as the bilateral filter and wavelet denoising. However, CPNR can accomplish this level of dose reduction with few edge effects and negligible nonlinear distortion of the anatomical signal as evidenced by the newly developed nonlinear assessment paradigm. In application to multi-detector CT, XCAT simulations showed that CPNR can be used to reduce noise variance by 40% with minimal blurring of anatomical structures under a filtered back-projection reconstruction paradigm. When an apodization filter was applied, only 33% noise variance reduction was achieved, but the edge-saving qualities were largely retained. In application to cone-beam CT for daily patient positioning in radiation therapy, up to 49% noise variance reduction was achieved with as little as 1% reduction in the task transfer function measured from reconstructed data at the cutoff frequency.

This work concludes that the CPNR paradigm shows promise as a viable noise reduction tool which can be used to maintain current standards of clinical image quality at almost half of normal radiation exposure. This algorithm has favorable resolution and nonlinear distortion properties as measured using a newly developed set of metrics for nonlinear algorithm resolution and distortion assessment. Simulation studies and the initial application of CPNR to cone-beam CT data reveal that CPNR may be used to reduce CT dose by 40%-49% with minimal degradation of image resolution.

# Contents

Abstract.....	iv
List of Tables.....	xi
List of Figures.....	xii
List of Abbreviations .....	xv
Acknowledgements.....	xvi
1. Introduction .....	1
1.1 Imaging Dose Reduction Strategies .....	3
1.2 Image Processing Algorithms for Dose Reduction and SNR Improvement .....	4
1.3 Dissertation Objectives .....	6
2. Correlated Polarity Noise Reduction .....	8
2.1 Introduction to CPNR.....	8
2.2 Polarity Estimation .....	14
2.2.1 Polarity Accuracy .....	19
2.2.2 Supermajority Voting Strategy .....	25
2.2.3 High Variance Residual Thresholding .....	28
2.2.4 Low Magnitude Noise Thresholding .....	34
2.2.5 Polarity Estimation Optimization.....	38
2.3 Subtracted Noise Magnitude and Distribution.....	40
2.3.1 Subtracted Noise Distribution .....	41
2.3.2 Subtracted Noise Distribution Optimization .....	44
2.4 CPNR Application to Radiographic Images.....	48
2.4.1 NPS Analysis.....	50

2.4.2 Noise Texture Shaping by Frequency Blending.....	55
2.5 CPNR Benchmarking.....	60
2.5.1 Bilateral Filter.....	60
2.5.2 Wavelet Denoising.....	61
2.5.3 Denoising Algorithm Comparison.....	62
2.6 CPNR Benefits, Limitations, and Future Work.....	66
3. Linear Methods for Resolution Performance Analysis.....	69
3.1 The Modulation Transfer Function.....	70
3.2 1-D MTF Measurement Methods.....	72
3.2.1 Fine Sampling at Arbitrary Angle.....	72
3.2.2 Slit Non-Uniformity.....	74
3.2.3 Experimental Implementation with an Indirect Detection Device.....	76
3.2.3.1 Imaging System.....	76
3.2.3.2 Beam Conditions.....	77
3.2.3.3 Edge Image Acquisition.....	78
3.2.3.4 Edge Image Processing.....	78
3.2.3.5 Slit Image Acquisition.....	81
3.2.3.6 Slit Image Processing.....	82
3.2.4 Validation by Synthesis with a Hypothetical Direct Detection Device.....	83
3.2.4.1 2-D MTF Simulation.....	83
3.2.4.2 Non-Uniform Slit Simulation.....	85
3.3 MTF Measurement Results from Experimental Implementation.....	86
3.3.1 1-D MTF Measurements.....	86
3.3.2 2-D MTF Measurements.....	87

3.3.3 Slit-Based Measurements and Non-Uniformity Correction.....	89
3.4 Results from Validation by Synthesis.....	90
3.4.1 2-D MTF Estimation .....	90
3.4.2 Slit Non-Uniformity Correction .....	92
3.5 Discussion and Conclusions.....	93
4. Frequency Response and Distortion Properties in Nonlinear Image Processing .....	99
4.1 Current Nonlinear Resolution Assessment Strategies .....	100
4.2 Nonlinear Signal Distortion.....	101
4.3 Development of Novel Nonlinear Metrology .....	103
4.3.1 Sinusoid Response .....	103
4.3.2 Principle Frequency Response .....	105
4.3.3 Distortion Power Spectrum .....	105
4.3.4 Distortion Index.....	106
4.3.5 Summed (Integrated) Distortion Index .....	107
4.4 Experimental Evaluation.....	108
4.4.1 PFR .....	109
4.4.2 DPS .....	110
4.4.3 DI.....	111
4.4.4 $\Sigma$ DI .....	112
4.5 Application of Nonlinear Metrology to the Bilateral, Wavelet, and CPNR Filters.....	113
4.6 Discussion, Benefits, and Limitations .....	116
4.7 Conclusions and Future Directions.....	121
5. CPNR Application to Computed Tomography.....	124
5.1 Preliminary Simulation Studies of CPNR Applied to MDCT.....	126



5.1.1 MDCT and XCAT Simulation .....	126
5.1.2 CPNR Optimization in MDCT Projection Space.....	127
5.1.3 FBP Reconstruction from Cylindrical Detector Data.....	128
5.1.4 Preliminary Results.....	131
5.1.4.1 NPS Analysis.....	131
5.1.4.2 Artifact Analysis.....	135
5.2 CPNR Application to Cone-Beam CT for Patient Positioning in Radiation Therapy	137
5.2.1 CBCT Data Acquisition .....	138
5.2.2 Bowtie Filter Images.....	140
5.2.3 CPNR in CBCT Projection Space .....	142
5.2.4 FBP Reconstruction from FPD Data.....	142
5.2.4.1 Bowtie Filter and Crescent Artifact Correction .....	143
5.2.4.2 Short Scan Weighting Function .....	145
5.2.4.3 Rudimentary Scatter Nonuniformity Correction .....	146
5.2.5 Catphan Analysis .....	147
5.2.5.1 Radial NPS .....	147
5.2.5.2 High Contrast Resolution.....	152
5.2.5.3 Task Transfer Function.....	154
5.3 Discussion.....	158
6. Concluding Remarks.....	160
Appendix A: Synthesis of Digitized Slit and Edge Objects with System Blurring Effects .....	163
Appendix B: Plane Wave Windowing, Sampling, and Integration Over a Rectangular Aperture .....	166
Appendix C: Expansion of Digital Plane Wave Representation in the Spatial Domain.....	176

References .....	178
Biography.....	192

## List of Tables

Table 2.1: MATLAB validation of the CPNR concept.....	11
Table 2.2: MATLAB validation of the optimized CPNR concept.....	42
Table 2.3: Parameters and measurements from Figure 2.12.....	47
Table 2.4: Image frequency blending parameters.....	56
Table 3.1: Summary of values obtained from physical edge measurement.....	79
Table 3.2: Summary of values obtained from simulated edge measurement.....	85
Table 3.3: Comparison of ESF denoising techniques and 2-D interpolation methods.....	88
Table 3.4: Simulation results comparing different ESF denoising techniques and 2-D interpolation methods using absolute relative accuracy averaged over $u = v = [0, f_c]$ .....	92
Table 3.5: Simulation results comparing different ESF denoising techniques and 2-D interpolation methods using relative precision error averaged over $u = v = [0, f_c]$ .....	92
Table 5.1: CBCT clinical protocols and parameters.....	140
Table 5.2: Catphan material definitions.....	156

## List of Figures

Figure 1.1: Medical radiation exposure of patients in the early 1980s.....	2
Figure 1.2: Medical radiation exposure of patients in 2006.....	2
Figure 2.1: Iterative noise variance reduction by CPNR.....	13
Figure 2.2: Noise polarity estimation versus signal fitting.....	15
Figure 2.3: Directional sampling mask.....	16
Figure 2.4: Sample masks at various angles.....	18
Figure 2.5: Simulated chest radiograph images using the XCAT phantom.....	21
Figure 2.6: Polarity accuracy of the majority vote method.....	23
Figure 2.7: Polarity maps showing polarity distribution, correlation, and artifacts for various polynomial order and mask length combinations.....	24
Figure 2.8: Accuracy of majority vote method with supermajority constraints.....	26
Figure 2.9: Polarity maps generated using the supermajority voting strategy.....	27
Figure 2.10: Noise estimation bias at high contrast edges.....	28
Figure 2.11: Spatially adaptive variance-based weighting function.....	30
Figure 2.12: Polarity accuracy as a function of $t_W$ .....	32
Figure 2.13: Polarity maps showing artifact reduction by $t_W$ thresholding.....	33
Figure 2.14: Accuracy of $t_{RMSE}$ noise magnitude thresholding.....	36
Figure 2.15: Polarity accuracy of the majority vote method with $t_{RMSE}$ thresholding.....	37
Figure 2.16: Accuracy of CPNR with settings optimized for scale space denoising.....	40
Figure 2.17: Polarity maps corresponding to optimized CPNR protocols.....	40
Figure 2.18: Noise intensity distributions from Tables 2.1 and 2.2.....	43
Figure 2.19: Impact of polarity inaccuracy and Weibull noise distribution on CPNR.....	47
Figure 2.20: X ray image of the Kyoto phantom at normal clinical exposure.....	49

Figure 2.21: 1-D NPS measured from subtracted Kyoto phantom images. ....	51
Figure 2.22: NNPS analysis of CPNR-processed Kyoto phantom images. ....	53
Figure 2.23: CPNR-processed Kyoto phantom x ray images with log transform. ....	54
Figure 2.24: Bandpass filtering of CPNR-processed images. ....	57
Figure 2.25: NNPS of CPNR frequency blended results. ....	58
Figure 2.26: CPNR-processed results compared to third and full dose images. ....	59
Figure 2.27: Sample symlet wavelet .....	62
Figure 2.28: NNPS of CPNR compared to bilateral and wavelet denoising. ....	63
Figure 2.29: Comparison of processed and difference images across algorithms. ....	65
Figure 2.30: XCAT signal and noise power spectra. ....	67
Figure 3.1: Slit geometry.....	75
Figure 3.2: LSF following numerical differentiation of a finely sampled edge.....	80
Figure 3.3: Normalized LSF from a slit at $4.15^\circ$ .....	83
Figure 3.4: MTF measured from (nearly) horizontal and vertical slit and edge devices.....	87
Figure 3.5: 2-D MTF estimate based on ten edge measurements between $0^\circ$ and $90^\circ$ . ....	88
Figure 3.6: Comparison of slit-based MTF measurements from physical slits at two angles with and without slit non-uniformity correction. ....	90
Figure 3.7: 2-D MTF measured from a hypothetical direct-detection device using the proposed edge method.....	91
Figure 3.8: Slit-based MTF measurements using synthesized images from a hypothetical direct-detection device.....	93
Figure 4.1: Narrow-band demonstration of algorithm nonlinearity.....	102
Figure 4.2: MTF, PFR, and DPS analysis of a 5x5 box filter. ....	106
Figure 4.3: Image backgrounds for nonlinear algorithm resolution analysis. ....	109
Figure 4.4: PFR is shown at several combinations of CNR and image background. ....	110

Figure 4.5: DPS of the median filter. ....	111
Figure 4.6: DI varies as a function of CNR and image background. ....	112
Figure 4.7: $\Sigma$ DI plotted as a function of CNR for various background images.....	113
Figure 4.8: PFR characterization of bilateral, wavelet, and CPNR algorithms. ....	114
Figure 4.9: DPS characterization of bilateral, wavelet, and CPNR algorithms. ....	115
Figure 4.10: DI characterization of bilateral, wavelet, and CPNR algorithms. ....	116
Figure 4.11: Visualization of principle frequency contrast modulation and nonlinear distortion effects. ....	118
Figure 5.1: Ramp and apodized reconstruction filters.....	130
Figure 5.2: NPS measured from reconstructed XCAT liver images.....	133
Figure 5.3: Heart detail with and without CPNR processing.....	134
Figure 5.4: Comparison of XCAT chest CT reconstruction images.....	136
Figure 5.5: Varian OBI system.....	139
Figure 5.6: Full fan (half scan) acquisition geometry. ....	139
Figure 5.7: Bowtie filter image.....	141
Figure 5.8: Bowtie and crescent artifact correction.....	145
Figure 5.9: Rudimentary scatter anisotropy correction.....	147
Figure 5.10: 2-D NPS measurement from Catphan data.....	150
Figure 5.11: NPS measured from uniform module of Catphan phantom. ....	150
Figure 5.12: Catphan noise textures. ....	151
Figure 5.13: High contrast resolution module analysis.....	153
Figure 5.14: TTF measured from three sensitometry inserts.....	157
Figure A.1: Depiction of variables used to define a resolution test object of finite width and infinite length cast onto a Cartesian coordinate system. ....	164
Figure B.1: Absolute error of sinusoid simulations using Eq. B.15.....	174

## List of Abbreviations

CPNR	Correlated Polarity Noise Reduction
1-D	One-dimensional
2-D	Two-dimensional
3-D	Three-dimensional
FT	Fourier transform
PSF	Point spread function
LSF	Line spread function
ESF	Edge spread function
OTF	Optical transfer function
MTF	Modulation transfer function
NPS	Noise power spectrum
DQE	Detective quantum efficiency
FPD	Flat panel detector
ROI	Region of interest
SNR	Signal-to-noise ratio
CNR	Contrast-to-noise ratio
PFR	Principle frequency response
DPS	Distortion power spectrum
DI	Distortion index
$\Sigma$ DI	Summed (integrated) distortion index
THD	Total harmonic distortion
CT	Computed tomography

## Acknowledgements

My greatest thanks and love go to my beloved, my wife, Aimee. Without all of your love and support, this work might not have been possible. And thank you to my beautiful children, Juniper and Durham, who give me new reason each day to do my work with the greatest ingenuity and integrity. Mom and Dad, thank you for sacrificing so much to make sure your boys went on to college and for providing for us in every way. And as for the rest of my family and friends, you are too numerous to list here, and I am honored to travel this life journey with you.

Thank you to my many academic advisors at Duke University and beyond whose tutelage has made my love of knowledge all the greater. I reserve special thanks for my primary advisor, Dr. James T. Dobbins, III, who granted me the great gift of academic freedom through my tenure as his student.

Special thanks go to those who have supported my research needs over the years. Thank you to the Duke Clinical Imaging Physics Group (CIPG) for their helpful conversations and for providing equipment needed for experiments. Thank you to Paul Segars for bridge funding which helped me to complete my degree, and thank you also for the special opportunity to work in the exciting world of digital phantom development. Thanks to Drs. James Bowsher, Huy Yan, and Irina Vergalasoza for helping me acquire CBCT data.

And finally, my deepest gratitude goes to my MMM brothers for the strength of our friendship and for sharing in many creative consultations. Gentlemen, you are each truly inspired.



# 1. Introduction

Over the past few decades, there has been increasing awareness of the health risks associated with medical radiation exposure. In the United States (US), the average cumulative individual dose from all sources to a member of the population almost doubled from 3.6 mSv in the early 1980s to 6.2 mSv in 2006 owing largely to an almost seven-fold increase in medical radiation exposure. [1] The increase in medical radiation use was the only statistically significant change during those two decades; this was due primarily to the increased use of high dose computed tomography (CT) and nuclear medicine procedures (Figure 1.1 and Figure 1.2).[2] Of the estimated 434 million diagnostic procedures involving ionizing radiation performed in 2006, approximately 67 million (15%) were CT and 20 million (5%) were nuclear medicine procedures, yet they accounted for 75% of the total medical exposure to the population. [1] By contrast, the majority of diagnostic studies ( $\approx 324$  million or 75%) were categorized as conventional radiography examinations which accounted for less than 11% of the total cumulative dose to the population. These increases in radiation exposure not only pose an increase in cancer risk to the overall population, but the risk to individuals has increased due to the increased prevalence and utilization of high dose medical procedures.

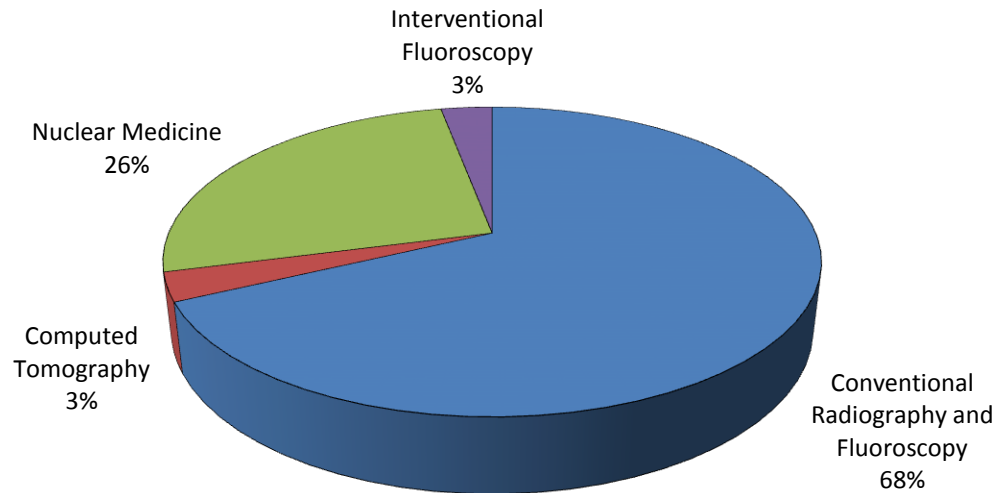


**Figure 1.1: Medical radiation exposure of patients in the early 1980s.**

Percentages quoted using effective dose equivalent ( $H_E$ ). Medical radiation in the 1980s accounted for 15% of the total average radiation exposure to members of the US population. Data were obtained from NCRP Report 160. [3]

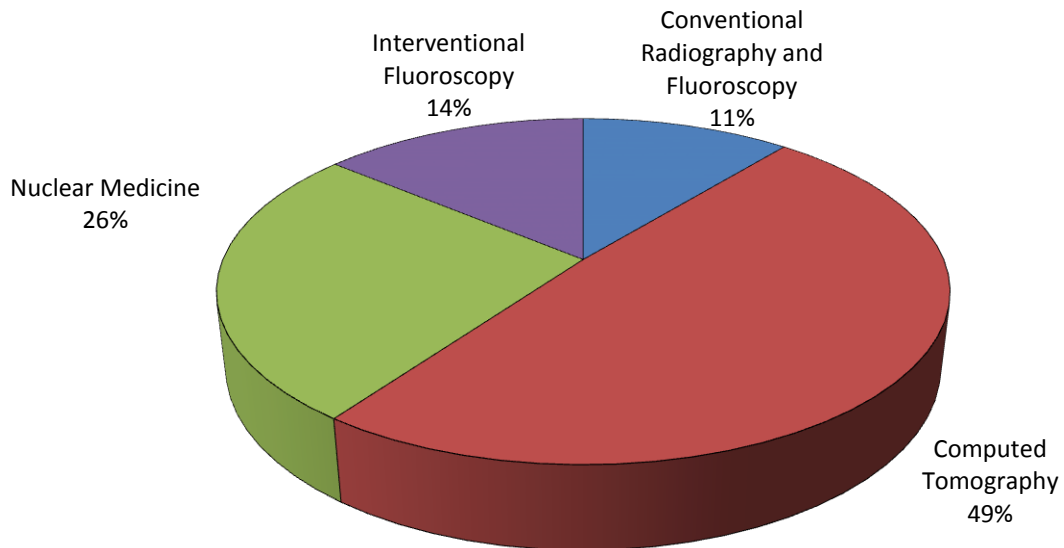


**Figure 1.2: Medical radiation exposure of patients in 2006.**

Percentages quoted using collective effective dose ( $S$ ) to the patient population measured in person-Sv. Medical radiation in 2006 accounted for 48% of the total average radiation exposure to members of the US population. By comparison, background radiation accounted for 50% of the total average exposure. Data were obtained from NCRP Report 160. [3]

Highly publicized reports [4] have further emphasized that radiation exposure is on the rise as high radiation-output devices such as CT are being used more prevalently in medicine. Campaigns such as Image Wisely [5] and Image Gently [6, 7] have advocated the judicious use of medical radiation in keeping with the As Low As Reasonably Achievable (ALARA) principle. [8] A considerable volume of scientific work is also underway to determine the necessary and appropriate level of radiation dose for imaging, especially for procedures involving vulnerable members of the population such as children. [9-12] All of these factors have prompted the scientific and medical communities to develop and implement strategies for the more efficient use, management, and control of medical radiation.

### ***1.1 Imaging Dose Reduction Strategies***

There is a growing interest in the scientific community about the appropriate utilization of radiation dose in medical procedures and what can be done to minimize its negative impact while still maintaining the beneficial aspects of advanced diagnostic procedures. In response, investigators have taken several approaches to reducing the radiation dose required for a given diagnostic task. One approach to dose reduction in projection x ray imaging is x ray spectrum optimization. Through the selection of appropriate  $kV_p$  and beam filtration, image signal-to-noise ratio (SNR) at a given radiation dose can be maximized. [13] A second approach to dose reduction is focused on improving the efficiency with which radiation is used by the imaging system. This imaging system characteristic is quantified by the detective quantum efficiency (DQE). Flat-panel detectors have improved the DQE(0) of radiography to about 65% from about 30% achieved with screen-film and computed radiography systems. [14]

Several other approaches to dose reduction have been implemented in CT. Tube current modulation can be used to minimize radiation exposure of more transmissive and/or radiosensitive parts of the anatomy such as the breast. [15-17] Another means of reducing dose has been accomplished by shaping the intensity profile of the x ray beam in CT using compensators such as bowtie filters. These filters shape the radiation beam to deliver less radiation to thinner, more transmissive parts of the patient anatomy such as the extremities. [18, 19] Finally, a new class of iterative CT reconstruction algorithms have made their way into clinical use. [20-23] These algorithms can be used not just for reducing imaging dose by up to eight-fold for a given image SNR, but also for improving the resolution of reconstructed images. Although iterative reconstruction techniques require longer reconstruction times than more conventional filtered back-projection methods, these algorithms are gaining increasing popularity among investigators and clinicians.

## ***1.2 Image Processing Algorithms for Dose Reduction and SNR Improvement***

Another strategy for reducing image noise is through the use of post-processing image noise reduction algorithms. These algorithms are generally used for one of two purposes in medical imaging: to improve the SNR of images acquired at a set dose or to match the SNR of reduce-dose scans to the SNR achieved at normal dose. In general, the remainder of the text will focus on the latter. One particular class of advanced algorithms for noise reduction includes algorithms which are nonlinear in nature. These algorithms depart from kernel-based linear smoothing approaches by implementing nonlinear denoising methods to achieve noise reduction without excessive blurring of anatomical information. Some popular algorithms which have been applied to medical imaging are the bilateral filter, [24-27] wavelet denoising, [28-31] and non-local means [32-34]. Each of

these algorithms has been used in x ray or CT imaging applications to achieve at least a two-fold reduction in noise variance (dose). Increasing the aggressiveness of these techniques can, however, impart undesirable characteristics into the post-processed image. Bilateral filtration, for instance, can produce a nonuniform residual noise print as a result of nonuniformities in noise processing near high contrast edges. Unnatural noise characteristics such as noise nonuniformity may cause observer confidence and performance to decline. [35] Other algorithms such as wavelet denoising have been shown to introduce nonlinear distortion artifacts when aggressively applied for image denoising. [36] Algorithms such as nonlocal means may also distort anatomical textures when applied to medical images; these textures are often times crucial to the diagnostic utility of medical images.

A second class of noise reduction algorithms is statistical in nature. One very popular statistical noise reduction paradigm is the family of anisotropic (partial) diffusion algorithms. [37-39] The anisotropic diffusion algorithm models image noise using the heat diffusion equation from physics. Smoothing of the image noise is modulated throughout the image with increased smoothing (conduction) in uniform image regions and reduced smoothing (conduction) at the edges of structured (anatomical) image content. Xia *et al.* [38] used this concept in application to breast CT imaging to reduce the dose by up to 60%. Yet another noteworthy statistical noise reduction algorithm which has been applied to chest and breast imaging is Bayesian image estimation (BIE). [40-45] The BIE approach evaluates the pattern of pixel-to-pixel variation and associates that pattern with the variations that would be expected from Poisson-distributed quanta. Any variations that are in excess of the amount expected from Poisson statistics are assumed to represent changes in the image due to anatomy and not noise. These statistical methods have generally

performed the best of all noise reduction strategies to date, but they take considerable time to compute due to their complex and iterative nature, and can leave various artifacts. Therefore, there is still cause to investigate new and promising nonlinear denoising approaches as an important component in the greater task of imaging dose management and SNR improvement.

### ***1.3 Dissertation Objectives***

This dissertation is focused on the development, assessment, and application of a new paradigm for medical image noise suppression called Correlated Polarity Noise Reduction (CPNR). Although several denoising algorithms have shown promise in the medical imaging field, there remain several important issues to be improved upon including:

1. Preservation of noise texture (spatial correlation)
2. Preservation of the noise magnitude distribution shape
3. Preservation of low contrast anatomical structure
4. Reduction/elimination of blurring and resolution artifacts

Using an iterative statistical approach, CPNR basically reverses the statistical process by which noise is added to an image from Poisson and random Gaussian-distributed processes. In doing so, experimental evaluation has shown that CPNR can lead to better than a two-fold reduction in radiation dose with minimal degradation of image quality (SNR and spatial resolution) and minimal artifacts. [46] Because the algorithm is simple in concept and does not require complicated manipulation of the image data, it can be implemented in a rapid fashion.

In order to assess the resolution properties of this new denoising technique, new tools for nonlinear algorithm metrology are developed. A review of current strategies for linear systems resolution assessment will show that they fail to properly account for

possible nonlinear distortions in image data. By investigating nonlinear algorithm response to a series of sinusoidal test signals, it will be shown that the contrast resolution and nonlinear distortion properties of nonlinear algorithms can be successfully separated for independent analysis. A comparison of CPNR against two other nonlinear denoising algorithms using the newly developed metrics shows that CPNR improves the resolution of low contrast-to-noise ratio (CNR) image details without the introduction of nonlinear distortions to the image data. This work in nonlinear resolution and distortion performance analysis represents a significant contribution to the field of medical imaging metrology.

In the final chapter of this dissertation, preliminary application of CPNR to CT denoising will be presented. Simulation studies show that a 40% reduction in image dose is possible with minimal degradation of image edges for conventional multi-detector CT. However, application of the new denoising techniques to clinically acquired cone-beam CT (CBCT) data show that up to 49% dose reduction is achievable with minimal loss of resolution. This work is followed by a summary of the dissertation and the proposal of future work.

## 2. Correlated Polarity Noise Reduction

Correlated polarity noise reduction (CPNR) is a novel noise reduction technique. It is a nonlinear, statistical noise reduction method which reduces image noise variance by first estimating the polarity (sign) of the random noise component followed by the subtraction of a pseudorandom number with matching polarity at every image pixel. For example, if the noise in a given pixel is estimated to be positive, then a random number that is also positive will be subtracted from that pixel. In this way, CPNR represents a major departure from more traditional noise reduction methods which estimate both the noise polarity and magnitude directly from image data. Using the CPNR strategy, image noise variance can be reduced by up to 40% per iteration with little negative impact on image resolution, few artifacts, and a residual noise print with “normal” appearance. In this chapter, CPNR will be developed in detail followed by examples of CPNR application to radiography. This work is prerequisite to CPNR application to CT (Chapter 5) and other medical imaging modalities such as tomosynthesis, fluoroscopy, and even nuclear medicine imaging.

Some of the work in this chapter was previously presented at the 2011 International Society for Optics and Photonics (SPIE) Annual Meeting followed by published conference proceedings. [46]

### 2.1 Introduction to CPNR

In general, a 2-D image  $I(x, y)$  can be modeled as some signal of interest  $S(x, y)$  and a random additive noise component  $R(x, y; \sigma_N)$  with random distribution width defined by parameter  $\sigma_N$ :



$$I(x, y) = S(x, y) + R(x, y; \sigma_N) = S(x, y) + \text{pol}[N(x, y)] |N(x, y)|. \quad (2.1)$$

Without loss of generality, Eq. (2.1) is represented in 2-D space and is easily expanded into higher-dimensional space. The equation is also written in terms of noise polarity  $\text{pol}[N(x, y)]$  and noise magnitude  $|N(x, y)|$  to aid the descriptions that follow.

The problem of image noise reduction has been approached by many authors through the use of many different algorithms – some linear, some nonlinear, some deterministic, and some statistical in nature. Conventional noise reduction algorithms generally conduct denoising by making some estimate of the image noise and subtracting it from the image data to produce an estimate of the noise-free or noise-reduced signal of interest. This approach can be problematic for several reasons. To obtain an estimate of the actual image noise, an algorithm must estimate both the sign of the noise (its polarity) as well as the noise magnitude directly from the image data at every image pixel. While this is generally not difficult to do in flat image regions devoid of signal structure, noise estimates near edges are often biased by large changes in the background or signal intensity. In the case of medical imaging, the signal of interest is some anatomical or physiological feature which generally contains edges that need to be preserved. If the changes in pixel intensity due to edges are mistaken for intensity change due to noise, the edges can be suppressed and artifacts may be introduced into the processed image. Low contrast features are also highly susceptible to this type of corruption. Furthermore, when estimates of the noise are made directly from image data, the processed noise print can look unnatural leading to issues with image interpretation. [35] These distortions in the noise texture should also be avoided to preserve the integrity and the utility of the medical image.

The CPNR concept is proposed as a potential solution to these problems which are typical of other denoising algorithms. CPNR was initially conceived and developed by

Dobbins who described the general concepts in a presentation at the Radiological Society of North America annual meeting in 1996. [47] It works by first making accurate estimates of the noise polarity followed by the subtraction of a random number with matching polarity:

$$I'(x, y) = S(x, y) + N(x, y) - \text{pol}[N(x, y)] |R(x, y; \sigma_{N'})|. \quad (2.2)$$

In Eq. (2.2),  $I'(x, y)$  is an estimate of the noise-reduced image and  $|R(x, y; \sigma_{N'})|$  is the absolute value of a random number with distribution width  $\sigma_{N'}$  which is based on an estimate of the distribution width of  $N(x, y)$ . By subtracting a random number, CPNR lets the statistical nature of the subtracted noise distribution reduce the noise variance. This avoids the error-prone process of trying to estimate the noise magnitude at every image pixel. By subtracting a random distribution of noise, it is hypothesized that, on average, image noise can be reduced while maintaining image noise texture with better preservation signal integrity. This is due to the fact that  $R(x, y; \sigma_{N'})$  is independent of the image itself. It would be impossible for the subtracted noise distribution to be influenced by image edges, whereas subtracted noise magnitudes estimated directly from image data are very often corrupted by the influence of image edges leading to an assortment of problems including edge suppression, artifacts, and noise nonuniformity. Also, by subtracting random noise values, the residual noise print left after CPNR should have a “normal” appearance which is another desirable quality. Therefore, given a sufficiently accurate estimate of noise polarity combined with an appropriate subtracted noise distribution, better image noise suppression may be achieved using CPNR.

It is well known that adding or subtracting the values of two uncorrelated random variables results in a third random variable with greater variance than the original two random distributions. According to the propagation of error formula, a variable  $f$  obtained

by adding or subtracting two random number distributions according to  $f = aR_A \pm bR_B$  has variance

$$\sigma_f^2 = a^2\sigma_A^2 + b^2\sigma_B^2 \pm 2ab \text{cov}_{AB}. \quad (2.3)$$

Indeed, if  $R_A$  and  $R_B$  are completely uncorrelated (i.e. their covariance  $\text{cov}_{AB} = 0$ ), their sum or difference always results in a third normal random variable with higher variance. However, the polarity term in the CPNR equation [Eq. (2.2)] creates positive correlation between the image noise and the subtracted random noise distribution, hence the name “Correlated Polarity Noise Reduction.” By positively correlating the sign of the random numbers, the covariance term in Eq. (2.3) is made positive which makes reduction in the residual variance possible.

The CPNR concept is demonstrated by a simple computer simulation in Table 2.1. Subtracting the values of two normally distributed random variables  $N_1(0, \sigma)$  and  $N_2(0, \sigma)$  with perfectly correlated polarities results in a third random variable with standard deviation of  $0.85\sigma$  which corresponds to a 28% reduction in noise variance. By recursively applying this operation in an iterative framework, similar variance reduction can be achieved with every iteration. After  $j$ -iterations, the fundamental CPNR equation becomes

$$I'_j(x, y) = I'_{j-1}(x, y) - \text{pol}[N'_{j-1}(x, y)] \left| R_{j-1}(x, y; \sigma_{N'_{j-1}}) \right|, \quad \begin{cases} I'_0 = I \\ \lim_{j \rightarrow \infty} I'_j = S' \end{cases} \quad (2.4)$$

**Table 2.1: MATLAB validation of the CPNR concept.**

V1 = 1;	% Noise variance
S1 = sqrt(V1);	% Noise standard deviation
N1 = randn(2^25, 1) .* S1;	% Noise variable 1
N2 = randn(2^25, 1) .* S1;	% Noise variable 2
POL1 = sign(N1);	% Polarity of N1
N2 = abs(N2) .* POL1;	% Correlate polarities of N2 with N1
N3 = N1 - N2;	% Subtraction of N2 from N1
VRATIO = var(N3) / V1;	% Change in noise variance

Figure 2.1 shows how the variance of a distribution of random Gaussian noise can be iteratively reduced using CPNR. The original noise image contains Gaussian-distributed random noise with standard deviation  $\sigma_0 = 1$  and zero mean. When the polarity of the noise is known with 100% accuracy, on average, the random noise variance is reduced by 24% per iteration using the iterative CPNR technique in Eq. (2.4). This is strong evidence which suggests that CPNR may be a viable technique for noise suppression in medical imaging.

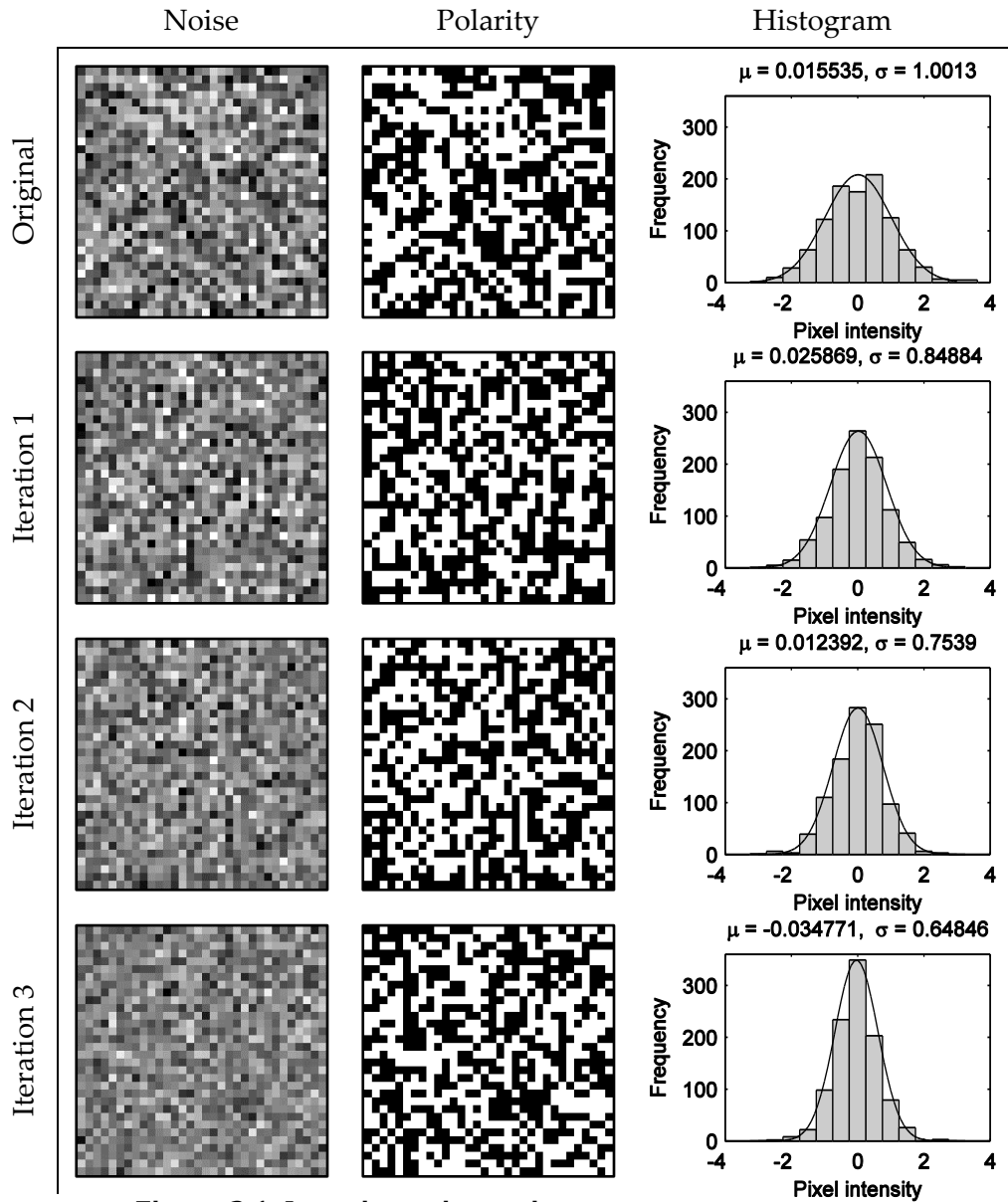


Figure 2.1: Iterative noise variance reduction by CPNR.

These results show iterative noise reduction by CPNR given that all polarities are known exactly. Each row depicts the noise, the noise polarity, and the intensity histogram associated with the respective noise image. The original noise distribution was simulated with  $\mu_0 = 0$  and  $\sigma_0 = 1$ . The noise standard deviation is reduced by an average of 13% per iteration which, according to Poisson statistics, corresponds to a 24% reduction in variance (x ray dose) per iteration.

## 2.2 Polarity Estimation

In this section, a method for estimating noise polarities from image data is introduced. Noise polarity estimation is the first key step in conducting CPNR; the accurate estimation of noise polarity is crucial to CPNR success. To estimate noise polarity, background trends and changes in pixel intensity due to anatomy must be ignored. This is achieved by making some fit to the anatomical signal and subtracting it from the image data. The sign of the residual should then provide an estimate of the noise polarity. By way of equation,

$$\text{pol}(N') = \text{sgn}(I - S'). \quad (2.5)$$

In Eq. (2.5),  $\text{sgn}(\ )$  is the sign operator,  $I$  is the original image data,  $S'$  is a fit (estimate) of the noise-free signal  $S$ , and  $\text{pol}(N')$  is the estimated noise polarity. If it were possible for  $S'$  to be a highly accurate estimate of the noise-free signal, the noise reduction problem would be largely solved and no further work would be required. However, accurate estimates of the noise-free signal are notoriously difficult near image edges, and this can lead to edge blurring and edge artifacts. On the contrary, the noise polarity estimation problem is a much easier one which does not require a perfect estimate of the noise-free signal for high polarity accuracy.

The robustness of the noise polarity estimation technique compared to the signal estimation technique is demonstrated in Figure 2.2. The signal  $S$  is strictly defined by the thick black line, and the noisy image data  $I$  are denoted by red “x” marks. Whereas it can be very difficult to accurately fit the noise-free signal value at each and every point along the black line, there is a wide range of possible fit values at each and every sample location that would return an accurate polarity estimate (denoted by the transparent green zones). In

this way, the noise polarity estimation problem is more resistant to errors in background (signal) trend fitting.

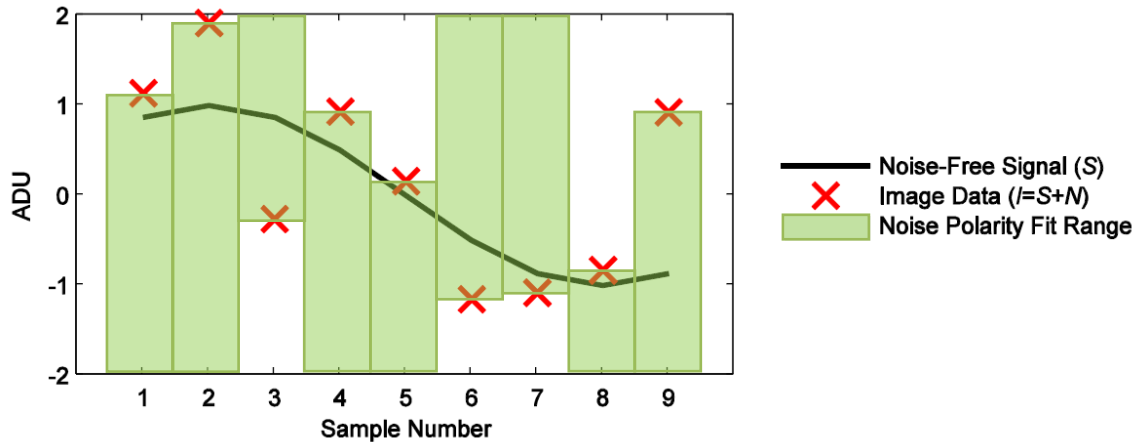


Figure 2.2: Noise polarity estimation versus signal fitting.

Highly accurate estimates of the noise-free signal  $S$  are very difficult to achieve, especially in high noise environments. On the other hand, estimating noise polarity is a much easier task. Accurate noise polarity estimates can be achieved by any fit to the data which passes through the transparent green zones. In this way, the noise polarity estimation problem is much more forgiving to errors in background trend fitting.

Therefore, according to the CPNR paradigm, it is only necessary to estimate the signal  $S$  with enough accuracy to get the noise polarity correct. This is a much easier task than trying to exactly estimate the noise-free signal itself with very high accuracy. In order for CPNR to achieve good noise polarity estimates, line segments are used to fit local image data and approximate neighborhood background trends due to anatomy. A rotated linear mask (Figure 2.3) is designed to sample the image data in the local neighborhood surrounding each image pixel at a particular angle. By rotating this mask through several angles  $\theta$ , angles containing strong edges can be detected and appropriately fit (or ignored) to prevent signal edge information from contaminating the noise polarity estimation step.

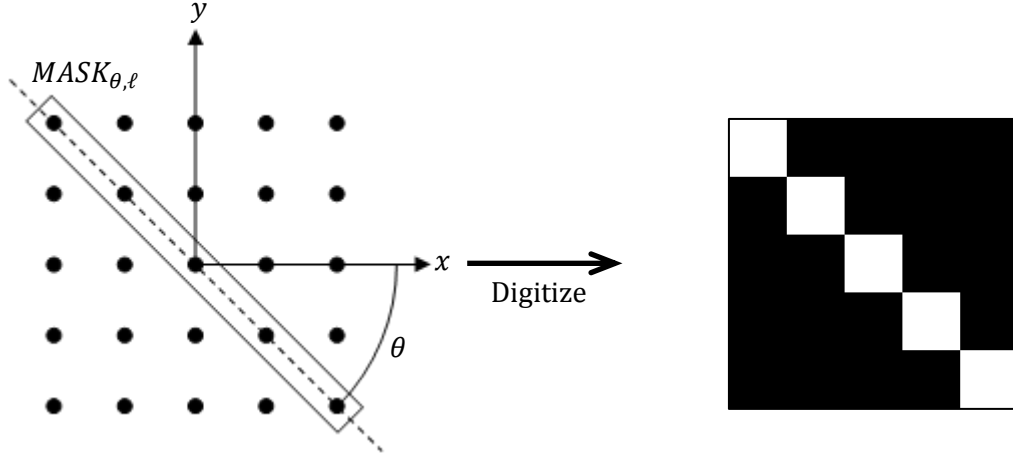


Figure 2.3: Directional sampling mask.

A CPNR mask is generated using the digital approximation of a line segment with orientation  $\theta$  and length  $\ell$ . A nearest neighbor methodology is used to convert the continuous representation on the left to the digitized representation on the right. Doing so ensures that a given mask contains exactly  $\ell$ -pixels.

The background trend (anatomy) in each mask can be fit using a simple 1-D polynomial fitting routine to remove the influence of anatomical signal in preparation for the noise polarity estimation step. Polynomial coefficients  $a_{\theta, \ell, p}$  can be determined as

$$a_{\theta, \ell, p} = (X_{\ell, p}^T X_{\ell, p})^{-1} X_{\ell, p}^T I'(MASK_{\theta, \ell}), \quad (2.6)$$

where

$$X_{\ell, p} = \begin{bmatrix} 1 & 1 & 1^2 & \dots & 1^p \\ 1 & 2 & 2^2 & \dots & 2^p \\ \vdots & \vdots & \vdots & \ddots & \vdots \\ 1 & \ell & \ell^2 & \dots & \ell^p \end{bmatrix}, \quad (2.7)$$

and  $X_{\ell, p}^T$  is the transpose of matrix  $X_{\ell, p}$ . Variable  $p$  is the (positive) integer polynomial order.<sup>1</sup> The matrix  $I'(MASK_{\theta, \ell})$  is a column vector containing image data within the rotated

---

<sup>1</sup> It is required that  $p \leq (\ell - 2)$  so that noise polarity can be determined from the residual of the fit.



mask  $MASK_{\theta,\ell}$ . Combined, these variables can be used to generate an estimate of the noise-free signal  $S'$  as

$$S'_{\theta,\ell,p} = X_{\ell,p} \alpha_{\theta,\ell,p}, \quad (2.8)$$

where  $S'_{\theta,\ell,p} \left( \frac{\ell+1}{2} \right)$  is the estimated signal intensity at the center pixel of  $MASK_{\theta,\ell}$  using a polynomial of order  $p$  and odd  $\ell$ .<sup>2</sup> Therefore, noise polarity at this location within the mask is estimated as

$$\text{pol}(N'_{\theta,\ell,p}) = \text{sgn} \left[ I'_{\theta,\ell} \left( \frac{\ell+1}{2} \right) - S'_{\theta,\ell,p} \left( \frac{\ell+1}{2} \right) \right]. \quad (2.9)$$

Eq. (2.9) is computed at all pixel locations in an image to produce a complete polarity map based on fitting the data contained in  $MASK_{\theta,\ell}$  with a 1-D polynomial of order  $p$ . The process is repeated at all mask angles  $\theta$  (Figure 2.4) to produce multiple noise polarity estimates at each pixel location.

---

<sup>2</sup> Experiments showed that estimates of  $S'$  at off-center locations within the linear mask resulted in poorer signal estimation due to polynomial fit divergence and the involvement of nonlocal image information which disproportionately weighted low-frequency trends in the data.

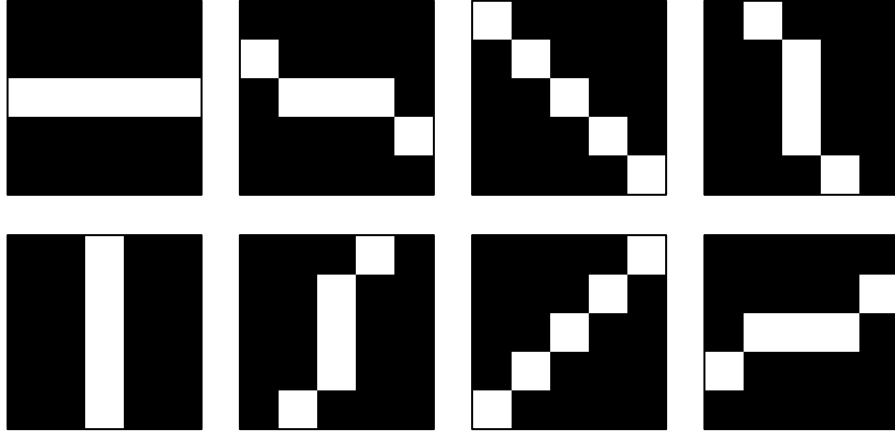


**Figure 2.4: Sample masks at various angles.**

**These 5-element long masks were generated at eight evenly-spaced angles in the range  $[0^\circ, 180^\circ]$ .**

Preliminary tests showed that using 16 mask angles resulted in the best CPNR performance. If too few mask angles were used, polarity estimation accuracy diminished because edges at intermediate angles could not be properly detected and fit. The use of more angles, while justified, resulted in the redundant use of pixel data if the difference between adjacent angles was very small. The use of too many angles provided only small increases in polarity accuracy at the expense of increased algorithm run time. Therefore, for the remainder of this dissertation, 16 mask angles will be used unless otherwise noted.

Using different masks of various lengths and orientations coupled with polynomial fits of various orders produces many estimates of pixel polarity at each image pixel. In order to determine a final estimate of pixel polarity, a voting strategy is employed to determine a final estimate of noise polarity at each pixel:

$$\text{pol}(N'_{\ell,p}) = \text{sgn} \left[ \sum_{\theta} \text{pol}(N'_{\theta,\ell,p}) \right]. \quad (2.10)$$

The term within the summation is obtained from Eq.(2.9). Eq. (2.10) shows that the sign of the sum of the polarity estimates from all angular orientations  $\theta$  constitutes the final

polarity estimate by simple majority vote. It is easy to see that a majority of positive or negative polarity votes produces a positive or negative final polarity estimate. It is also possible for the number of positive votes to equal the number of negative votes resulting in a “zero” or “null” polarity estimate. Pixels with null polarity receive no modification due to uncertainty in noise polarity estimation, and this is an important benefit of the majority vote method. By reducing the noise estimation problem down to a vote on noise polarity, the noise reduction process is made independent of the noise magnitude at each image pixel. Rather, the noise reduction process is dependent only upon the reliability (certainty) of the noise polarity estimate. This is a major departure from other noise reduction methods which typically require estimates of the both the polarity and magnitude of the noise derived directly from image data. Attempts to measure both the sign and magnitude of the noise can be biased due to large differences between the image data  $I'$  and the estimate of the noise-free signal  $S'$ . This bias can lead to distortions in the denoised data such as changes in the noise magnitude distribution, small feature suppression, and edge blurring to name a few. It is believed that these problems can be avoided using the new noise reduction paradigm.

### **2.2.1 Polarity Accuracy**

Polarity accuracy maximization is a key component of successful CPNR execution. As the CPNR algorithm is developed further, parameter values will require optimization toward the goal of increasing polarity accuracy. In order to assess polarity accuracy, however, a suitable test image must be obtained. The test image should be similar to the target application in terms of signal and noise content due to the nonlinear nature of the

denoising mechanism.<sup>3</sup> Ideally, this image should also be paired with a “known truth” or noise-free signal for proper polarity accuracy assessment. Since a truly noise-free image is impossible to obtain in practice, an alternative means of test image production is required.

To meet the criteria outlined for the ideal test image, the 4-D extended cardiac-torso (XCAT) phantom of Segars *et al.* is employed. [48] The XCAT phantom provides a robust digital patient model derived from actual human data. The high degree of anatomical realism combined with the ability to provide realistic simulations of real radiographic systems and noise-free images makes the XCAT phantom an ideal tool for quantitative medical image processing algorithm analysis and optimization. More information about the phantom and its capabilities can be found in the literature. [49, 50]

To narrow the scope of optimization, applications in projection x ray imaging were examined in this dissertation. For the purposes of CPNR development and optimization in this chapter, the XCAT phantom was used to simulate a posteroanterior (PA) chest examination. The simulated x ray detector had a 1024×1024 array of 0.4×0.4 mm<sup>2</sup> detector elements with 80% fill factor. This pixel size was selected as an intermediate pixel size between radiographic (0.2×0.2 mm<sup>2</sup>) and CT (0.8×0.8 mm<sup>2</sup>) denoising applications. The simulated x ray source was located at a source-to-image distance of 180 cm with a source-to-object distance of 150 cm. A 120 kV<sub>p</sub> x ray beam spectrum [51] was simulated. To achieve typical clinical noise levels, Poisson noise was added to noise-free XCAT projection images with appropriate intensity scaling. Scattered radiation was not simulated. Figure 2.5 provides the simulated chest radiograph used for accuracy testing throughout this chapter.

---

<sup>3</sup> Nonlinear algorithm performance is, in general, application-specific and context-dependent.

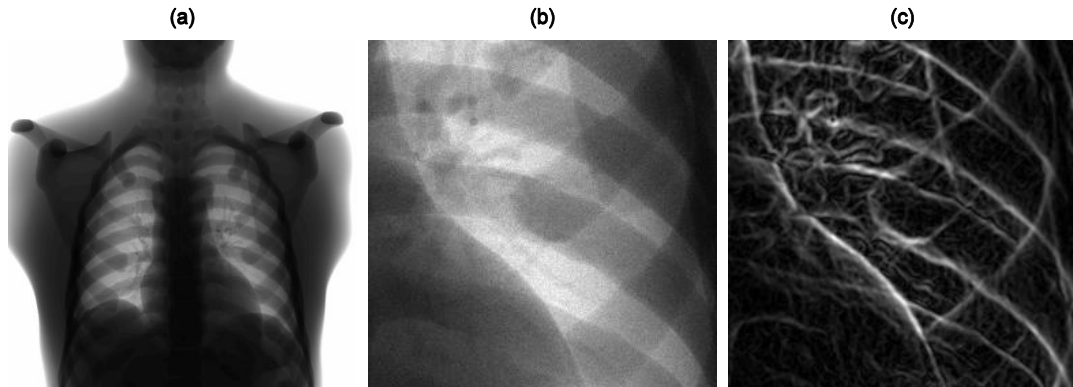


**Figure 2.5: Simulated chest radiograph images using the XCAT phantom.**

**(a) Full chest PA projection image without noise. (b) ROI from the left lung region with Poisson noise added to simulate image noise at half the normal dose. (c) Gradient magnitude of (b) using the Canny operator with Gaussian standard deviation of  $\sqrt{2}$ . Gradient operators can be used to identify image regions with high intensity gradient (i.e. high contrast edges); it is important to preserve the integrity of image edges during processing. Note that the simulated images have intensities which are proportional to detector exposure.**

Using Figure 2.5(b), the accuracy of the majority vote method [Eq. (2.10)] was tested for several combinations of mask length and polynomial fit order. Numerical results are provided in Figure 2.6 and graphical results are provided in Figure 2.7. The polarity maps in Figure 2.7 can be used to gauge the amount of artifact induction and edge blurring at different CPNR parameter settings. Clusters of positive and negative polarity near edges are indicative of poor polarity estimation at edges which can lead to blurring. Excessive correlation and odd textures in the polarity maps can also indicate a higher likelihood of image processing artifacts.

Based on preliminary studies of noise power performance, resolution performance, and measurements of polarity accuracy, three combinations of mask length and polynomial fit order were selected for further investigation throughout the remainder of the dissertation. The three different combinations were chosen to reflect CPNR settings

optimized for low, mid, and high frequency performance. Those settings are as follows:  
 $p = 0$  and  $\ell = 7$  for low frequency performance;  $p = 2$  and  $\ell = 7$  for mid frequency performance; and  $p = 2$  and  $\ell = 5$  for high frequency performance.

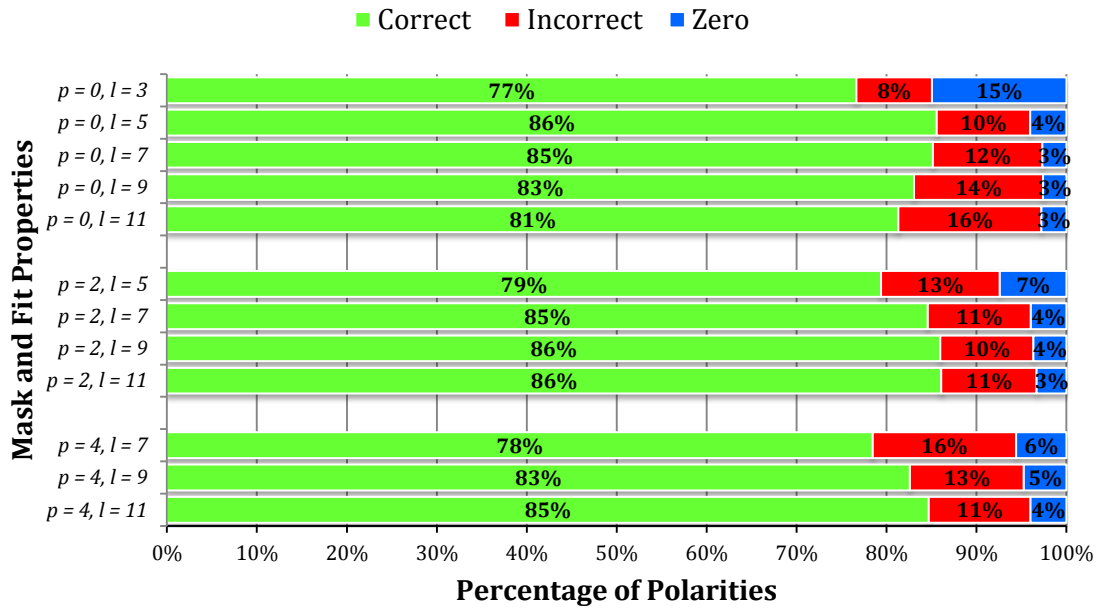


**Figure 2.6: Polarity accuracy of the majority vote method.**

Using the XCAT data from Figure 2.5(b), this bar chart shows the percentages of correct, incorrect, and zero polarity estimates from various CPNR mask length and polynomial order combinations.

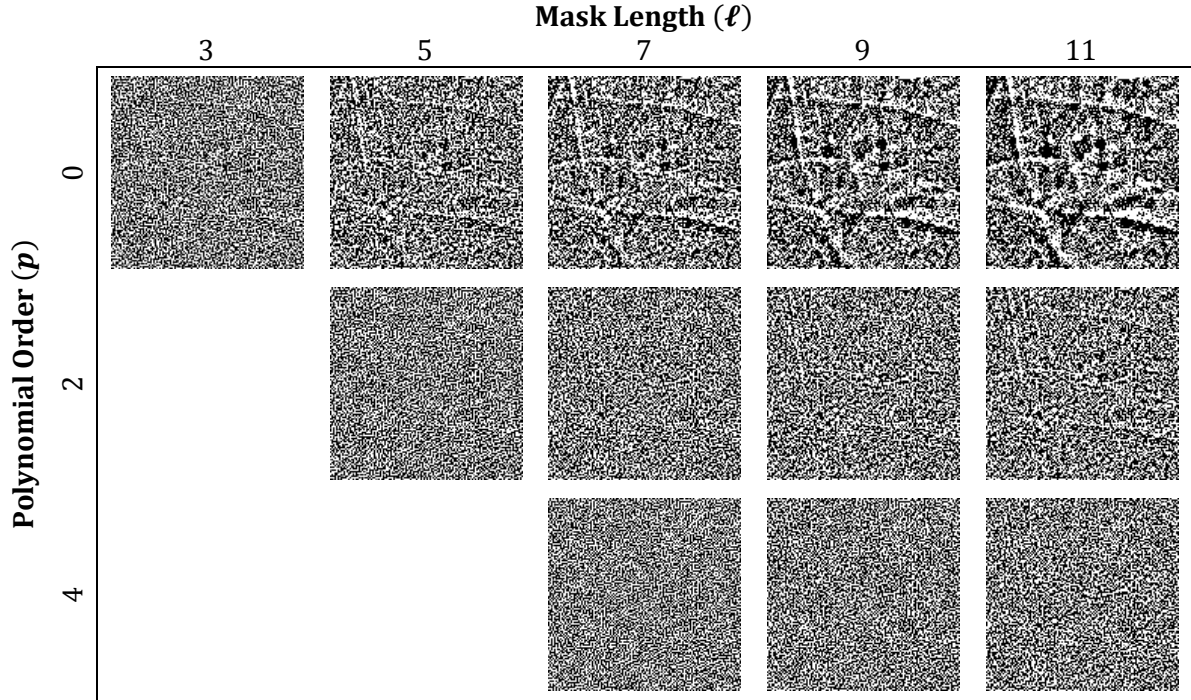


**Figure 2.7: Polarity maps showing polarity distribution, correlation, and artifacts for various polynomial order and mask length combinations.**

The images show negative [52], positive [53], and zero (gray) polarity estimates at various CPNR settings. Combinations of high polynomial order and short mask length provide better high frequency performance while low polynomial order and long mask length combinations provides better low frequency performance. Based on preliminary noise and resolution performance analysis, three polynomial order and mask length combinations were preselected for further analysis:  $(p, \ell) = (0, 7)$ ;  $(p, \ell) = (2, 7)$ ; and  $(p, \ell) = (2, 5)$ .



## 2.2.2 Supermajority Voting Strategy

Given the success of the majority voting strategy, a natural extension would be a supermajority voting strategy. By requiring a supermajority vote for pixel polarity determination, pixels with a weak majority vote (less confidence) will receive no (zero) polarity assignment. This should reduce the total number of incorrect polarity assignments in exchange for zero polarity assignments – a preferable alternative. Modification of Eq. (2.10) to include a supermajority threshold yields

$$\text{pol}(N'_{\ell,p}) = \begin{cases} \text{sgn} \left[ \sum_{\theta} \text{pol}(N'_{\theta,\ell,p}) \right], & \left| \sum_{\theta} \text{pol}(N'_{\theta,\ell,p}) \right| > t_{MAJ} \sum_{\theta} |\text{pol}(N'_{\theta,\ell,p})| \\ 0, & \text{otherwise,} \end{cases} \quad (2.11)$$

where  $t_{MAJ}$  is the fractional supermajority threshold. Eq. (2.11) reduces to Eq. (2.10) at the 50% supermajority threshold (i.e.  $t_{MAJ} = 0.5$ ). The polarity accuracy at different supermajority thresholds is tabulated in Figure 2.8 with graphical results provided in Figure 2.9.

The intention of supermajority voting is to retain only those polarity estimates with high confidence. By increasing the supermajority threshold requirement, the confidence in polarity assignment increases: when more polarity votes agree, it can be reasonably assumed that the estimated polarity is more likely to be correct. For instance, if the supermajority requirement for polarity assignment is increased to 100% (i.e. all votes agree), the accuracy of assigned polarities also nears 100%. However, the number of zero (inactive) polarities also increases which can lead to nonuniformity in the residual noise print. The optimal  $t_{MAJ}$  value is one that maximizes the fraction of correct polarities relative to the fraction of incorrect polarities without the generation of excessive zero votes. In this regard, a reasonable tradeoff can be achieved in the 60%-70% supermajority range

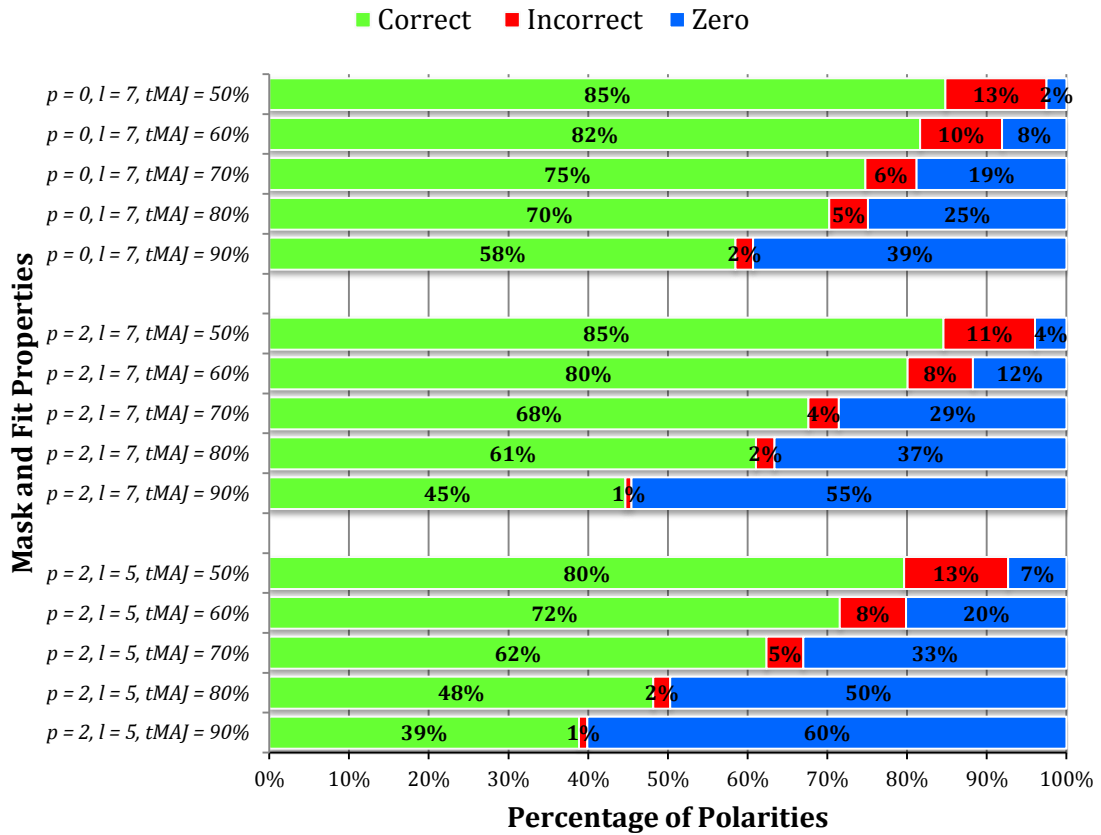


**Figure 2.8: Accuracy of majority vote method with supermajority constraints.**

By requiring a supermajority of votes, the fraction of erroneous polarities relative to the fraction of correct polarities can be reduced. This is achieved by setting polarity votes which fail to meet the supermajority threshold to zero.

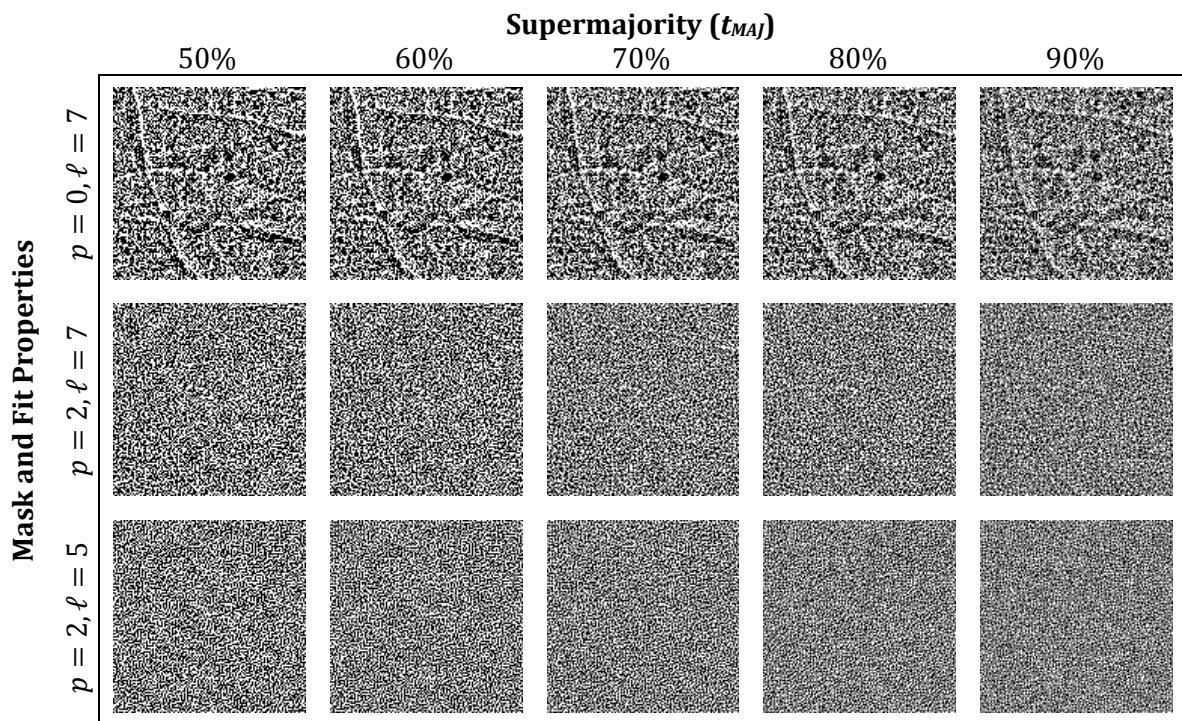


Figure 2.9: Polarity maps generated using the supermajority voting strategy.

Supermajority voting may be used to assign a “zero” polarity to those pixels with uncertain polarity estimates. Overall, this increases the relative accuracy of polarity estimation but can result in noise print nonuniformity at supermajority thresholds above 80%. There do not appear to be any edge-saving benefits to supermajority voting.

### 2.2.3 High Variance Residual Thresholding

While supermajority voting reduces the relative fraction of incorrect polarity estimates, it does not improve the concentration of obvious polarity errors near high contrast edges. This effect is especially pronounced for 0<sup>th</sup>-order polynomial fitting as shown in Figure 2.7 and Figure 2.9. These errors occur due to the inability of low order polynomials to sufficiently fit the high frequency, high contrast edge information within masks parallel to the local gradient directions at these locations. Polynomial fits to the data contained within these masks tend to bias polarity estimates creating erroneous polarity clusters near edges. Figure 2.10 demonstrates that errors near high contrast edges can be reduced by using only those masks which are approximately perpendicular to the local gradient direction. Masks perpendicular to the local gradient contain far less of the high frequency, high contrast edge information; this helps to circumvent errors due to poor signal fitting near strong edges.

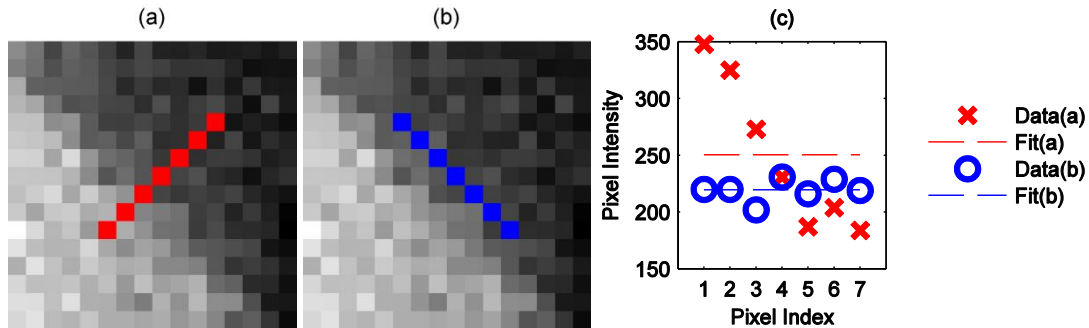


Figure 2.10: Noise estimation bias at high contrast edges.

(a) The red mask is approximately parallel to the local intensity gradient of the XCAT data. (b) The blue mask is approximately perpendicular to the local gradient (tangential to the edge). The masks are each centered on a pixel just to the low intensity side of the edge. (c) The plot shows that a 0<sup>th</sup>-order (mean) fit of the red mask data is positively biased by the edge information rendering an incorrect estimate of noise polarity while the blue mask data returns the correct (positive) noise polarity.

While it is important to increase the selectivity of fit results near edges, it is also important to retain as many votes as possible in flat image regions since using more votes generally increases the polarity accuracy. Therefore, a weighting scheme was developed which uses the variance of the polynomial fit residual to identify mask angles vulnerable to edge bias:

$$w_{\theta,\ell,p} = \frac{1}{RMSE^2}. \quad (2.12)$$

The function  $w_{\theta,\ell,p}$  assigns a weight to each  $MASK_{\theta,\ell}$  with polynomial fit order  $p$  based on the inverse of the root-mean-square error (RMSE)<sup>4</sup> of the polynomial fit which is defined as

$$RMSE = \sqrt{\frac{\sum [I'_{\theta,\ell} - S'_{\theta,\ell,p}]^2}{\ell}}. \quad (2.13)$$

The RMSE is an estimate of the local noise standard deviation (the square of which is an estimate of noise variance). However, if  $S'_{\theta,\ell,p}$  is a poor estimate of the real underlying signal of interest, then the difference  $[I'_{\theta,\ell} - S'_{\theta,\ell,p}]$  may be contaminated by signal edge content which would positively bias the estimate of the local noise variance. To avoid masks and polynomial fits subject to poor fitting, higher weights are assigned to masks containing lower variance data and vice versa. These weights are then normalized by the maximum mask weight at each pixel in the image:

$$\hat{w}_{\theta,\ell,p} = \frac{w_{\theta,\ell,p}}{\max(w_{\theta,\ell,p})}. \quad (2.14)$$

Once normalized, a threshold can be defined to suppress the votes generated from abnormally high-variance residuals:

---

<sup>4</sup> The RMSE is also known as the standard estimate of the error ( $\sigma_{EST}$ ).

$$\text{pol}(N'_{\theta,\ell,p}) = \begin{cases} \text{pol}(N_{\theta,\ell,p}), & \hat{w}_{\theta,\ell,p} \geq t_W \\ 0, & \text{otherwise.} \end{cases} \quad (2.15)$$

The threshold  $t_W$  is a value defined in the domain  $[0,1]$ . Eqs. (2.12), (2.14), and (2.15) are used to discard votes generated from masks with  $w_{\theta,\ell,p} < t_W \max(w_{\theta,\ell,p})$ . This provides a spatially adaptive method for voter rejection which favors edge preservation and improved noise reduction in flat image regions. These improvements are accomplished because the thresholding scheme eliminates only those polarity estimates from masks with higher variance data which often contain high contrast edge information. Increasing the threshold results in less polarity clustering (error) near high contrast edges but retains useful polarity estimates in lower contrast (flat) image regions since they contain comparatively lower variance image data. Figure 2.11 demonstrates the spatially adaptive performance of this methodology.

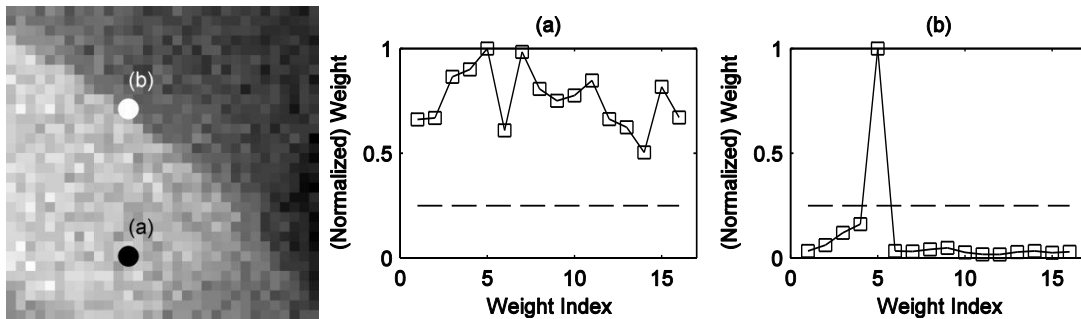


**Figure 2.11: Spatially adaptive variance-based weighting function.**

A 7-element mask was rotated at 16 angles at the pixel locations marked in the image. (a) No pixel polarity estimates are rejected at the  $t_W = 0.25$  level for a pixel located in a uniform image region. (b) Most polarity estimates for a pixel located near a high contrast edge are rejected at the  $t_W = 0.25$  level since they are likely to contain substantial edge information. The only polarity vote retained after thresholding was derived from data parallel to the high contrast edge.

Figure 2.12 provides a plot of polarity accuracy associated with various  $t_W$  values. The simple majority voting scheme [Eq. (2.10)] was used with different  $t_W$  settings.

According to the bar chart, a decrease in polarity accuracy is observed for larger  $t_W$ . The decrease in accuracy is due to the overall reduction in the number of eligible voters throughout the image. At  $t_W = 1$ , only a single vote passes the threshold at every pixel location in the image. Although this vote is obtained from the best-fitted data (i.e. the polynomial fit with lowest RMSE), there is still some inherent error associated with that estimation (see section 2.2.4 Low Magnitude Noise Thresholding). In spite of the reductions in polarity accuracy, Figure 2.13 shows that the  $t_W$  thresholding strategy improves polarity estimation performance near high contrast edges. This effect is most prevalent for the CPNR settings optimized for low frequency noise reduction. A threshold as low as  $t_W = 0.25$  provides some improvement in high contrast edge performance with little impact on polarity accuracy for the low frequency optimization. After examining the edge response at several  $t_W$  thresholds after 2-3 iterations, it was determined that  $t_W = 0.75$  provided the best CPNR performance in terms of edge preservation and noise reduction potential at the low frequency settings. Based on the images in Figure 2.13, the improvement in edge performance is not as evident in the mid and high frequency polarity maps. However, after running the CPNR algorithm for several iterations at different  $t_W$  showed that  $t_W = 0.5$  provided improvement in edge performance for the mid frequency setting, and  $t_W = 0.1$  improved high frequency performance. Although these threshold settings increased the total number of incorrect polarities, edges were spared after processing. The increase in the number of incorrect polarities slightly slowed the speed of CPNR convergence and limited the noise variance reduction potential. Depending on the application and the need to preserve the integrity of image edges, increases in  $t_W$  at the expense of some polarity inaccuracy can be justified.

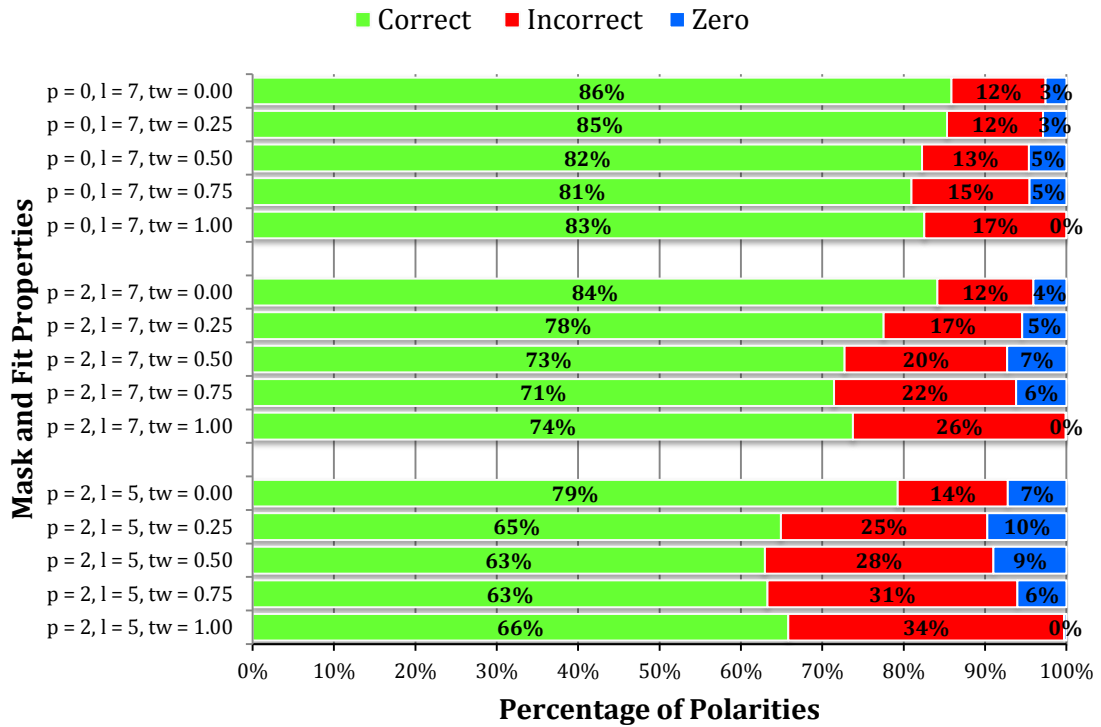
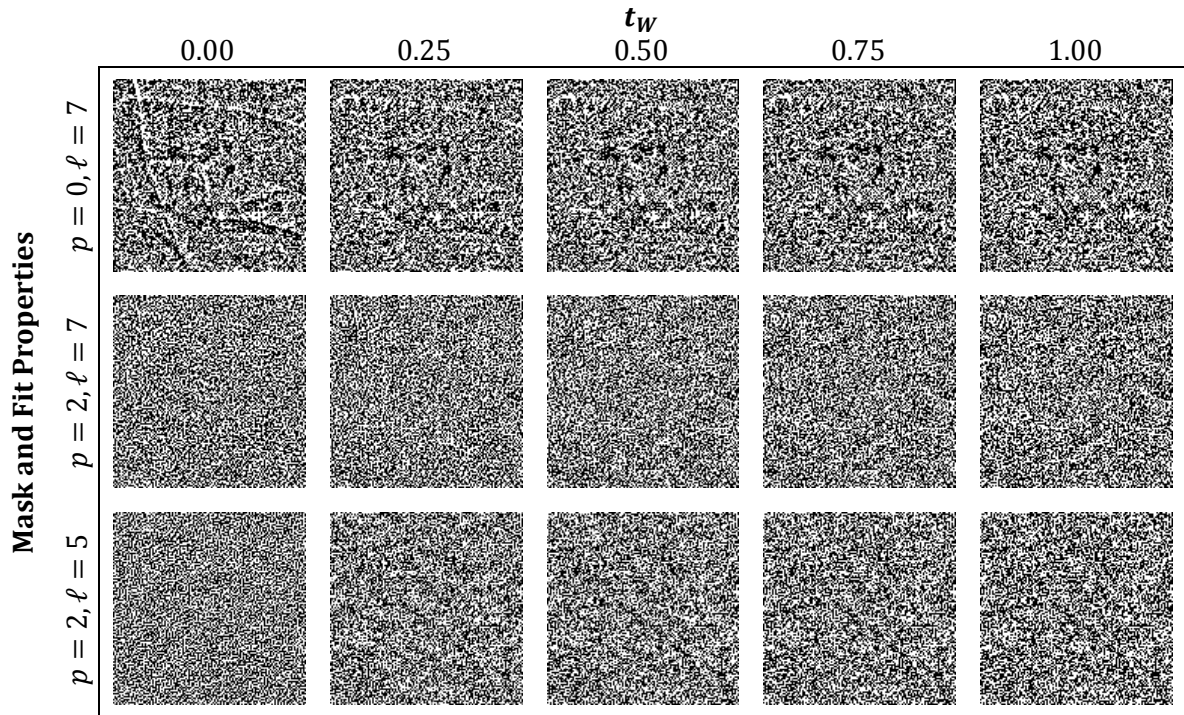


Figure 2.12: Polarity accuracy as a function of  $t_w$ .

The  $t_w$  threshold is designed to exclude polarity votes derived from poor polynomial fits to the anatomical signal. Although increasing  $t_w$  reduces the polarity accuracy, there are artifact reduction benefits that can be observed in Figure 2.13.





**Figure 2.13: Polarity maps showing artifact reduction by  $t_w$  thresholding.**

**Increasing  $t_w$  reduces polarity inaccuracy near high contrast edges. The benefit is most obvious when lower polynomial orders are considered.**

## 2.2.4 Low Magnitude Noise Thresholding

So far, several methods for improving polarity accuracy have been proposed, but further improvements might be possible. The previous section showed that polynomial fits with very high variance residuals often result in biased polarity estimates due to the strong influence of the image signal in these regions. By contrast, polarity estimates derived from very low variance noise may be equally prone to error due to the inability of polynomial fitting routines to accurately estimate the polarity of very low magnitude noise.

This idea is explored by first obtaining an estimate of the noise standard deviation at each image pixel. This is conveniently approximated by (unbiased) measures of the RMSE [Eq. (2.13)]. By using reliable estimates of the RMSE (i.e. RMSE associated with  $\hat{w}_{\theta,\ell,p} > 0$ ), the RMSE can be plotted and fit as a function of image pixel intensity [ $RMSE_{FIT}(I')$ ]. Then, if the magnitude of the difference  $|N'_{\theta,\ell,p}| = \left| I'_{\theta,\ell} \left( \frac{\ell+1}{2} \right) - S'_{\theta,\ell,p} \left( \frac{\ell+1}{2} \right) \right|$  (i.e. the estimated noise magnitude at mask center) does not exceed some fraction  $t_{RMSE}$  of  $RMSE_{FIT}(I')$ , then the confidence in the polarity estimate may be deemed insufficient implying that zero polarity should be assigned instead. Since the noise magnitude is already estimated to be very low, little improvement in the noise magnitude is likely to be achieved by further noise suppression. In fact, even if the polarity is correctly estimated, it is highly probable that the noise will be made worse at said locations. So, rather than running the risk of worsening the noise (or suppressing relevant anatomy), polarity estimates at pixels with low magnitude noise can be modified according to the following equation:

$$\text{pol}(N'_{\theta,\ell,p}) = \begin{cases} \text{pol}(N'_{\theta,\ell,p}), & |N'_{\theta,\ell,p}| > t_{RMSE} RMSE_{FIT}(I') \\ 0, & \text{otherwise.} \end{cases} \quad (2.16)$$

Several  $t_{RMSE}$  values were investigated, and those results are provided in Figure 2.14 and Figure 2.15. The simple majority voting scheme [Eq. (2.10)] was used with

different  $t_{RMSE}$  settings. As anticipated, the relative accuracy of assigned polarities increases with increases in  $t_{RMSE}$ . Of course, these potential improvements come at the cost of extra zero-polarity assignments which can cause nonuniformity in the noise print of processed images.

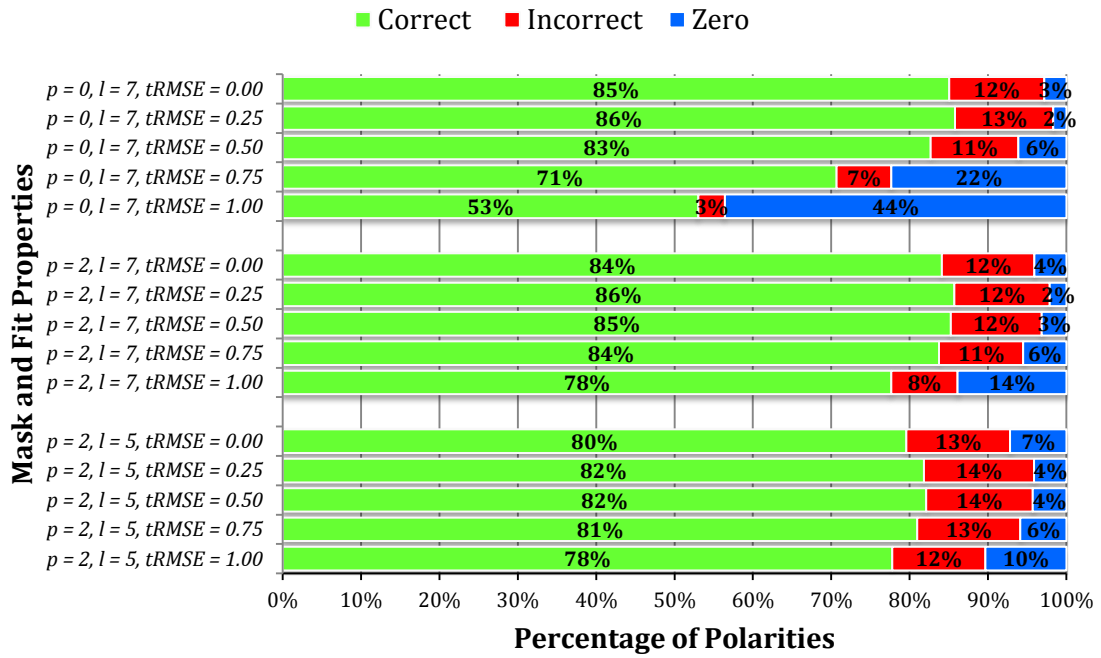


**Figure 2.14: Accuracy of  $t_{RMSE}$  noise magnitude thresholding.**

**Increasing  $t_{RMSE}$  provides improvement in the relative fraction of correct to incorrect polarity estimates by reassigning polarity estimates derived from low noise magnitudes to zero.**

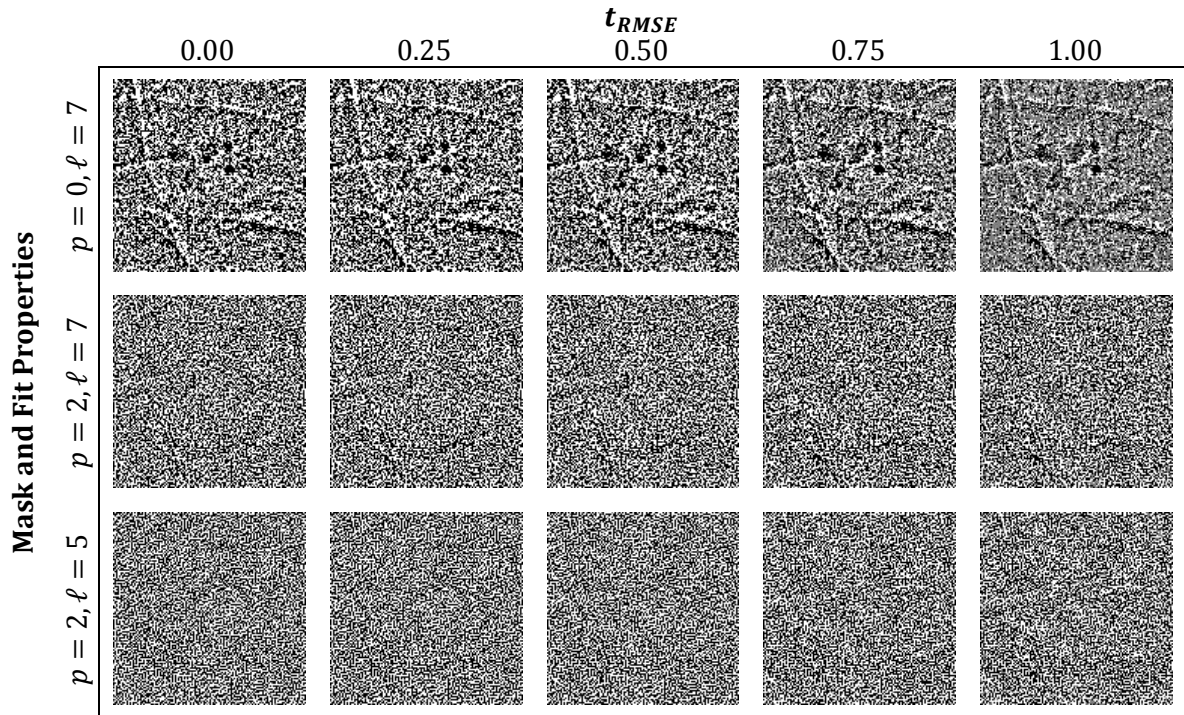


Figure 2.15: Polarity accuracy of the majority vote method with  $t_{RMSE}$  thresholding.

By eliminating votes made from low magnitude noise, some incorrect polarity estimates can be avoided. However, this comes at the cost of noise print nonuniformity as a result of extra zero polarities. This thresholding scheme does not appear to improve polarity estimation accuracy near edges.

## 2.2.5 Polarity Estimation Optimization

CPNR optimization is a complicated process. There are several factors to consider which include maximizing the number of correct polarities, minimizing the number of incorrect polarities (without generating excessive zero polarities), reduction of edge artifacts, and maintenance of the noise texture. So far, three parameters can be adjusted to accomplish these goals. The supermajority threshold  $t_{MAJ}$  was shown to greatly impact the number of correct and incorrect polarities but had minimal impact on reducing edge artifacts. On the other hand, the high variance threshold  $t_W$  had minimal impact on overall polarity accuracy but provided great improvements in CPNR performance at edges. And finally, the low noise magnitude threshold  $t_{RMSE}$  can be used to improve the ratio of correct to incorrect polarities, but must be assigned such that excessive zero polarities are not produced thus creating nonuniformities in the residual noise print.

To ensure the reduction of edge artifacts in radiographic imaging,  $t_W$  was manually set to avoid objectionable softening and smoothing of important anatomical features. In preliminary tests of edge performance, a high threshold of  $t_W = 0.75$  was selected for the low frequency settings,  $t_W = 0.50$  for the mid frequency settings, and  $t_W = 0.1$  for the high frequency setting. These thresholds resulted in the retention of fewer polarity votes at most pixel locations which resulted in overall reductions in pixel accuracy in exchange for polarity accuracy improvements near edges. Although the number of incorrect polarities increases with  $t_W > 0$ , those mistakes may be corrected in subsequent iterations. It is however the edge preservation effect afforded by  $t_W > 0$  which is the more desirable characteristic in application to radiography.

The remaining threshold values  $t_{RMSE}$  and  $t_{MAJ}$  require optimization. To accomplish this, a figure of merit must be devised which minimize the fraction of incorrect polarities

relative to the fraction of correct polarities without excessive zero polarity assignment. A figure of merit which favors these objectives is

$$f_{OPT} = \frac{f_{CORRECT}}{2 \times f_{INCORRECT} + f_{ZERO}/2}. \quad (2.17)$$

The figure of merit  $f_{OPT}$  in Eq. (2.17) weights reduction in the fraction of incorrect polarities ( $f_{INCORRECT}$ ) higher than it does increases in the fraction of correct polarities ( $f_{CORRECT}$ ). The fraction of zero polarities ( $f_{ZERO}$ ), while in the denominator, is weighted less than  $f_{INCORRECT}$  since zero polarities are more favorable than incorrect polarities but still less favorable than correct polarities. Many combinations of  $t_{RMSE}$  and  $t_{MAJ}$  were investigated for the low, mid, and high frequency CPNR optimizations, and the combination which produced the maximum value of  $f_{OPT}$  was determined to be the optimum. The optimized parameter sets are as follows:  $(p, \ell, t_{EST}, t_W, t_{MAJ}) = (0, 7, 0.25, 0.75, 0.6)$  optimizes CPNR for low frequency performance,  $(p, \ell, t_{EST}, t_W, t_{MAJ}) = (2, 7, 0.50, 0.50, 0.6)$  optimizes CPNR for mid frequency performance, and  $(p, \ell, t_{EST}, t_W, t_{MAJ}) = (2, 5, 0.50, 0.10, 0.5)$  optimizes CPNR for high frequency performance. Accuracy figures for these parameter combinations are provided in Figure 2.16. Polarity maps associated with these settings are provided in Figure 2.17.

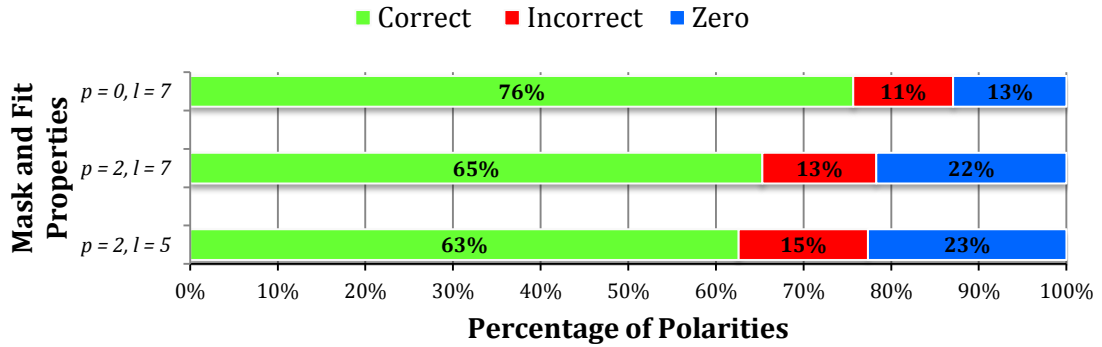


Figure 2.16: Accuracy of CPNR with settings optimized for scale space denoising.

Parameters  $(p, \ell, t_{EST}, t_W, t_{MAJ}) = (0, 7, 0.25, 0.75, 0.6)$  optimize CPNR for low frequency performance,  $(p, \ell, t_{EST}, t_W, t_{MAJ}) = (2, 7, 0.50, 0.50, 0.6)$  optimizes CPNR for mid frequency performance, and  $(p, \ell, t_{EST}, t_W, t_{MAJ}) = (2, 5, 0.50, 0.10, 0.5)$  optimizes CPNR for high frequency performance.

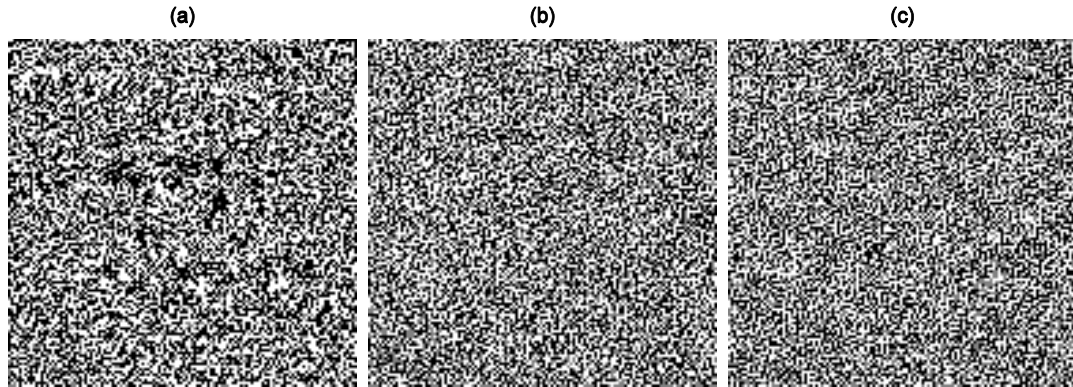


Figure 2.17: Polarity maps corresponding to optimized CPNR protocols.

Polarity maps associated with (a) low frequency CPNR optimization, (b) mid frequency CPNR optimization, and (c) high frequency CPNR optimization.

### 2.3 Subtracted Noise Magnitude and Distribution

The second component of the CPNR equation is the random distribution of subtracted noise values  $R(x, y; \sigma_{N'})$ . As stated in the introduction to this chapter, many noise reduction algorithms attempt to directly estimate the noise magnitude directly from image data, and this can lead to several problems including signal suppression, edge



artifacts, and abnormalities in the residual noise distribution. By contrast, deliberate and informed design of the subtracted noise distribution can lead to a residual noise print with distribution which retains the shape of the original noise intensity distribution; it can also optimize the speed with which the noise reduction algorithm converges to the best possible result. These concerns are addressed in the development of the CPNR noise distribution estimation paradigm.

### 2.3.1 Subtracted Noise Distribution

The rationalization for CPNR in Eq. (2.4) suggests that, by correlating the polarity of the random image noise with noise values from a random distribution, the variance of their difference would be less than the variance of the original image noise. Indeed, a simple computer simulation (Table 2.1) proved that this is the case. Subtracting the values of two normally distributed random variables  $N_1(0, \sigma)$  and  $N_2(0, \sigma)$  with correlated polarities (i.e. positive covariance) results in a third random variable with reduced variance. The variance of the residual can be further reduced through a simple multiplicative variance-reducing optimization factor applied to the subtracted noise distribution. This optimization is easily performed in MATLAB using the *fminbnd.m* command provided in Table 2.2. The optimization routine returns a multiplicative constant  $A = 0.64$  which yields residual noise with  $0.77\sigma$  corresponding to a 41% reduction in noise variance after only a single iteration.

**Table 2.2: MATLAB validation of the optimized CPNR concept.**

---

```
V1 = 1; % Noise variance
S1 = sqrt(V1); % Noise standard deviation
N1 = randn(2^25,1).*S1; % Noise variable 1 (2^25 samples)
N2 = randn(2^25,1).*S1; % Noise variable 2 (2^25 samples)
POL1 = sign(N1); % Polarity of N1
N2 = abs(N2).*POL1; % Correlate polarities of N2 with N1
A = fminbnd(@(a)var(N1(:) - ...
    a.*N2(:)),0,10,...
    optimset('Display','off')); % Optimize the magnitude of N2
N3 = N1-A.*N2; % Subtract A*N2 from N1
VRATIO = var(N3)/V1; % Change in noise variance
```

---

The intensity histograms of the different noise distributions in Table 2.1 and Table 2.2 are provided in Figure 2.18. The original and subtracted noise distributions show excellent agreement with their best-fit Gaussian distribution overlays, but the residual distributions differs significantly from their best-fit Gaussians. Specifically, there is a notable overabundance of both low and high magnitude residual noise values resulting in heavily peaked and heavily tailed distributions which are significantly non-Gaussian (according to Lilliefors' test for distribution normality). [54]

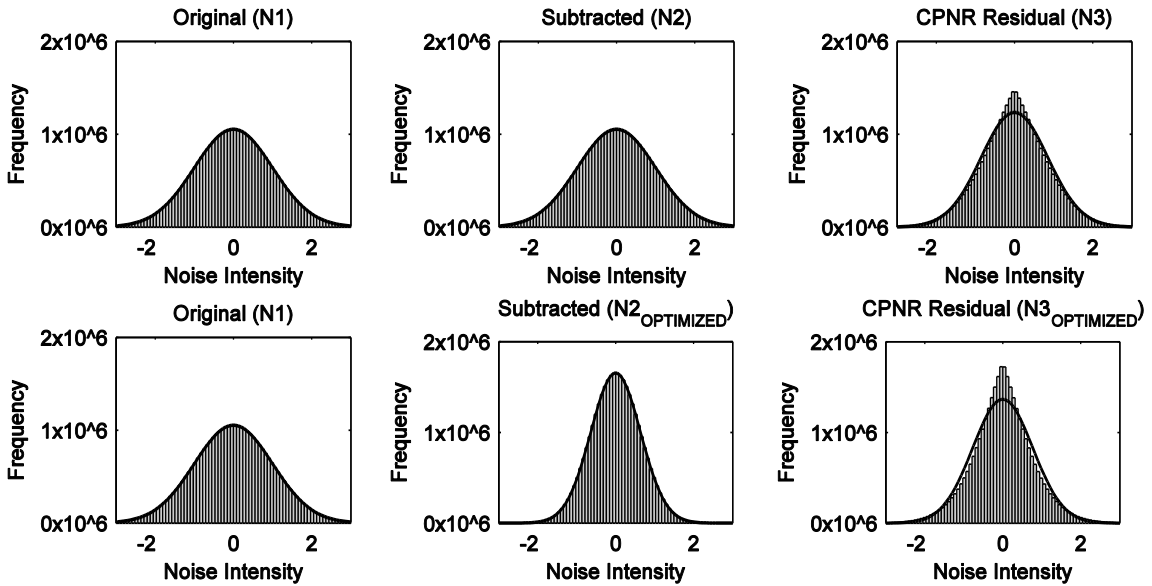


Figure 2.18: Noise intensity distributions from Tables 2.1 and 2.2.

The original and subtracted noise intensities are Gaussian distributed (as evidenced by the Gaussian overlay). However, even when noise polarity is known with 100% accuracy, the residual noise distributions exhibit non-Gaussian characteristics

These tests have been performed to demonstrate a very important principle: noise reduction can be performed simply by correlating the polarities of the original and subtracted noise distributions. This is the key principle behind CPNR. Furthermore, the experiments in Table 2.1 and Table 2.2 have shown that noise reduction is possible without any knowledge of the individual noise magnitudes in the original noise print. It has been shown that noise magnitudes from a random distribution can be used to effectively reduce the noise standard deviation when the polarities of the original noise values are known with sufficient accuracy. In other words, having a sufficiently accurate estimate of image noise polarities and an informed estimate of the noise distribution is all that is necessary to reduce image noise. This is the core principle of the CPNR technique.

### 2.3.2 Subtracted Noise Distribution Optimization

Having demonstrated that the CPNR concept is viable given sufficiently accurate estimates of noise polarity, it may be possible to tailor the subtracted noise magnitude distribution to produce a residual noise print with normal (Gaussian) characteristics. It is desirable to maintain the normal shape of the residual noise distribution, especially under the iterative CPNR paradigm proposed by Eq. (2.4). If residual noise normality cannot be maintained after the first iteration, then the distribution of image noise intensities input into subsequent iterations will be non-normal leading to further distortion of the residual noise distribution. It is therefore important to search for a noise magnitude distribution which, when subtracted from a normal noise distribution using CPNR, yields a residual noise print with sufficiently normal intensity distribution.

The residual noise distributions in Figure 2.18 are heavily peaked and heavily tailed due to two different phenomena. The distorted shape of the residual is partially attributable to situations when very large magnitude values ( $N_2$ ) are subtracted from very small magnitude noise values ( $N_1$ ). Even though the polarities of the original and subtracted noise values are perfectly correlated, the subtraction of very large values results in overcorrection of the noise producing a residual noise magnitude ( $N_3$ ) which is greater than the original. Similarly, when very small magnitude values are subtracted from very large magnitude noise values, the residual noise magnitude remains fairly large. This effect is compounded by incorrect polarities which always increase the noise magnitude and contribute to the heaviness of the residual distribution tails. In order to restore normality, the subtracted noise print should be scaled in such a way that the distribution of noise intensities after subtraction is similar to the distribution of the original (i.e. normal). Furthermore, this correction should be developed within the context of diminished polarity accuracy since

polarity estimation error will undoubtedly affect the distribution of noise intensities after CPNR.

In order to generate a normally distributed CPNR residual noise print, the subtracted noise distribution should be modified. The modified distribution should have two characteristics: reduced probability of very small magnitude values and reduced probability of very large magnitude values. After extensive experimentation with various random distribution types,<sup>5</sup> it was discovered that the Weibull distribution fits these criteria and is capable of producing a residual noise magnitude distribution with more normal characteristics even when noise polarity is not 100% accurate. The probability distribution function (PDF) of the Weibull distribution is formulated as

$$PDF(x; \lambda, k) = \begin{cases} \frac{k}{\lambda} \left(\frac{x}{\lambda}\right)^{k-1} e^{-(x/\lambda)^k}, & x \geq 0 \\ 0, & x < 0, \end{cases} \quad (2.18)$$

with scale parameter  $\lambda$  and shape parameter  $k$ . At different polarity accuracy levels, the Weibull distribution parameters were adjusted to produce residual noise distributions with minimized sum of squared differences with best fit Gaussian distributions. Zero mean Gaussian random noise with  $\sigma = 1$  was processed at 100% , 90%, and 80% polarity accuracy levels to reflect the polarity accuracies anticipated in practical CPNR application. Random values were then selected from Weibull distributions with parameters found in Table 2.3. Histograms of the relevant distributions are provided in Figure 2.19 accompanied by relevant parameters and measurements in Table 2.3.

Although the residual distributions in Figure 2.19 show some differences with the Gaussian overlay, use of the Weibull distribution for noise magnitude estimation has

---

<sup>5</sup> Other random distributions included the gamma, inverse Gaussian, Rician, and uniform distributions.

produced more favorable residual distribution shapes compared to the results when noise magnitudes were drawn from normal distributions (Figure 2.18). Further distribution optimization with more attention to higher order distribution moments may yield further improvements.

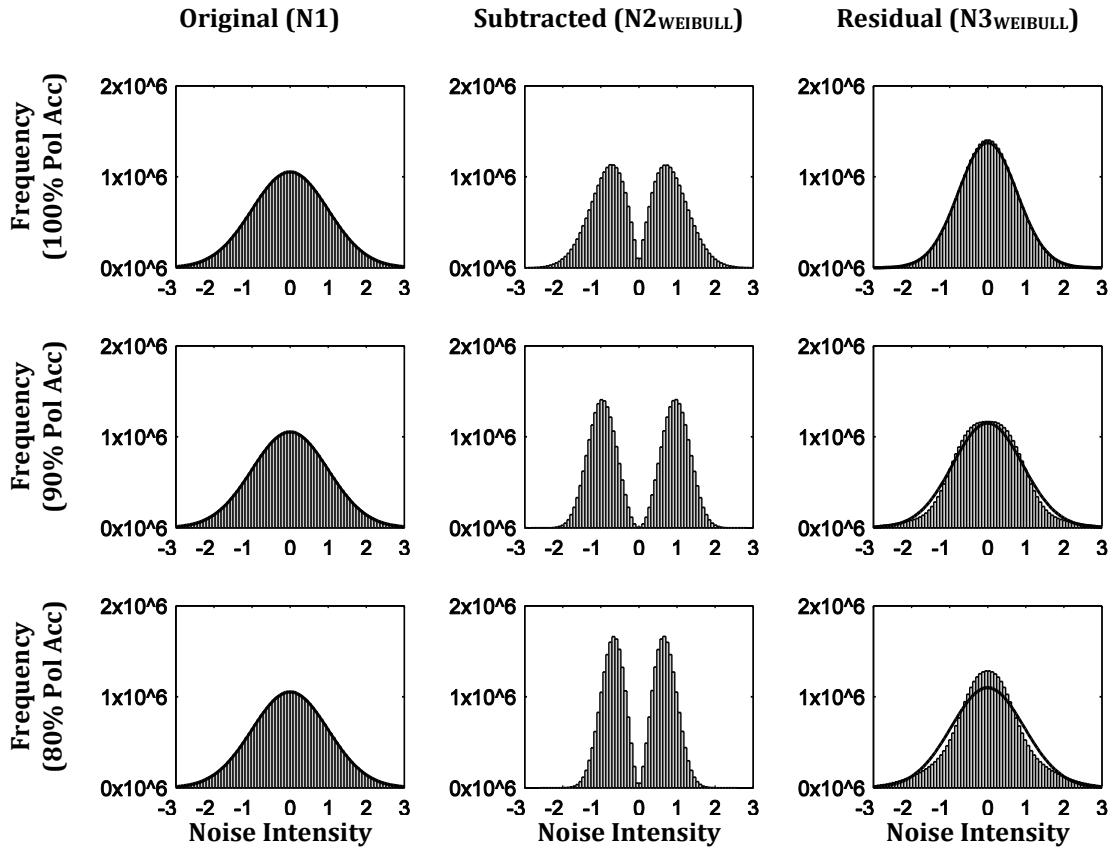


Figure 2.19: Impact of polarity inaccuracy and Weibull noise distribution on CPNR.

Use of the Weibull distribution for CPNR noise magnitude estimation limits the probability of very small and very high magnitude subtracted noise values. Doing so produces residual noise distributions with more normal characteristics. However, the shape of the residual distribution becomes increasingly non-normal with diminished polarity accuracy.

Table 2.3: Parameters and measurements from Figure 2.12.

The selected Weibull distribution parameters maximized the normality of the residual noise intensity distribution.

Polarity Accuracy	Weibull Distribution Parameters		$\sigma_{RESIDUAL}$	Variance Reduction
	$\lambda$	$k$		
100%	$1.0 \times \sigma_{ORIGINAL}$	2.0	$0.77 \times \sigma_{ORIGINAL}$	41%
90%	$1.1 \times \sigma_{ORIGINAL}$	3.0	$0.92 \times \sigma_{ORIGINAL}$	16%
80%	$0.8 \times \sigma_{ORIGINAL}$	2.5	$0.96 \times \sigma_{ORIGINAL}$	8%

## ***2.4 CPNR Application to Radiographic Images***

The optimized CPNR routines described in section 2.2.5 Polarity Estimation combined with the subtracted noise distribution optimizations found in section 2.3.2 Subtracted Noise Distribution Optimization were tested on actual radiographic images. To avoid the exposure of human subjects to multiple x ray examinations, an anthropomorphic chest phantom (Model “Lungman”, Kyoto-Kaguki, Japan) with fine lung insert was imaged in this study. The fine lung insert was used to emulate the anatomy of the human thorax – specifically the fine fibrous detail of the human lung. Images were obtained on an indirect-detection flat panel detector (FPD) (Revolution XQ/i, GE Healthcare, Waukesha, WI) in a laboratory setting. The Bucky-mounted detector has a 41×41 cm<sup>2</sup> field of view (FOV) with 0.2 mm pixel pitch. Other detector properties have been described extensively in the literature. [55, 56] Prior to image acquisition, the system was calibrated with the antiscatter grid installed. The grid (Mitaya Revolution XR/d) had 78 line pairs per cm and a grid ratio of 13:1 with septa focused at 180 cm. The lead septa had thickness of 29 μm with aluminum interspacing and carbon fiber reinforced plastic (CFRP) cover material. In accordance with manufacturer specifications, a 20 mm aluminum block was placed in the beam (for calibration purposes only), and no other hardware was added. The system was then calibrated for gain non-uniformities, offset correction, and defective pixels using the “grid” protocol as specified by the manufacturer. Gain map, offset, and bad pixel corrections constituted the full extent of image pre-processing by the imaging system.

The phantom was placed in the PA position next to the detector with a 3 cm gap between the anterior phantom surface and the detector cover plate. A standard MX 100 x ray tube insert and housing (GE Healthcare, Waukesha, WI) were used with an ULTRANET SA beam collimator (Medys, Monza, Italy) to deliver a full field x ray beam. The system was



set to deliver a 120 kVp beam using a large focal spot (1.25 mm) and 0.2 mm Cu filtration. Two automatic exposure controls behind the lung regions automatically set the tube current to 320 mA for an exposure time of 10 ms (3.2 mAs). This setting delivered an entrance skin exposure (ESE) of 9.6 mR to the posterior phantom surface (measured without the phantom and detector in the beam). This technique reflects what would typically be used in the clinic to image a patient of similar size.

Two images were acquired using the normal technique in order to assess the NPS before and after image processing from subtracted images with different random noise prints. In addition, two images each at half, third, fifth, and tenth exposure were acquired by adjusting the tube current and exposure time to produce the appropriate mAs. These images were acquired to test the effect of processing images at reduced x ray exposure. A sample image has been provided in Figure 2.20.

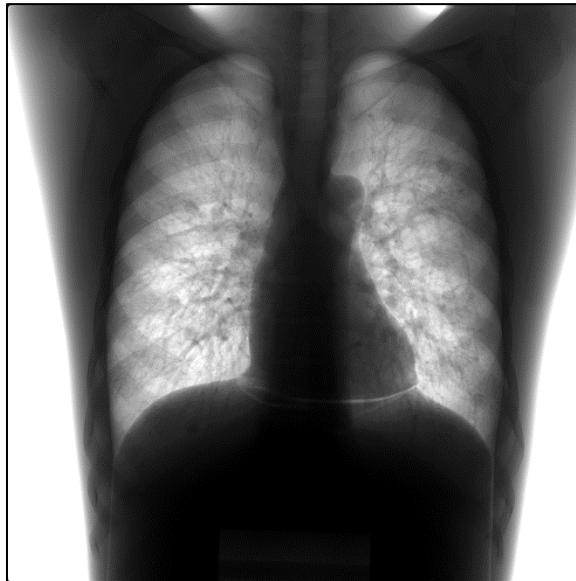


**Figure 2.20: X ray image of the Kyoto phantom at normal clinical exposure.**

### 2.4.1 NPS Analysis

The spatial characteristics of the stochastic noise component of an image can be assessed using the NPS which is defined as

$$NPS(u, v) = \lim_{N_x, N_y \rightarrow \infty} \lim_{M \rightarrow \infty} \frac{N_x N_y \Delta x \Delta y}{M} \sum_{m=1}^M |\mathcal{F}\{I - S\}(x, y)(u, v)|^2. \quad (2.19)$$

The NPS is taken as the ensemble average of the square of the magnitude of the Fourier transform (FT) of the zero mean image noise. [57, 58] The NPS is normalized by the product of the sampling ROI dimensions  $(N_x, N_y)$  and pixel sizes  $(\Delta x, \Delta y)$ . The image noise in Eq. (2.19) is defined as the difference between image data  $I$  and the deterministic signal  $S$ . Since  $S$  is practically impossible to obtain from physical measurements, the difference of two acquisitions  $I_1$  and  $I_2$  can be used to produce an estimate of stochastic noise distribution. Due to the propagation of error imposed by the subtraction operation, the noise image  $I_1 - I_2$  must be normalized by a factor of  $\sqrt{2}$ .

The 1-D NPS in the vertical and horizontal directions associated with the normal dose image in Figure 2.20 is shown in Figure 2.21 using the subtracted image method. A total of 64 128x128 ROIs were used to generate the NPS which employed the methods of Dobbins, *et al.* [57, 59] with 2-D quadratic detrending as recommended by Zhou, *et al.* [60]

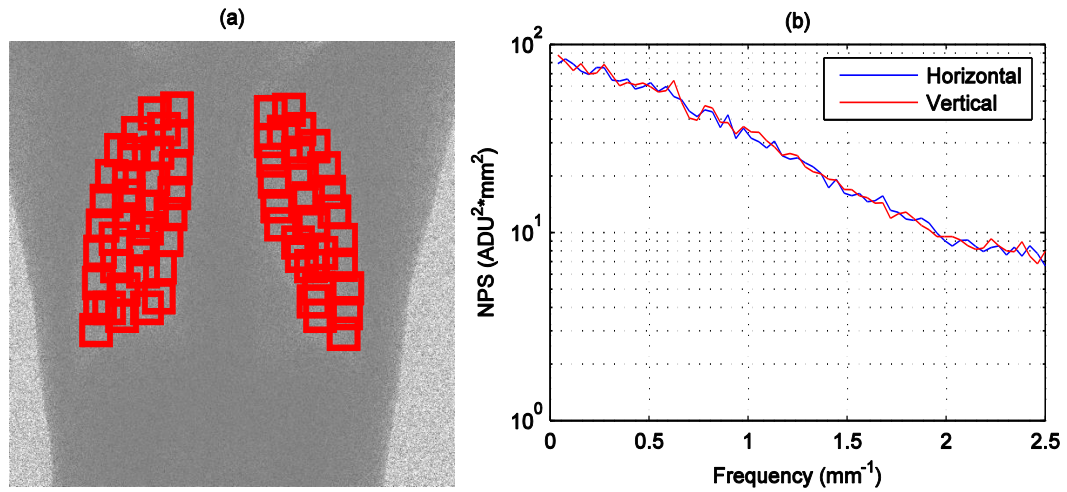


**Figure 2.21: 1-D NPS measured from subtracted Kyoto phantom images.**

The NPS in the lung region of the Kyoto phantom image was assessed. (a) A subtracted image at normal dose is shown with NPS ROIs overlaid in the lung region. (b) 1-D NPS measurements plotted at positive spatial frequencies show spatial correlation of the image noise typical of the indirect detection device studied.

The CPNR parameter sets optimized for low, mid, and high frequency performance were each used to denoise Kyoto phantom images acquired at one-third exposure. In order to compare the amount of noise reduction achieved at one-third exposure to the noise at normal exposure, it is necessary to use the normalized NPS (NNPS):

$$NNPS(u, v) = \frac{NPS(u, v)}{LAS^2}. \quad (2.20)$$

The NNPS is defined as the NPS normalized by the square of the large area signal (LAS). The LAS is a measure of the average pixel gain (intensity) measured in the same units used to determine the NPS which defines the NNPS in units of area. Since x ray noise is Poisson distributed, the noise variance is proportional to the mean photon count. Therefore, in order to effectively compare the noise levels at different exposures, the NPS must be normalized. In Figure 2.22, NNPS from normal and third dose Kyoto phantom images are compared to NNPS measured from subtracted, processed, third dose images

$[CPNR(I_1) - CPNR(I_2)]/\sqrt{2}$  at each of three iterations. Processed images are compared to the original third and normal dose images in Figure 2.26.

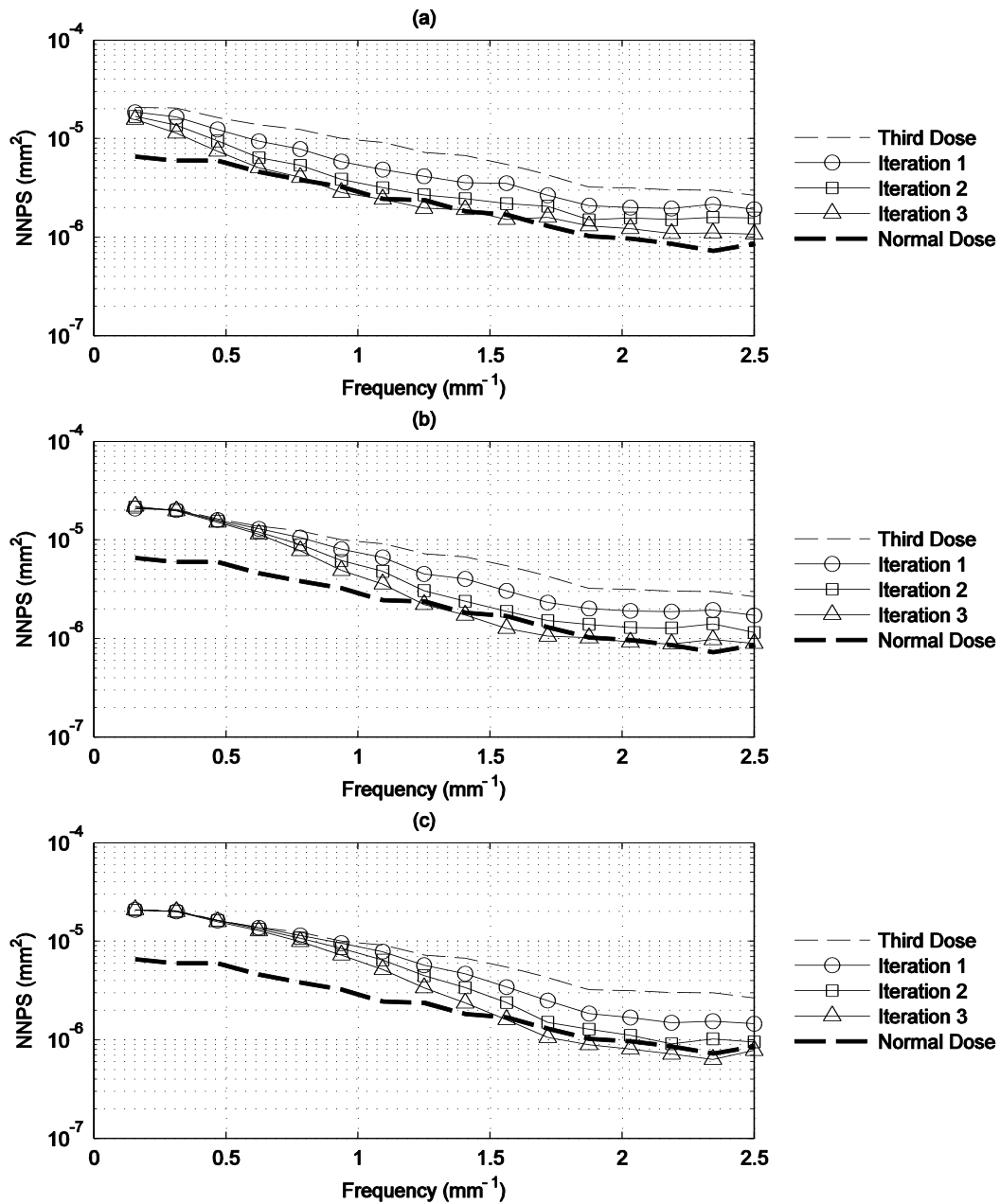
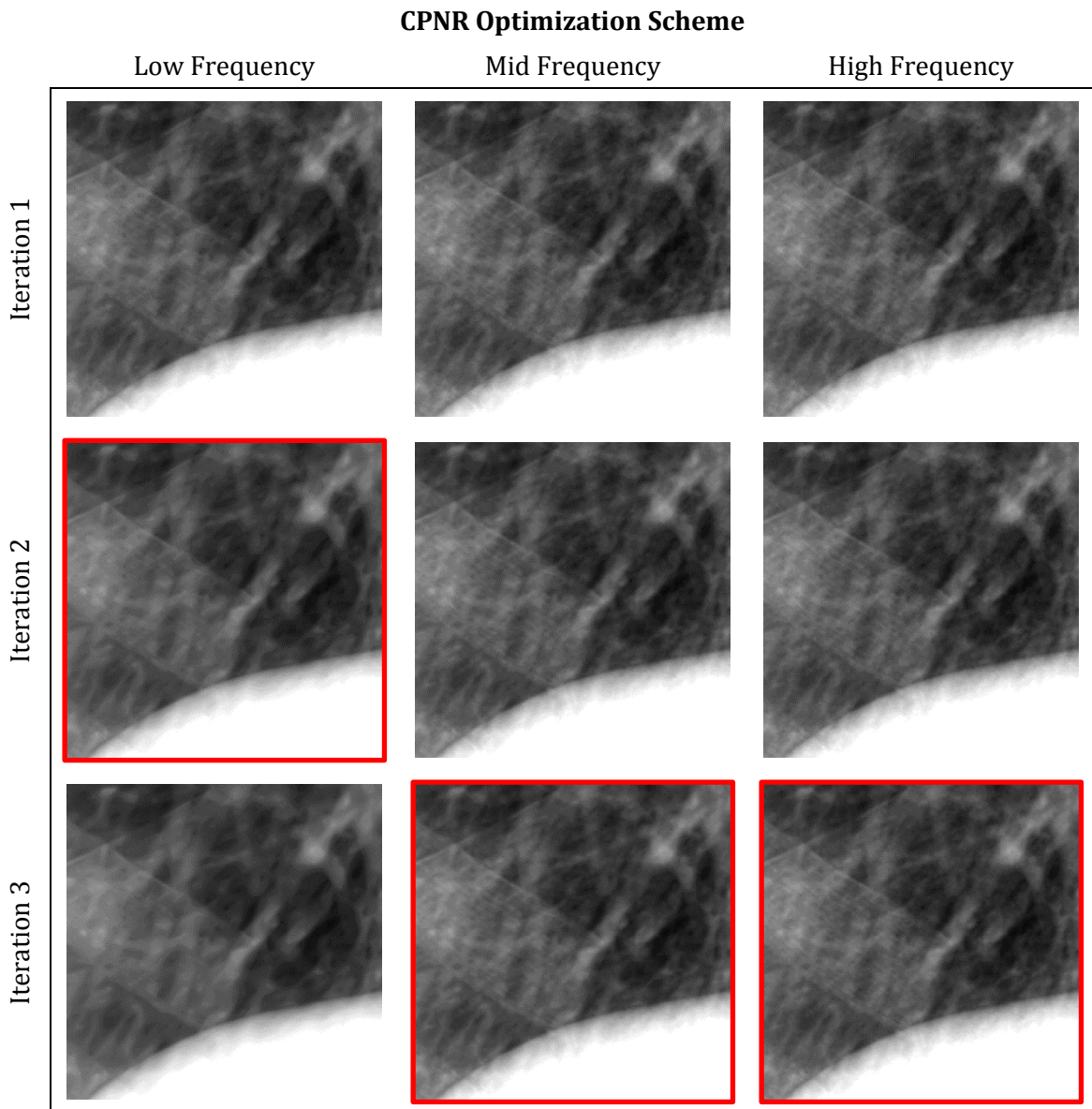


Figure 2.22: NNPS analysis of CPNR-processed Kyoto phantom images.

One-third exposure Kyoto phantom images were processed using three iterations of CPNR with (a) Low frequency optimization, (b) Mid frequency optimization, and (c) High frequency optimization settings. NNPS at each iteration are compared to the NNPS at one-third and normal exposure.



**Figure 2.23: CPNR-processed Kyoto phantom x ray images with log transform.**

Log transformed and CPNR-processed x ray images of the Kyoto phantom are shown at each of three iterations. The noise is iteratively suppressed for each optimization scheme. Anatomical signal is best preserved by the high frequency optimization, but the low and mid frequency noise is better suppressed by the low and mid frequency optimizations, respectively. This is confirmed by the NPS in Figure 2.22. Highlighted images provided a good balance of noise reduction and resolution retention and were input into Eq. (2.23) to produce the final frequency-blended CPNR result.

## 2.4.2 Noise Texture Shaping by Frequency Blending

Within their respective domains, the low, mid, and high frequency optimizations are able to effectively reduce noise variance, and in the case of mid and high frequency processing, noise is suppressed without objectionable blurring of the anatomical signal. The CPNR-processed images in Figure 2.23 show that the high frequency optimization best preserves the high frequency anatomical detail while this detail is suppressed in exchange for better noise reduction by the other lower frequency optimizations. Early results [46] showed an example of frequency blending of CPNR-processed images. The resultant image had more appealing noise texture and resolution properties than either of the component images alone. The best characteristics of each optimization scheme can thus be retained by combining the preferred frequencies from each of the processed images into a single optimal image using a spatial frequency blending algorithm.

$$B_{LP}(f; f_C, n) = \frac{1}{1 + \left(\frac{f}{f_C}\right)^{2n}}. \quad (2.21)$$

The Butterworth low pass filter  $B_{LP}(f)$  is a function of spatial frequency  $f = \sqrt{u^2 + v^2}$  with spatial frequency cutoff parameter  $f_C$  and smoothness parameter  $n$ . Smaller values of  $n$  produce smoother blends of the low and high frequency data, and larger values of  $n$  result in a sharper spatial frequency cutoff at  $f_C$ . As  $n \rightarrow \infty$ ,  $B_{LP}$  approaches an “ideal” low pass filter. To blend the spatial frequency content of two images, a complimentary Butterworth high pass filter is defined as  $B_{HP}(f) = 1 - B_{LP}(f)$ , and the frequency blended image is defined as

$$IM_{BLEND-2} = \mathcal{F}_{2D}^{-1}[\mathcal{F}_{2D}(IM_1) \times B_{LP} + \mathcal{F}_{2D}(IM_2) \times B_{HP}]. \quad (2.22)$$

Likewise, a frequency blend of three images can be achieved through recursive application of Eq. (2.22):

$$\begin{aligned} IM_{BLEND-2} &= \mathcal{F}_{2D}^{-1}[\mathcal{F}_{2D}(IM_1) \times B_{LP1} + \mathcal{F}_{2D}(IM_2) \times B_{HP1}] \\ IM_{BLEND-3} &= \mathcal{F}_{2D}^{-1}[\mathcal{F}_{2D}(IM_{BLEND-2}) \times B_{LP2} + \mathcal{F}_{2D}(IM_3) \times B_{HP2}]. \end{aligned} \quad (2.23)$$

According to the NNPS analysis in Figure 2.22 and review of the processed images in Figure 2.23, a good blend of low, mid, and high frequency CPNR results can be achieved using the highlighted images in Figure 2.23 with the frequency blend settings in Table 2.4. Using Eqs. (2.22) and (2.23), the band passed images in Figure 2.24 show that the noise is suppressed by CPNR in each of the respective frequency bands. Subtracted images contain very little edge information suggesting that resolution is largely preserved within each frequency band.

**Table 2.4: Image frequency blending parameters.**

		$IM_{BLEND-2}$	$IM_{BLEND-3}$
Frequency Blend Parameters	$IM_1$	-	$IM_{LOW}$
	$f_{C1}$	-	$0.50 \text{ mm}^{-1}$
	$n_1$	-	4
	$IM_2$	$IM_{MID}$	$IM_{MID}$
	$f_{C2}$	$1.75 \text{ mm}^{-1}$	$1.75 \text{ mm}^{-1}$
	$n_2$	12	12
	$IM_3$	$IM_{HIGH}$	$IM_{HIGH}$



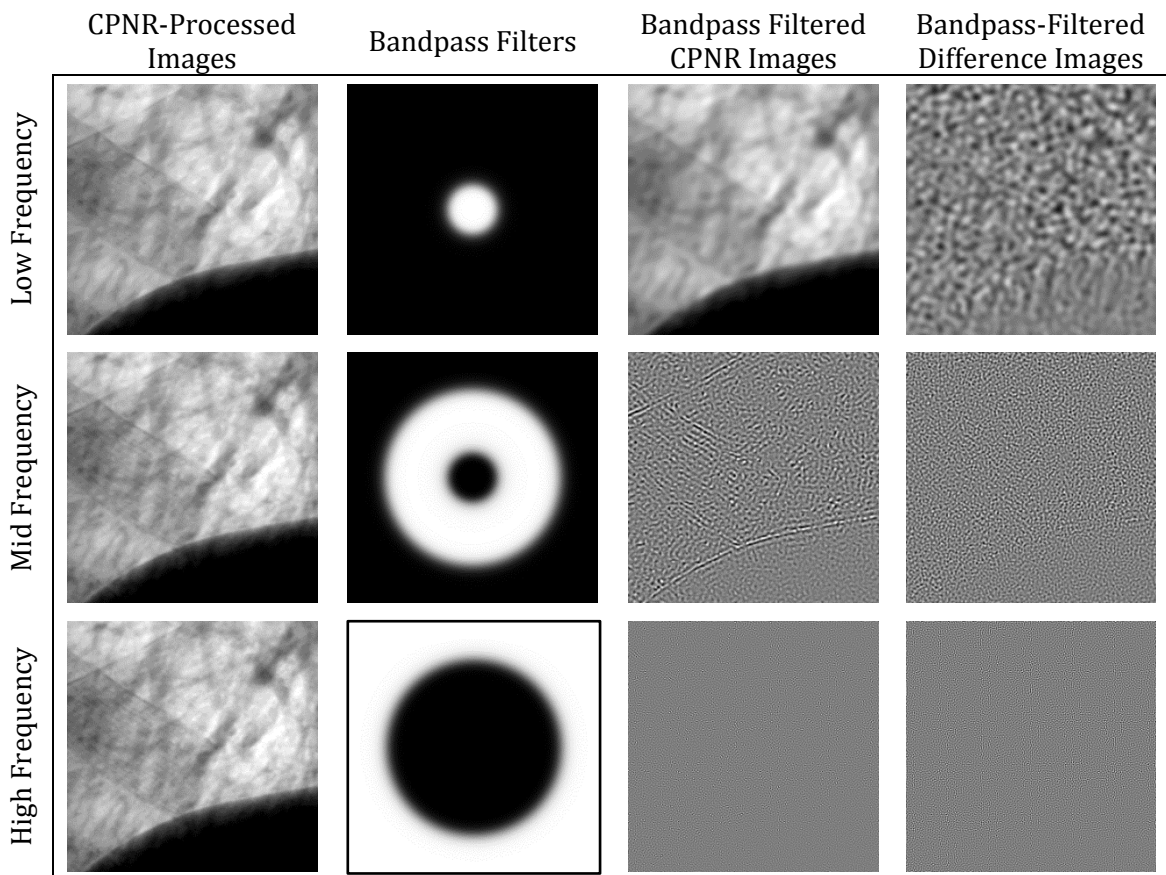


**Figure 2.24: Bandpass filtering of CPNR-processed images.**

Using the band pass cutoffs listed in Table 2.4, low, mid, and high frequency bandpass filters were generated. CPNR-processed one-third exposure images were filtered and subtracted from bandpassed versions of the original third-dose images. The lack of anatomical detail in the subtracted images indicates that resolution is largely preserved through the CPNR process.

The frequency-blended NNPS for two- and three-image blends are displayed in Figure 2.25 showing that the noise variance at mid and high frequencies has been reduced by a factor of three with less variance reduction at lower frequencies. Application of CPNR resulted in total noise variance reduction of 49% in the two-image frequency blended result and 53% in the three-image frequency blended result. The CPNR-processed images in Figure 2.26 show mid and high frequency noise characteristics equal to those of the normal

dose image with minimal degradation of anatomical detail. The residual low frequency noise in the CPNR-processed images does not appear to be objectionable.

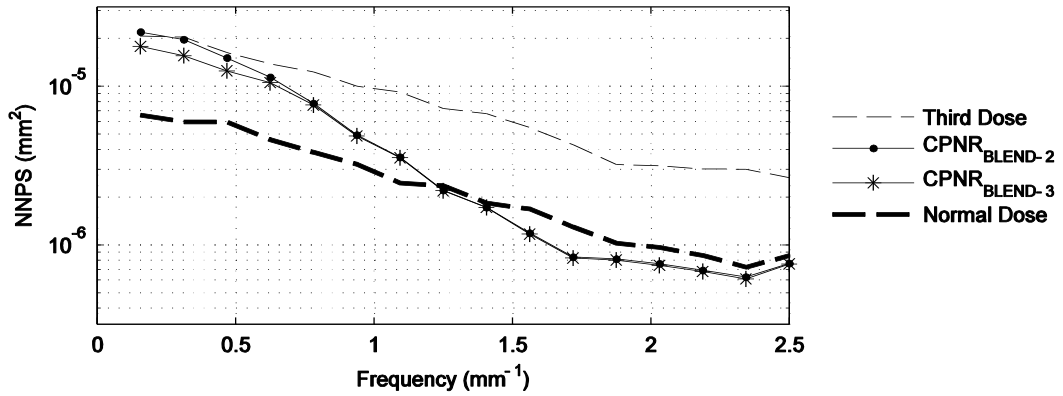
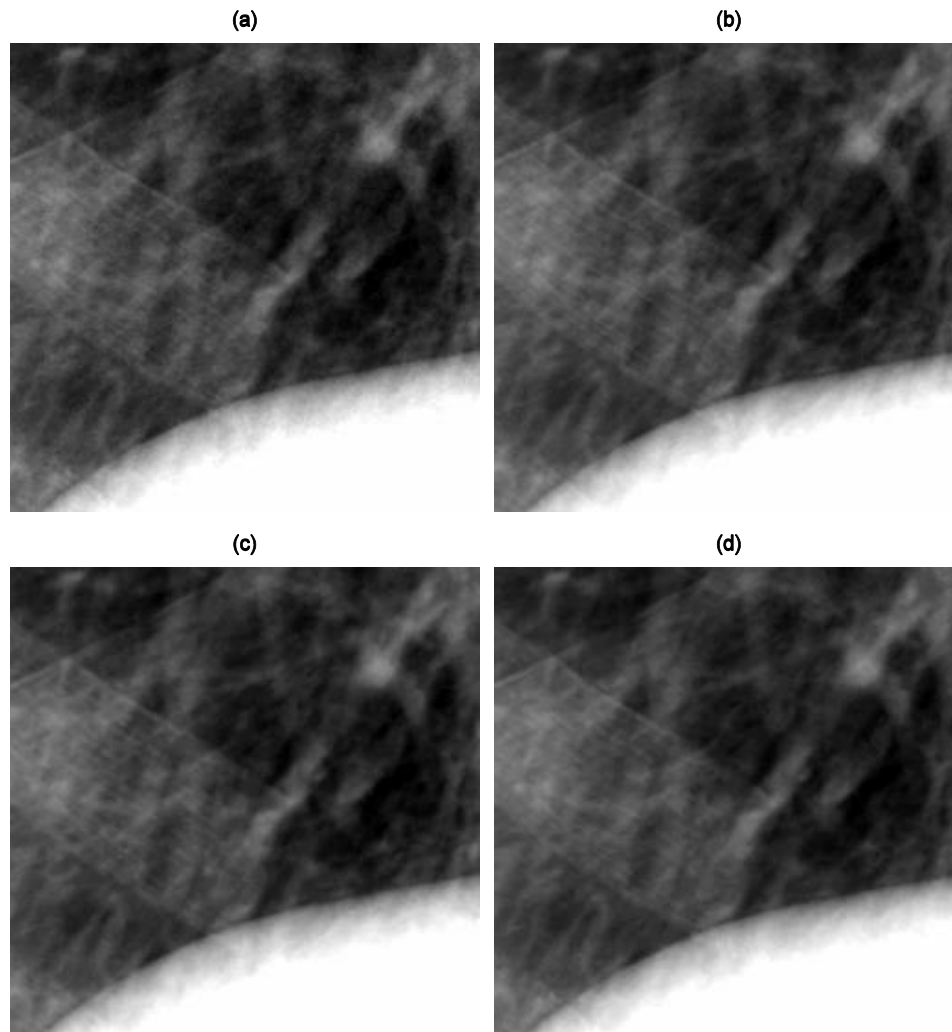


Figure 2.25: NNPS of CPNR frequency blended results.

NNPS for two- and three-image blending after frequency blending of CPNR-processed results improves the best noise reduction properties of the three component images. The incorporation of low-frequency information improves the low frequency noise power, but some low frequency noise still persists.



**Figure 2.26: CPNR-processed results compared to third and full dose images.**

Images are shown after log transformation. (a) One-third exposure image. (b) Normal exposure image. (c) CPNR-processed one-third exposure image with two-image frequency blending. (d) CPNR-processed one-third exposure image with three-image frequency blending. The noise variance at mid and high frequencies in (b-d) is approximately equal with minimal suppression of high frequency anatomical features. The low frequency noise in (d) is slightly better than that in (c) with minimal additional impact on resolution.

## 2.5 CPNR Benchmarking

It is important to know how CPNR compares to other nonlinear image denoising techniques in terms of noise (dose) reduction, noise texture preservation, artifact induction, and resolution performance. While signal resolution and distortion analysis is reserved for Chapter 4, preliminary analysis of noise power performance and artifact induction are conducted in this section as a means of benchmarking CPNR performance. A multitude of denoising techniques are employed throughout the medical imaging field, and based on a thorough review of the medical imaging literature, two of the most popular nonlinear denoising algorithms were chosen for comparison against CPNR.

### 2.5.1 Bilateral Filter

Bilateral filtration is a non-iterative, nonlinear algorithm which uses a simple procedure for edge preserving smoothing. [24] It operates by selective spatial smoothing through the use of both the domain (geometric closeness) and range (photometric similarity) of image data  $I$  according to the function

$$I_{BILATERAL}(x, y) = \sum_{(x_i, y_j) \in \Omega} I(x_i, y_j) G_D(x_i, y_j) G_R(x_i, y_j), \quad (2.24)$$

where  $\Omega$  is a 2-D window centered at  $(x, y)$ .  $G_D(x_i, y_j)$  and  $G_R(x_i, y_j)$  are Gaussian-weighted domain and range functions defined as

$$G_D(x_i, y_j) = e^{-[(x_i-x)^2 + (y_j-y)^2]/2\sigma_D^2}, \quad (2.25)$$

and

$$G_R(x_i, y_j) = e^{-[I(x_i, y_j) - I(x, y)]^2/2\sigma_R^2}. \quad (2.26)$$

Variables  $\sigma_D$  and  $\sigma_R$  are the domain and range smoothing parameters, respectively. The range smoothing parameter is a unique feature of the bilateral filter which is used to

preserve image edges by decreasing the amount of smoothing across large intensity gradients. In fact, the bilateral filter has been shown by several investigators [52, 61, 62] to be derived from the same Bayesian approach as the (iterative) anisotropic diffusion algorithm of Perona and Malik. [37] The anisotropic diffusion technique is another nonlinear, edge-preserving denoising technique which has been extensively and successfully applied in medicine for noise reduction in CT and MRI. [38, 39, 63, 64] Given the success of both the anisotropic diffusion and bilateral filter techniques in medical applications, [24-26, 65-67] the bilateral filter was chosen for demonstration purposes due to its non-iterative nature and smaller parameter space.

## **2.5.2 Wavelet Denoising**

There are many approaches in the literature for the task of denoising, and they can be roughly divided into two categories: denoising in the original signal (spatial) domain and denoising in the transform (frequency) domain. (e.g., by Fourier or wavelet transform). In the 1990s, Donoho *et al.* introduced a means of bridging the gap between spatial (time) domain and transform (frequency) domain processing through the use of wavelets. [68-73] A wavelet is a wave-like oscillation with non-zero amplitude near its center and amplitude which approaches zero in the tails. A sample wavelet is provided in Figure 2.27.

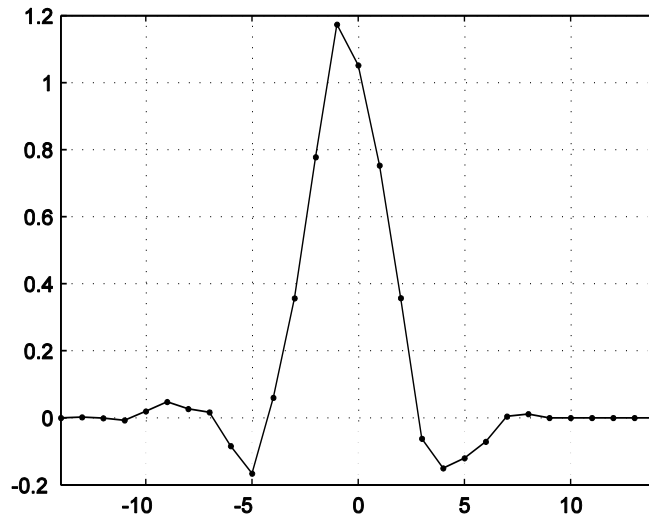


**Figure 2.27: Sample symlet wavelet**

Due to the shape of the wavelet function, wavelet analysis tends to be localized in both time (space) and frequency whereas the sinusoidal basis object used in Fourier analysis is localized only in frequency (i.e. sinusoids propagate *ad infinitum* in the time and spatial domains). This property of wavelets can be used to decompose a signal into different scale spaces for processing. By using multiple image decompositions (resampling with coarser and coarser resolution), denoising can be performed at different image scale spaces. This advantage of wavelet denoising has made it a popular method for denoising medical image data. [28-30, 74, 75]

### 2.5.3 Denoising Algorithm Comparison

To facilitate the fairness of comparison between the bilateral, wavelet, and CPNR algorithms, bilateral and wavelet filter parameters were adjusted to provide the same amount of noise variance reduction as CPNR. This was accomplished by matching the integral of the 2-D NPS after processing a one-third dose Kyoto phantom image. The spatial smoothing parameter of the bilateral filter was fixed at  $\sigma_D = 1$  to prevent excessive spatial

smoothing, and a range smoothing parameter of  $\sigma_R = 24$  reduced the total noise variance by 53% to match CPNR.

The 2-D stationary wavelet transform was used to conduct wavelet denoising. MATLAB's Wavelet Toolbox was used to facilitate the design of the wavelet denoising scheme. By using level three symlet wavelets and a soft threshold of eight, a reasonable wavelet denoising paradigm was achieved which minimized fine detail suppression but also reduced the total noise variance by 53%.

After processing two one-third exposure Kyoto phantom images, NNPS were measured in the lung region from subtracted images and plotted in Figure 2.28. All algorithms are shown to preferentially suppress the mid and high frequency noise with an excess of low frequency residual noise remaining. The  $\text{CPNR}_{\text{BLEND-2}}$  retains slightly more low frequency noise power since low frequency processing was not incorporated in the image blending operation.

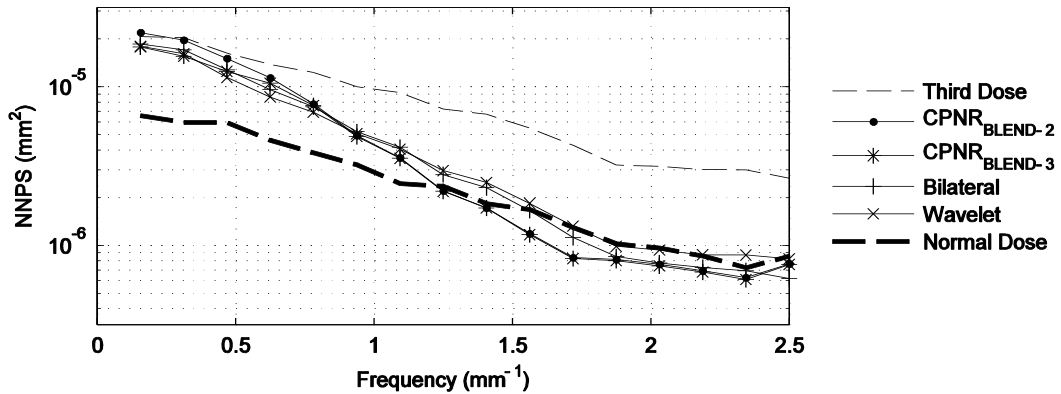


Figure 2.28: NNPS of CPNR compared to bilateral and wavelet denoising.

Algorithm settings were adjusted to reduce the noise variance in a one-third exposure Kyoto phantom image by 53% (except for  $\text{CPNR}_{\text{BLEND-2}}$  which reduced noise variance by 49%). All algorithms preferentially reduce mid and high frequency noise leaving an excess of residual low-frequency noise variance.

Figure 2.29 shows a side-by-side comparison of the processed images along with the difference between the processed images and the original. Each algorithm produces a unique pattern in the difference image which contains subtracted noise, edge blur, and any nonlinear distortion of the image information. The bilateral filter suppresses the noise but does so in a very nonuniform way throughout the image. Furthermore, the presence of edges in the difference image suggests that edge information is being actively suppressed by the algorithm. Wavelet denoising seems to perform better than the bilateral filter both in terms of edge preservation and noise print uniformity, although some edge information has been subtracted. Finally, the CPNR images show good noise reduction with very little edge suppression as evidenced by the lack of signal edge content in the difference images. The CPNR subtracted noise prints appear very uniform with no noticeable artifacts or excessive distortion. Although an excess of low frequency noise remains in the processed images, it does not appear to be objectionable.



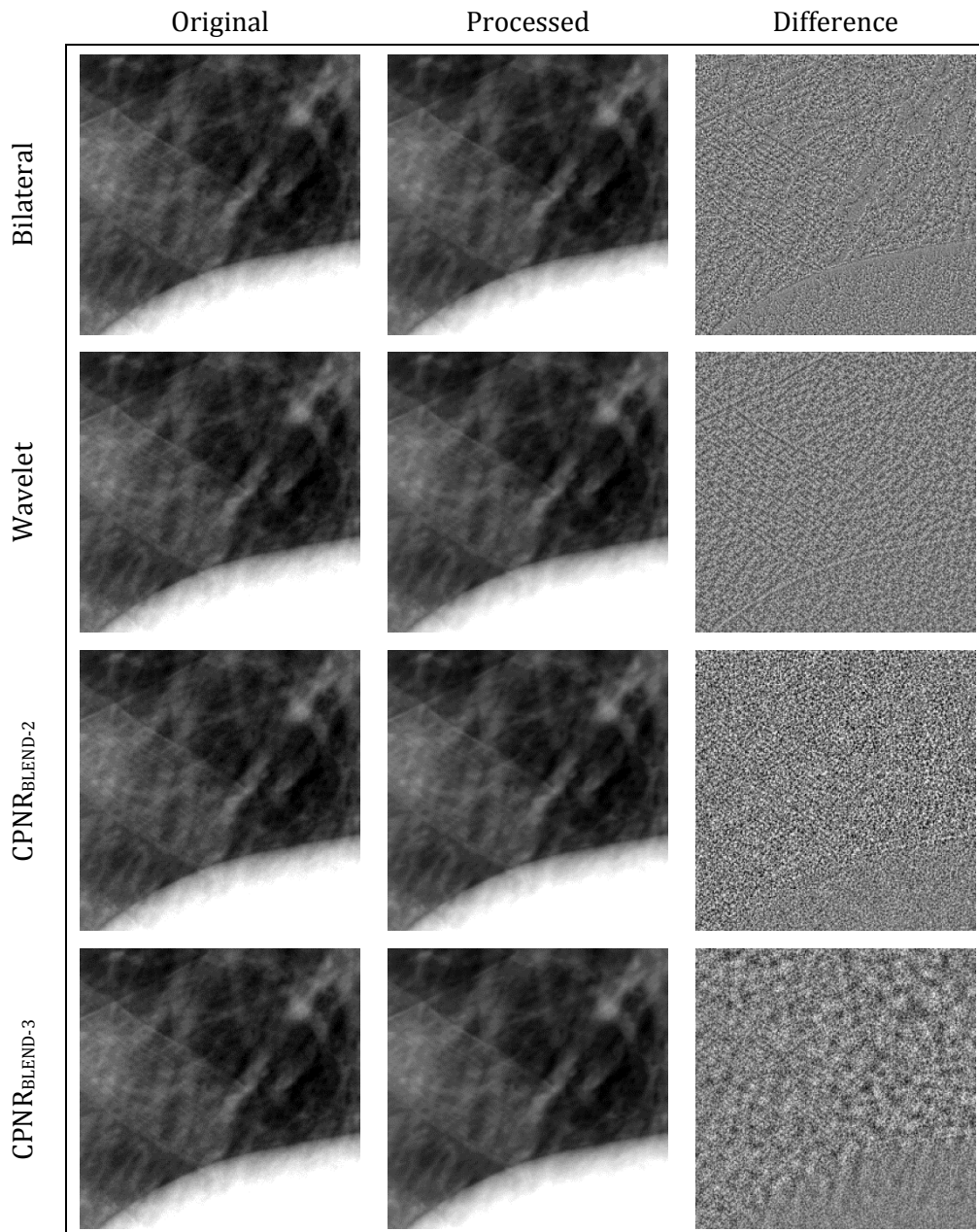


Figure 2.29: Comparison of processed and difference images across algorithms.

Images from three different nonlinear denoising algorithms are compared. Difference images (original minus processed) are provided to show the extent of edge blurring and noise non-uniformity. Each algorithm suppresses image edges to some extent; CPNR appears to suppress edges the least. Also, CPNR and wavelet denoising have fairly uniform noise subtraction throughout the image while the bilateral filter produces noise nonuniformities near high contrast edges.

## ***2.6 CPNR Benefits, Limitations, and Future Work***

Results so far suggest that a two- and possibly three-fold reduction in projection x ray imaging exposure can be achieved with CPNR processing with minimal degradation of the anatomical detail. Based on the preliminary results presented in this work, processed images show suppressed noise variance without objectionable distortion in the distribution of residual noise intensities. No obvious artifacts or signal distortions were observable in the CPNR-processed images. And of the advanced algorithms studied in this chapter (bilateral filtration, wavelet denoising, and CPNR), CPNR appeared (subjectively) to have the least amount of edge blurring.

One objective that remains elusive in spatial denoising is the maintenance of normal noise texture (NPS shape). Specifically, CPNR and other denoising algorithms which operate exclusively in the spatial domain have failed to adequately suppress low frequency noise without significantly suppressing the anatomical signal. This is most probably due to the very high anatomical signal power at low frequencies which prohibits the accurate assessment and suppression of the noise. Figure 2.30 demonstrates that the anatomical signal at low frequencies is many times that of the noise at typical clinical exposure levels. By comparing the signal power of a noise-free XCAT image with that of uncorrelated Poisson noise equivalent to one-third of normal dose, it is apparent that the noise power approximates or exceeds the signal power at mid and high frequencies but is much lower than the signal power at low frequencies. This would explain why the post-processed NPS in Figure 2.28 have shapes which differ from the original image noise – the low frequency noise simply does not have enough power to be properly detected and suppressed. While the problem of suppressing of low-frequency noise in 2-D imaging remains largely unsolved, modest distortions in the noise power at low frequencies may not be a major

impediment to the use of denoising algorithms. Since signal power far exceeds that of the noise at low frequencies, neither algorithms nor human observers may be capable of visualizing the very lowest frequency noise patterns that remain after image denoising.

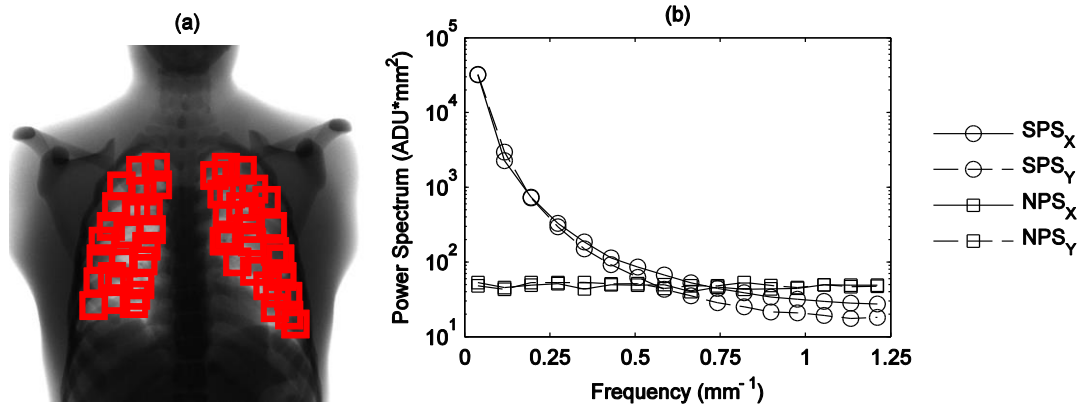


**Figure 2.30: XCAT signal and noise power spectra.**

(a) XCAT simulated chest radiograph at one-third of normal exposure overlaid with 50 ROIs. (b) Signal and noise power spectra measured from the ROIs in (a). At mid and high frequencies, noise power approximates or exceeds signal power. At these frequencies, the noise is readily detected and suppressed without excess suppression of the anatomical signal. However, at low frequencies, signal power is 10-100 times greater than noise power which obscures the noise signal and makes accurate noise assessment more difficult.

Some of the work in this chapter has suggested that some form of scale space processing with CPNR may be justified. It was shown in Figure 2.22 that different CPNR parameter combinations preferentially reduced noise power within different spatial frequency bands. It may be worth exploring the possibility of denoising bandpass filtered images with CPNR. Based on the widespread use of wavelets and the benefits of scale-space denoising, a scale-space (wavelet-based) approach to CPNR denoising may be justified. Along with that, continued investigation of other advanced denoising strategies (such as the nonlocal means algorithm [32-34, 76]) should be a part of ongoing research.

Moving forward, a more detailed investigation of the upper limits of noise reduction in radiographic imaging should be pursued. Any improvements in x ray projection image denoising will have implications in higher dose modalities such as CT (Chapter 5) which uses many projection images of an object to reconstruct a 3-D volume. In the future, other high dose and high dose rate medical imaging modalities like fluoroscopy should also be explored. Applications like fluoroscopy could benefit from advanced denoising algorithms like CPNR but require fast image processing. Recent advancements in parallel computing and graphics processor hardware have made real time execution of algorithms like CPNR more feasible. One final but very important component of CPNR performance optimization is the critical and objective analysis of resolution effects and the potential for nonlinear distortion. This in depth analysis will be explored in Chapter 4.

### 3. Linear Methods for Resolution Performance Analysis

In the search for a proper nonlinear algorithm resolution assessment tool, it is important to first understand and explore methods for linear systems resolution performance analysis. In particular, the modulation transfer function (MTF) has been extensively investigated and applied in the medical imaging literature as evidenced by the many citations and references in this chapter. It is the *de facto* measure of image system resolution performance, and it is important to recognize the role of the MTF in modern imaging research prior to the development of nonlinear resolution assessment tools. Although this chapter will explore the MTF measurement of physical medical imaging devices, the concepts are easily translatable to application in the digital image processing domain.

In this chapter, a detailed review and analysis of two popular techniques for measuring the (1-D) resolution response of medical imaging systems is provided. The assumptions, benefits, and limitations of each method are outlined, investigated, and improved upon. Specifically, theory is developed and applied to ensure adequate fine sampling of the system edge or line spread function (LSF) for 1-D test devices at orientations other than approximately vertical and horizontal. The new formalism is shown to sufficiently generalize the measurement of the 1-D MTF from physical test devices at arbitrary angle. This is presented along with newly derived correction factors which improve measurement accuracy for both edge- and slit-based measurements of the 1-D MTF. Techniques will be validated with experimental measurements on an indirect-detection flat-panel system. In addition to the review and improvement of existing methods for 1-D MTF measurement, a new method for estimating the 2-D system resolution

response using only 1-D test devices is investigated. Validation by synthesis is also performed with simulated images from a hypothetical direct-detection flat-panel device.

The work in this chapter has been previously published in the journal *Medical Physics* and was presented at the 2012 American Association of Physicists in Medicine (AAPM) Annual Meeting. [77, 78]

### ***3.1 The Modulation Transfer Function***

The MTF is widely accepted as the standard measure of linear imaging system resolution performance. It is commonly reported in one dimension as the normalized magnitude of the FT of the LSF which is readily obtained by imaging a slit or edge test device. [79-81] These test devices are typically used to report orthogonal measures of the MTF. While orthogonal measures classify the resolution performance of the system near the two major axes, it has generally been impractical to reliably estimate the off-axis portions of the 2-D MTF.

It would be useful to assess the full 2-D resolution properties of medical imaging systems. For instance, previous reports on the MTF of computed radiography systems have shown distinctive asymmetries in the scan and subscan directions which can make the values at intermediate angles difficult to estimate from orthogonal measurements alone. [82, 83] Examples from digital radiography have also shown that 2-D undersampling and aliasing effects are important to consider, especially in calculations of NEQ and DQE. [55, 59, 84] Complete assessments of the 2-D NEQ and DQE are valuable in assessments of observer task performance since image interpretation is an inherently 2-D task. [83] And although the 2-D NPS is easily measured, regular evaluations of the full 2-D NEQ and DQE have been difficult due to various challenges in obtaining accurate estimates of the 2-D MTF.

Direct measurement of the 2-D MTF has been difficult due to the lack of a suitable 2-D test device and a practical measurement procedure. In a recent effort to measure the 2-D MTF without the use of physical test devices, Kuhls-Gilcrist *et al.* derived an exact relationship between the 2-D NPS and presampled MTF for linear systems. [85] Although accurate, the technique requires in-depth cascaded systems analysis to produce a functional form of the system MTF for fitting purposes. Still, several authors have reported on efforts to develop 2-D resolution test objects. Fetterly *et al.* and Båth *et al.* both demonstrated the use of pinhole test devices for the measurement of 2-D detector point spread function (PSF). [83, 86, 87] Their techniques utilize precision-machined arrays of pinholes to produce “point” sources of x rays, and such devices may not be generally available. Also, to measure the (5×) oversampled and tail-smoothed PSF of a computed radiography system, Fetterly *et al.* required in excess of 6000 individual point-source measurements (obtained from 25 images of a 16×16 matrix of pinholes) for precise computation of the 2-D MTF. [83] Furthermore, opaque pinhole devices may require cumbersome alignment procedures (due to the thickness of the stock material) while non-opaque devices may require background detrending which can affect low-frequency MTF measurements. Other authors have proposed the use of a disk test device and Wiener filtering for the measurement of 2-D MTF. [88, 89] Although this technique requires only a single measurement, reports indicate inaccuracies in 2-D MTF assessment due to aliasing at high frequencies resulting from failure to acquire the presampled MTF. [87] Thus, while these efforts at developing 2-D test objects for MTF are laudable, there still remain issues of practicality and precision in such direct 2-D measurements.

## **3.2 1-D MTF Measurement Methods**

In this section, a simple and accurate method is described for estimating the 2-D MTF using edge and slit test devices that have been routinely used for 1-D MTF measurement. By making measurements with these devices at several angles, an estimate of the 2-D MTF is assembled from an ensemble of 1-D MTF measurements. Methods to ensure adequate fine sampling of edge and slit devices cast at arbitrary angle are also described. The proposed methods are evaluated with experimental measurements on an indirect-detection flat-panel detector (FPD) device and with simulation studies of a direct-detection FPD.

### **3.2.1 Fine Sampling at Arbitrary Angle**

A system LSF can be measured using a variety of techniques. One of the most notable is the technique of Fujita *et al.* [80] who provided a simple method for determining the presampled 1-D MTF using a slit test device. Their methods have been used extensively by many investigators. [56, 79, 81, 82, 87, 90, 91] However the slit method has not been sufficiently generalized to afford presampled MTF estimation at angles which do not approximate the vertical or horizontal. Therefore, an approach toward the generalization of the original MTF estimation method of Fujita *et al.* is derived here which ensures fine-sampling of the LSF at arbitrary angle.

Fine-sampling of the system LSF is required to reduce the effects of aliasing on the measured signal and to recover the presampled MTF. Therefore, a slit-test object must be measured at angles which afford sufficient fine-sampling of the LSF. For a slit at arbitrary angle  $\theta$ , the slope of the projected slit,  $m$ , can be represented using a rational approximation (in simplest form):



$$m = \frac{a}{b} \approx \tan(\theta). \quad (3.1)$$

In Eq. (3.1)  $a$  and  $b$  are integers used to approximate  $\tan(\theta)$ . For the special cases of  $0^\circ = \theta \bmod 180^\circ$  (horizontal) and  $90^\circ = \theta \bmod 180^\circ$  (vertical),  $m = 0/1$  and  $m = 1/0$ , respectively. The simplest-form rational approximation of  $m$  is required in order to accurately determine the sub-pixel sampling resolution achievable at a particular angle. The effective sampling aperture is defined as

$$\Delta s = p/n, \quad (3.2)$$

where pixel dimension  $p$  in the two orthogonal directions is assumed to be equal. Parameter  $n$  is computed from the simplest-form rational approximation in Eq. (3.1) as

$$n = \sqrt{a^2 + b^2}. \quad (3.3)$$

It is evident from Eqs. (3.1), (3.2), and (3.3) that large-integer rational approximations of  $m$  result in large values of  $n$  which in turn provide small effective sampling apertures. In other words,  $1/n$  represents the minimum fractional pixel width achievable through sub-pixel sampling of a 1-D resolution test signal at angle  $\theta \approx \tan^{-1}(m)$ . This distinction is an important generalization of statements made by both Fujita *et al.* [80] and Samei *et al.* [81] Given our definitions in the equations above, we conclude that a slit or edge at an angle with  $1/n$  greater than some predefined value for  $\Delta s/p$  will provide inadequate sub-pixel resolution. At these angles, the coarseness of sub-pixel sample spacing may lead to aliasing in the response function. Therefore, a 1-D resolution test device imaged at any other angle with sufficiently small  $1/n$  will yield adequate results.

Finally, once a satisfactory angle is found, the finely-sampled LSF can be obtained as a function of pixel distance  $d$  from the slit center

$$d = \frac{y - (mx + y_0)}{\sqrt{m^2 + 1}}, \quad (3.4)$$

where  $d$  is the exact perpendicular distance from pixel center coordinate  $(x, y)$  to the center of the imaged slit defined by slope  $m$  and  $y$ -intercept  $y_0$ . Simple arrangement of pixel values as a function of increasing  $d$  between  $\pm d_0$  (Figure 3.1) forms a precise estimate of the finely-sampled LSF.

### 3.2.2 Slit Non-Uniformity

One hurdle to physical implementation of slit-based measurements of MTF at arbitrary angle is the absence of a generalized uniformity correction for imperfections in the slit. Slight inaccuracies in slit fabrication due to imprecision in machining may result in slit width variation leading to non-uniformities in x ray transmission along the length of the test device. In a previous report, [82] slit width imperfection was corrected by normalizing the intensity of pixel values by the integral intensity across the slit in a direction perpendicular to the slit for slits positioned near the image axes. This approach has been extended for application at arbitrary angle.

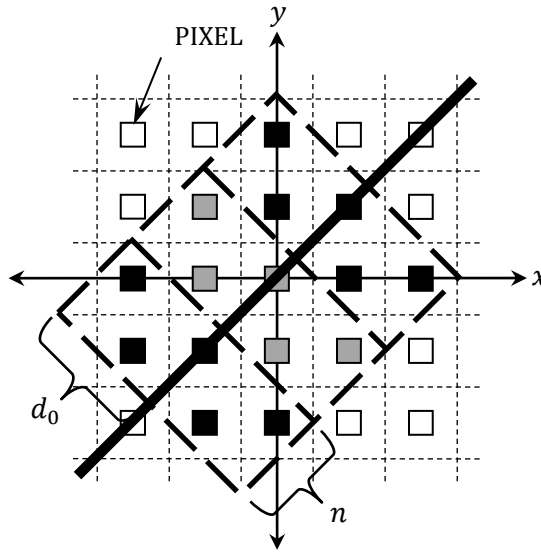


**Figure 3.1: Slit geometry.**

**Perpendicular slit profiles (thick dashed rectangular enclosures) shown for a slit at or near  $45^\circ$ . For  $\theta \approx 45^\circ$ ,  $\tan(\theta) \approx 1/1 = a/b = m$ . Variables  $n$  and  $d_0$  are displayed for convenience. Alternating black and gray pixel centers indicate a particular pixel's profile membership. Pixels with white centers are ignored.**

The new approach to slit non-uniformity correction involves rounding the slit angle to one that permits estimation of  $m$  using small integers  $a$  and  $b$  [Eq. (3.1)]. The small-integer approximation of  $m$  results in a relatively small value for  $n$  [Eq. (3.3)] which can be interpreted as the regular interval (in pixels) approximately parallel to the slit at which consecutive perpendicular profiles should be formed. Note that the small-integer approximation of  $m$  is recommended exclusively for the purposes of slit non-uniformity correction and not for the construction of the finely-sampled LSF due to the potential for aliasing in the response function. For example, non-uniformity correction of an approximately horizontal slit involves normalization of pixel values to the integral of vertical profiles at regular increments along the  $0^\circ$  direction ( $m = 0/1$ ). At  $0^\circ$ ,  $n = 1$  implying that profiles should be generated at 1-pixel increments along the slope  $m = 0$ . In

another example, a slit at  $44^\circ$  ( $m \approx 28/29$ ) requires non-uniformity correction using profiles perpendicular to the  $45^\circ$  direction ( $m = 1/1$ ). At  $45^\circ$ ,  $n = 1.414$  indicating that non-uniformity correction can be achieved through pixel value normalization by the perpendicular profile integral obtained at increments of 1.414 pixels along the  $45^\circ$  angle (Figure 3.1). This same procedure can be implemented at any other angle thus generalizing the slit non-uniformity correction technique.

### **3.2.3 Experimental Implementation with an Indirect Detection Device**

The measurement of MTF at angles between horizontal and vertical was demonstrated on an indirect-detection FPD using both edge and slit devices.

#### **3.2.3.1 Imaging System**

An indirect-detection FPD (Revolution XQ/i, GE Healthcare, Waukesha, WI) was investigated in a laboratory setting. The Bucky-mounted detector has a  $41 \times 41$  cm<sup>2</sup> field of view (FOV) with 0.2 mm pixel pitch. Other detector properties have been described extensively in the literature. [55, 56] A standard MX 100 x ray tube insert and housing (GE Healthcare, Waukesha, WI) were used with an ULTRANET SA beam collimator (Medys, Monza, Italy). The source-to-image distance was 186 cm.

Prior to system calibration, several pieces of hardware were removed from the x ray beam: beam conditioning filters; collimator-mounted crosshairs and exposure meter; detector cover plate; antiscatter grid; and the automatic exposure control. In accordance with manufacturer specifications, a 20 mm aluminum block was placed in the beam (for calibration purposes only). No other hardware was added. The system was then calibrated for gain non-uniformities, offset correction, and defective pixels using the “no grid” protocol as specified by the manufacturer. Previous studies showed that the system response

function demonstrated excellent linearity within the relevant exposure range,<sup>1</sup> hence raw images required no linearization correction. Gain map, offset, and bad pixel corrections constituted the full extent of image pre-processing by the imaging system.

### **3.2.3.2 Beam Conditions**

The x ray beam was conditioned in accordance with the IEC RQA5 standard which requires a 21 mm aluminum block in the beam. [92, 93] Standard shop-grade aluminum (type-1100) was used following the findings in a previous publication. [94] To approximate narrow beam geometry, the beam was first tightly windowed with the system's internal collimator followed by a second lead collimator attached to the detector side of the aluminum block. With phantom and collimators in place, the IEC-specified half-value layer of 6.8 mm Al was achieved at 71.5 kV<sub>p</sub> in accordance with the RQA5 beam quality requirements. [92, 93] Exposure measurements for half-value layer calculation were made using a calibrated ionization chamber and kV meter (Accu-Pro, MDH Model 1015, 10X5-6 ionization chamber, Radcal, Morovia, CA). The chamber was positioned 93 cm from the source for all exposure measurements made in this study.

All beam conditions associated with MTF measurements closely followed the IEC standard with one exception: The x ray exposure was set to the maximum value allowed by the system. The technique was fixed at 71.5 kVp, 64 mAs, 250 mA, 250 ms, and 0.6 mm nominal focal spot for all MTF test images in this study. It provided an exposure of 4.0 mR at the detector (higher than the IEC recommendation). Other investigations have shown that this deviation from the prescribed protocol is justified in order to reduce the influence of image noise since the MTF of digital FPDs rarely exhibit substantial exposure dependency. [79, 81]

### 3.2.3.3 Edge Image Acquisition

An opaque edge was used in the first set of physical measurements of MTF. It consisted of a  $0.2 \times 5 \times 10 \text{ cm}^3$  tungsten slab with one polished edge (TX5 W Edge Test Device, Scanditronix Wellhöffer, Schwarzenbruck, Germany). The other three edges were surrounded by a 3 mm thick lead frame. The edge test device was placed in contact with the system carbon-fiber cover plate and visually aligned with the central axis of the x ray beam. To ensure proper alignment of the beam axis, detector center, and edge, a bubble level was used to measure and correct for any sagging of the x ray tube housing and detector Bucky. After verification of system alignment, the x ray beam was collimated to  $8 \times 8 \text{ cm}^2$  at the detector. This ensured proper exposure of the full length of the available edge without exposing the lead frame. The edge was rotated and imaged through a total of ten angles between  $0^\circ$  (horizontal) and  $90^\circ$  (vertical). It was supported at each angle by wooden wedges and fixed in place with common tape. At each angle, the entire collimator assembly was rotated to align the square x ray field with the edge. Five images were acquired at every edge orientation with at least two minutes between each acquisition to minimize the influence of detector lag. The repeated measurements at each angle were taken to compute the uncertainty in 2-D edge-based MTF assessments.

### 3.2.3.4 Edge Image Processing

The method of Samei *et al.* [81] was used to process the individual edge images at each angle. Edges were extracted using a  $256 \times 256 \text{ pixel}^2$  ROI. A binary threshold operation was applied to the edge data in the ROI, [95] and the edge was extracted using Canny edge detection. [96] The edge angle was determined using a double Hough transform with  $0.1^\circ$  precision. Each of the five edge images at each angle were processed independently, and key measurements are summarized in Table 3.. The data were projected parallel to each edge

and rebinned with 0.02 mm (0.1 pixel) spacing to form the finely-sampled edge spread function (ESF).

**Table 3.1: Summary of values obtained from physical edge measurement.**

Using the estimated edge angles,  $a/b$  ratios were obtained using the MATLAB function *rat* with tolerance factor of 0.001. Parameter  $n$  indicates that all edge angles can accommodate fine-sampling of the ESF with sub-pixel sampling bins which are at least 10× smaller than the physical pixel dimension.

Parameter	Acquisition									
	1	2	3	4	5	6	7	8	9	10
$\theta$	1.33°	7.59°	20.22°	30.29°	37.90°	48.07°	58.85°	69.78°	78.13°	88.02°
$a/b$	1/43	2/15	7/19	7/12	7/9	59/53	43/26	19/7	157/33	781/27
$n$	43.01	15.13	20.25	13.89	11.40	79.31	50.25	20.25	160.43	781.47

In order to reduce the impact of noise in the finely-sampled ESF measurement, two denoising methods were compared. One method employed modest smoothing with a Gaussian-weighted polynomial kernel (0.34 mm width, 4<sup>th</sup>-order polynomial fitting) according to the recommendations of Samei *et al.* [81] Alternatively, the ESF was conditioned using the algorithm of Maidment and Albert. [97] Whereas smoothing of the ESF has been shown to introduce systematic errors in the estimation of the MTF (namely amplitude suppression at high frequencies), the ESF conditioning algorithm has been shown to preserve fine features of the MTF. [97] This is accomplished by constraining the ESF data through quadratic optimization according to two requirements: monotonicity of the ESF and squared error minimization. Results using the ESF conditioning algorithm are compared to the Gaussian-weighted polynomial smoothing algorithm in Sections 3.3 and 3.4.

After denoising the finely-sampled ESF, differentiation using the standard central-difference algorithm produced the LSF. A sample LSF from an approximately horizontal edge is shown in Figure 3.2 without denoising, with smoothing, and with conditioning. To

remove low-frequency nonuniformities, the baseline of the LSF was subtracted using a linear fit to 1 cm portions of the LSF tails. This was followed by windowing with a Hanning window of 2 cm width. The 1-D FT of the windowed LSF produced the optical transfer function (OTF). The magnitude of the complex OTF normalized to unity at zero frequency formed the MTF with bin spacing of  $0.05 \text{ mm}^{-1}$ . An iterative process refined the edge angle estimate down to  $0.01^\circ$  precision through maximization of the integral of the MTF between the zero (DC) and cutoff ( $f_c$ ) frequencies.

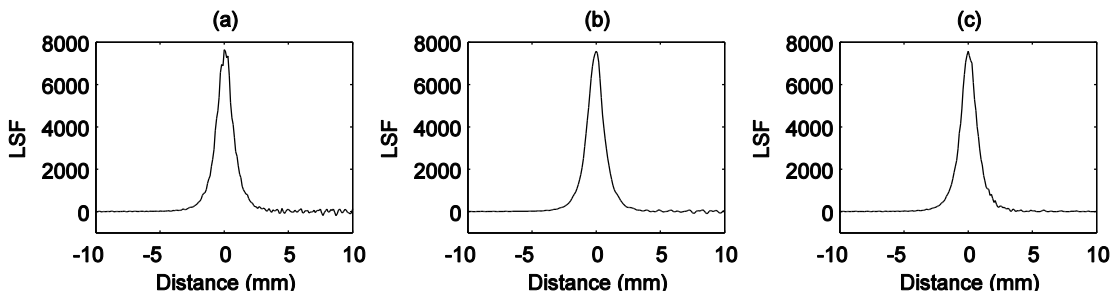


**Figure 3.2: LSF following numerical differentiation of a finely sampled edge.**

**The edge device was imaged at  $1.33^\circ$ . Results shown (a) without denoising, (b) with smoothing, and (c) with conditioning. The effects of denoising are most evident on the positive side of the LSF which corresponds to the unattenuated side of the edge.**

At this point in edge image processing, it was recognized that two correction factors could be used to improve the edge method of Samei *et al.* [81] First, their sub-pixel binning procedure is in effect the convolution of a rectangular function of sub-pixel width with the finely-sampled 1-D ESF data. Therefore, the resultant MTF should be corrected through division by  $|\text{sinc}(\Delta s \sqrt{u^2 + v^2})|$  where variables  $u$  and  $v$  are spatial frequencies in the horizontal and vertical directions, respectively. Second, differentiation using the standard central-difference algorithm introduces additional blurring effects which should be modeled to correct the MTF. For evenly-spaced data, the central-difference algorithm is



simply the average of the forward and backward (two-point) differences. The averaging process may be modeled as a convolution of the resultant LSF by a rectangular function of width equal to two sub-pixel bins – a correction which is easily applied through division of the MTF by  $|\text{sinc}(2\Delta s\sqrt{u^2 + v^2})|$ . This correction, which is equivalent to the transfer function of the central differences algorithm, is consistent with the findings of Buhr *et al.* [98]

Once the corrected 1-D MTF estimates at each of ten angles was obtained, the 2-D MTF was estimated through a simple surface fit to the ensemble of 1-D data. Due to the symmetry of the detector elements in our studies, we assumed reflective symmetry of the 2-D PSF across both the  $x$  and  $y$  axes. Therefore, the 1-D MTF measurements generated from edge images between  $0^\circ$  and  $90^\circ$  were reflected across the  $u$  and  $v$  axes to fill the remainder of 2-D frequency space in advance of data interpolation onto a  $192 \times 192$  Cartesian lattice with evenly-spaced samples between  $\pm 1.5f_c = \pm 3.75 \text{ mm}^{-1}$ . This grid size was chosen based on the recommended size for 2-D NPS measurements from a previous study. [58] Consistency between the MTF and NPS grid sizes is important for the purposes of 2-D DQE and NEQ computations. [55, 59, 82, 84, 87] Finally, the ensemble of 1-D MTF data was interpolated onto the 2-D grid using three interpolation methods: nearest neighbor, linear, and cubic interpolation. All interpolation methods were based on Delaunay triangulation due to the scattered (unevenly sampled) nature of the source data. Comparisons of the accuracy and precision of these interpolation methods are reported in the Results section.

### **3.2.3.5 Slit Image Acquisition**

A narrow slit test device was imaged to compare against results from the edge method. A sturdy aluminum jig held two 2 mm thick lead blocks with highly polished edges

spaced 12  $\mu\text{m}$  apart. The slit was positioned in the center of a 35×35 mm<sup>2</sup> aluminum window. Following the same tube and Bucky alignment procedure as with the edge, the slit was positioned 1 cm from the system cover plate near the center of the imaging plate. The beam apertures were set to deliver a 3.5×3.5 cm<sup>2</sup> field at the detector to avoid excessive exposure of the aluminum frame. The slit was imaged at three orientations: vertical, horizontal, and 45°. At each position, the slit was adjusted so that its angle was 1-4° off of true vertical, horizontal, and 45° alignment. An iterative alignment procedure was implemented to maximize the x ray flux through the slit indicating optimal slit positioning. [82] Once aligned, the slit was imaged 20 times with at least two minutes between each acquisition to minimize the effects of detector lag.

#### **3.2.3.6 Slit Image Processing**

The generalizations described in the sections above were applied to the methods of Fujita *et al.* and Dobbins *et al.* which both served as guides for slit processing. [80-82] At each angle, the 20 slit images were averaged to form a single composite image which reduced the influence of noise. Slits were extracted using a 160×160 pixel<sup>2</sup> region of interest (ROI). In a process similar to that implemented for the edge, slit angle was determined using a double Hough transform following thresholding and morphological skeletonization of the slit image. This yielded slit angle measurements of 4.15°, 44.07°, and 87.03°. Irregularities in pixel intensity due to non-uniformities in slit width were corrected using the technique proposed in section 3.2.2 Slit Non-Uniformity. Finally, the finely-sampled LSF was found using the same binning operation described for the edge (0.02 mm sub-pixel bins).

To promote consistency between LSF measurements, the LSF tails were extrapolated exponentially beyond 1% of the peak value following the work of other

authors. [80, 82, 99] A sample LSF is shown in Figure 3.3 before and after extrapolation. Following extrapolation and 1-D FT of the LSF, the magnitude of the complex OTF was normalized to unity at zero frequency to form the MTF. Finally, two correction factors were applied to the MTF. It was first corrected through division by  $\text{sinc}[(14 \mu\text{m})\sqrt{u^2 + v^2}]$  to account for the finite width of the slit, its magnification, and focal spot blur. The measure of  $14 \mu\text{m}$  is a value derived from past work with the same slit test device. [82] Then, the MTF was corrected for the blur due to sub-pixel binning through division by  $|\text{sinc}(\Delta s\sqrt{u^2 + v^2})|$ .

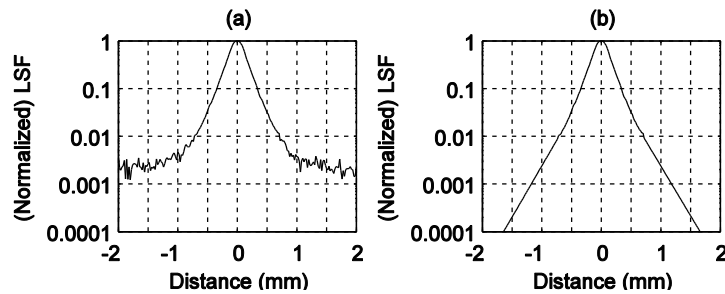


Figure 3.3: Normalized LSF from a slit at  $4.15^\circ$ .

The LSF is shown (a) before and (b) after exponential extrapolation below the 0.01 level.

### 3.2.4 Validation by Synthesis with a Hypothetical Direct Detection Device

#### 3.2.4.1 2-D MTF Simulation

To better understand the utility of 2-D MTF estimation techniques, test images were synthesized assuming a hypothetical direct-detection FPD device. The direct-detection device was chosen in order to estimate the 2-D MTF in a case where a substantial amount of aliasing is likely to be present. The blurring function of the hypothetical detector was approximated by the square pixel aperture function modeled as a rectangular window of height  $h_a$  and width  $w_a$ . [14, 98, 100] This blurring function is associated with the following presampled MTF:

$$MTF_{\text{aperture}}(\rho, \theta) = |\text{sinc}(\rho w_a \cos \theta) \text{sinc}(\rho h_a \sin \theta)|. \quad (3.5)$$

In Eq. (3.5),  $MTF_{\text{aperture}}(\rho, \theta)$  is described by polar coordinates  $\rho$  and  $\theta$ . In terms of the more traditional Cartesian coordinates, radial spatial frequency variable  $\rho = \sqrt{u^2 + v^2}$  and  $\theta = \tan^{-1}(v/u)$  is the polar angle. The effects of detector MTF were incorporated into the simulation model which is described in full mathematical detail in Appendix A: Synthesis of Digitized Slit and Edge Objects with System Blurring Effects. A graphical description of model variables is provided in Figure A.1.

To test the precision and accuracy of the methods, the 2-D MTF of the hypothetical direct-detection device was estimated from ten simulated edge images. The angles of the edges in each image were evenly spaced between  $0^\circ$  and  $90^\circ$  at the angles shown in Table 3.2. Images were synthesized by executing Eq. (A.8) using Simpson's trapezoid rule for numerical integration with 200001 evenly-spaced spatial frequency locations between -50 and  $50 \text{ mm}^{-1}$  with parameters  $\omega = 125 \text{ mm}$  and  $\ell = \omega/2$  on a  $384 \times 384$  pixel<sup>2</sup> lattice. Pixels were square with pitch of 0.2 mm, and simulated pixel intensities in all images ranged from 10 to 16383. Poisson random noise was added to the simulated edge images. Finally, the presampled MTF was estimated at each angle and the 2-D MTF estimate constructed in accordance with the procedures outlined in section 3.2.3.4 Edge Image Processing. Results were plotted in the range  $\pm 4f_c = \pm 10 \text{ mm}^{-1}$  in the  $u$  and  $v$  directions on an evenly sampled  $512 \times 512$  Cartesian lattice.

**Table 3.2: Summary of values obtained from simulated edge measurement.**

Using the estimated edge angles,  $a/b$  ratios were obtained using the MATLAB function *rat* with tolerance factor of 0.001. Parameter  $n$  indicates that all edge angles can accommodate fine-sampling of the ESF with sub-pixel sampling bins which are at least  $10\times$  smaller than the physical pixel dimension.

Parameter	Acquisition									
	1	2	3	4	5	6	7	8	9	10
$\theta$	4.50°	13.50°	22.50°	31.50°	40.50°	49.50°	58.50°	67.50°	76.50°	85.50°
$a/b$	3/38	6/25	12/29	19/31	41/48	48/41	31/19	70/29	504/121	216/17
$n$	38.12	25.71	31.38	36.36	63.13	63.13	36.36	75.77	518.32	216.67

### 3.2.4.2 Non-Uniform Slit Simulation

Simulation of non-uniform slits permitted testing of the proposed slit non-uniformity correction at arbitrary angle. Wedge-shaped slits were produced by subtracting two offset edges with slightly different angles. Slits of average width  $s = 12.5 \mu\text{m}$  at two representative angles ( $1.5^\circ$  and  $43.5^\circ$ ) were simulated on a  $384 \times 384$  pixel<sup>2</sup> lattice with 0.2 mm pixel pitch in the horizontal and vertical directions. Slit width varied linearly by  $\pm 6.25 \mu\text{m}$  ( $\pm 50\%$ ) over 160 pixels along the length of the slit at either angle. This type of slit-width variation was similar to that observed on the physical slit test device.

Using methods from the Appendix, the slit at  $1.5^\circ$  was produced by subtracting an edge image with parameters  $\omega = 125 \text{ mm}$ ,  $\ell = (\omega + s)/2$ , and  $\theta = 90^\circ - 1.5^\circ + \text{atan}[6.25 \mu\text{m}/(160 \times 200 \mu\text{m})]$  from another edge image with parameters  $\omega = 125 \text{ mm}$ ,  $\ell = (\omega - s)/2$ , and  $\theta = 90^\circ - 1.5^\circ - \text{atan}[6.25 \mu\text{m}/(160 \times 200 \mu\text{m})]$ . The slit at  $43.5^\circ$  was produced by subtracting an edge image with parameters  $\omega = 125 \text{ mm}$ ,  $\ell = (\omega + s)/2$ , and  $\theta = 90^\circ - 43.5^\circ + \text{atan}[6.25 \mu\text{m}/(160 \times 200 \mu\text{m})]$  from another edge image with parameters  $\omega = 125 \text{ mm}$ ,  $\ell = (\omega - s)/2$ , and  $\theta = 90^\circ - 43.5^\circ - \text{atan}[6.25 \mu\text{m}/(160 \times 200 \mu\text{m})]$ . Simulated pixel intensities in both images ranged from 10 to 16383, and Poisson random

noise was added. The presampled MTF was estimated at each angle in accordance with the procedures outlined in Slit Image Processing. Simulation results were compared for presampled MTFs produced with and without the slit non-uniformity correction.

### ***3.3 MTF Measurement Results from Experimental Implementation***

#### **3.3.1 1-D MTF Measurements**

Figure 3.4 shows the comparison of edge- and slit-based MTF measurements for the indirect-detection FPD. Averaging between the DC and cutoff frequencies,  $0.78\% \pm 0.31\%$  ( $\mu \pm \sigma$ ) difference was measured between the orthogonal MTF measurements for the slit method,  $0.31\% \pm 0.38\%$  difference was measured between the orthogonal MTF measurements for the smoothed edge method, and  $0.12\% \pm 0.40\%$  difference was measured between the orthogonal MTF measurements for the conditioned edge method. For a given MTF response, the slit-based assessment is slightly higher than the edge-based assessment from the DC-component up to about  $3.5 \text{ mm}^{-1}$ . Averaged between zero and the cutoff frequency, the slit method returns MTF values  $1.21\% \pm 0.67\%$  higher than those of the conditioned edge. These observations are consistent with other comparisons of slit- and edge-based measurements. [79, 81, 101]

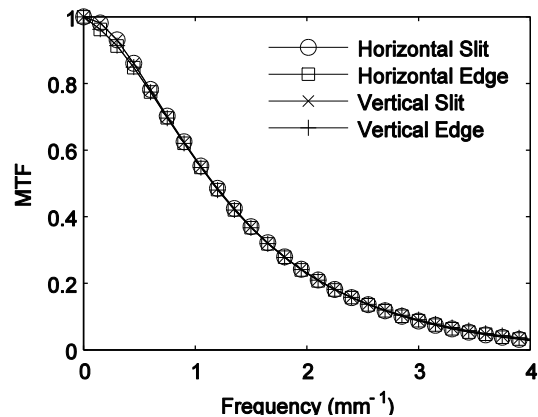


**Figure 3.4: MTF measured from (nearly) horizontal and vertical slit and edge devices.**

The edge-based MTF shown was computed using conditioned data. Symbols are plotted at every third data point.

### 3.3.2 2-D MTF Measurements

Figure 3.5(a) shows an estimate of the 2-D MTF of the GE Revolution XQ/i based on an ensemble of ten 1-D MTF measurements computed from conditioned data using a single edge-test device imaged once at each of ten angles. Based on five independent estimates of the 2-D MTF generated from five different ensembles of edge data, the relative precision error (standard deviation divided by the mean) for the non-negative frequencies only is reported in Figure 3.5(b). From Table 3.3, conditioned edge data with linear interpolation yield results with lowest average relative precision error which, averaged over  $[0, f_c]$  in the  $u$  and  $v$  directions, is 0.26%. No perceivable patterns or differences could be detected in edge-based MTF measurements as a function of measurement angle below  $4 \text{ mm}^{-1}$ . This implies approximate radial symmetry which is emphasized by the contour plot in Figure 3.5(c). Finally, in Figure 3.5(d), orthogonal profiles through the 2-D MTF are compared to the 1-D MTF obtained from slit-based measurements.

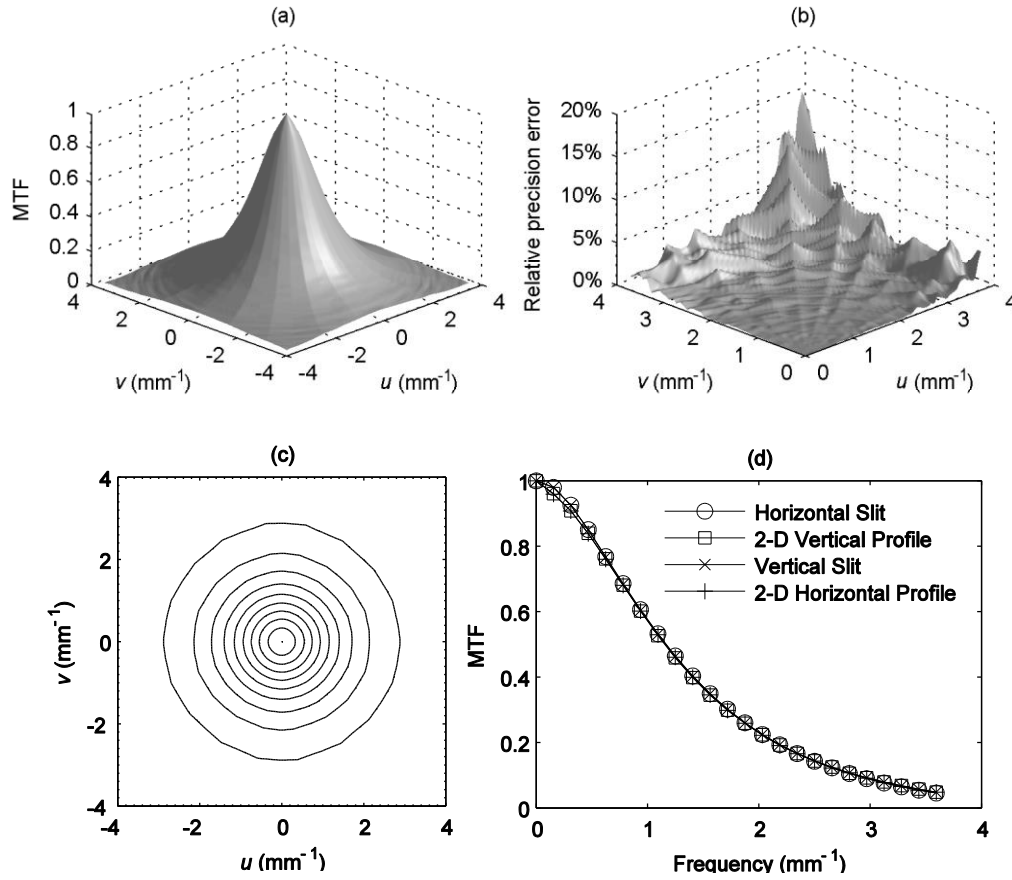


Figure 3.5: 2-D MTF estimate based on ten edge measurements between  $0^\circ$  and  $90^\circ$ .

Results using conditioned edge data are shown for  $\pm 1.5f_c$  in the  $u$  and  $v$  directions using  $192 \times 192$  linearly interpolated points. (a) 2-D rendition constructed under the assumption of reflective symmetry across the  $u$  and  $v$  axes. (b) Plot of the relative precision error for non-negative frequencies. (c) Contour plot of (a) with contours drawn at increments of 0.1 from 0.1 to 1. (d) Comparison of the MTF from approximately horizontal and vertical slits with vertical and horizontal profiles through the 2-D MTF. Symbols are plotted every fourth data point.

Table 3.3: Comparison of ESF denoising techniques and 2-D interpolation methods.

Physical measurement results are compared in terms of relative precision error averaged over  $u = v = [0, f_c]$ .

Technique	Interpolation Method		
	Nearest	Linear	Cubic
Non-denoise	0.42%	0.32%	0.37%
Smoothed	0.41%	0.32%	0.36%
Conditioned	0.34%	0.27%	0.30%



### 3.3.3 Slit-Based Measurements and Non-Uniformity Correction

Results from the slit-based measurements demonstrate features of the radial asymmetry of the 2-D MTF. Figure 3.6 shows comparisons of 1-D MTF measurements using a slit test device at  $4.15^\circ$  and  $44.07^\circ$ . At frequencies below  $4 \text{ mm}^{-1}$ , 1-D MTF plots at the two angles are nearly identical with maximum absolute difference of 0.0076. However, above  $4 \text{ mm}^{-1}$ , the first zeros of the plots differ markedly. This observation agrees with theory which, under the assumption of 100% pixel fill factor, predicts zero-values at  $5.0 \text{ mm}^{-1}$  and  $7.1 \text{ mm}^{-1}$  for the 1-D MTF measurements near  $0^\circ$  and  $45^\circ$ , respectively. And although the magnitude of the MTF for this indirect detector is quite low near the described frequencies, it clearly indicates that the approximation of circular symmetry does not apply in the high spatial frequency range. Rather, the MTF in the high-frequency range lends itself more toward the 2-D separable behavior reminiscent of the FT of the rectangular pixel aperture function, an observation consistent with expectations based on detector geometry.

Also shown in Figure 3.6 are comparisons of the 1-D MTF produced with and without slit non-uniformity correction. Whereas the corrected plots approach zero near  $2f_c$ , the uncorrected plots deviate in the positive direction. To compare corrected and uncorrected MTFs, we examine the relative difference (absolute difference divided by the average) averaged between the DC and cutoff components. At  $4.15^\circ$ , the average relative difference between corrected and uncorrected MTFs is  $0.10\% \pm 0.09\%$  with maximum absolute difference of 0.053 (near  $2f_c$ ). At  $44.07^\circ$ , the average relative difference between corrected and uncorrected MTFs is  $0.08\% \pm 0.07\%$  with maximum absolute difference of 0.022 (near  $2f_c$ ). Similar results are observed in the simulated data (Figure 3.8).

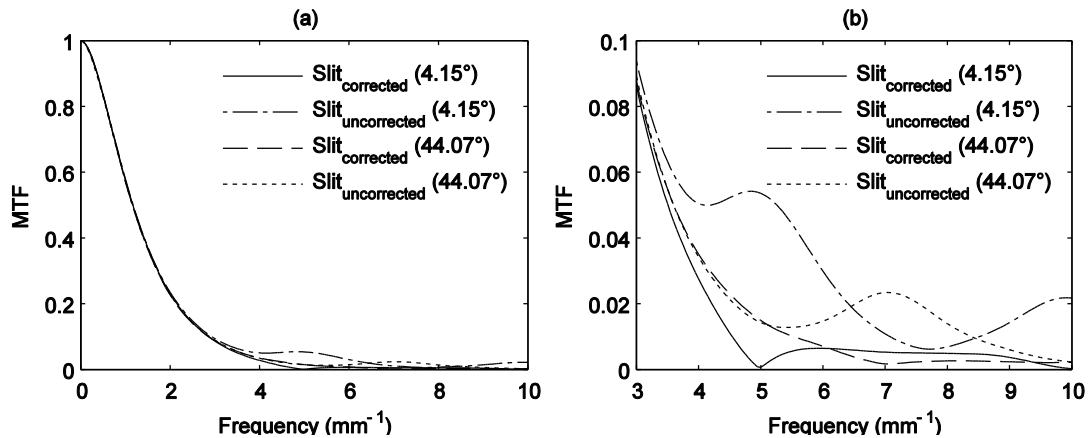


**Figure 3.6: Comparison of slit-based MTF measurements from physical slits at two angles with and without slit non-uniformity correction.**

(a) Comparison of the MTF at angles approximating 0° and 45°. (b) Detail of the MTF plot in (a) showing deviation between the MTF near 0° and 45° beyond 4 mm<sup>-1</sup>. The difference between corrected and uncorrected plots can also be appreciated.

### **3.4 Results from Validation by Synthesis**

#### **3.4.1 2-D MTF Estimation**

Figure 3.7(a) shows an estimate of the 2-D MTF of the hypothetical direct-detection FPD based on an ensemble of ten 1-D MTF measurements computed from conditioned data. Data are plotted from  $-4f_c$  to  $+4f_c$  in both the  $u$  and  $v$  directions in order to display the first side-lobes of the 2-D MTF. Figure 3.7(b) compares horizontal profiles through different estimates of the 2-D MTF based on results using different ESF denoising methods. Figure 3.7(c) shows the error associated with the plots in Figure 3.7(b), and reveals that the conditioned data yield superior results. This is confirmed numerically in Table 3.4 and Table 3.5 where different combinations of ESF denoising techniques and interpolation methods are compared. Conditioned data in combination with linear interpolation delivers the most accurate results. Conditioned data in combination with either linear or cubic interpolation delivers the most precise results.

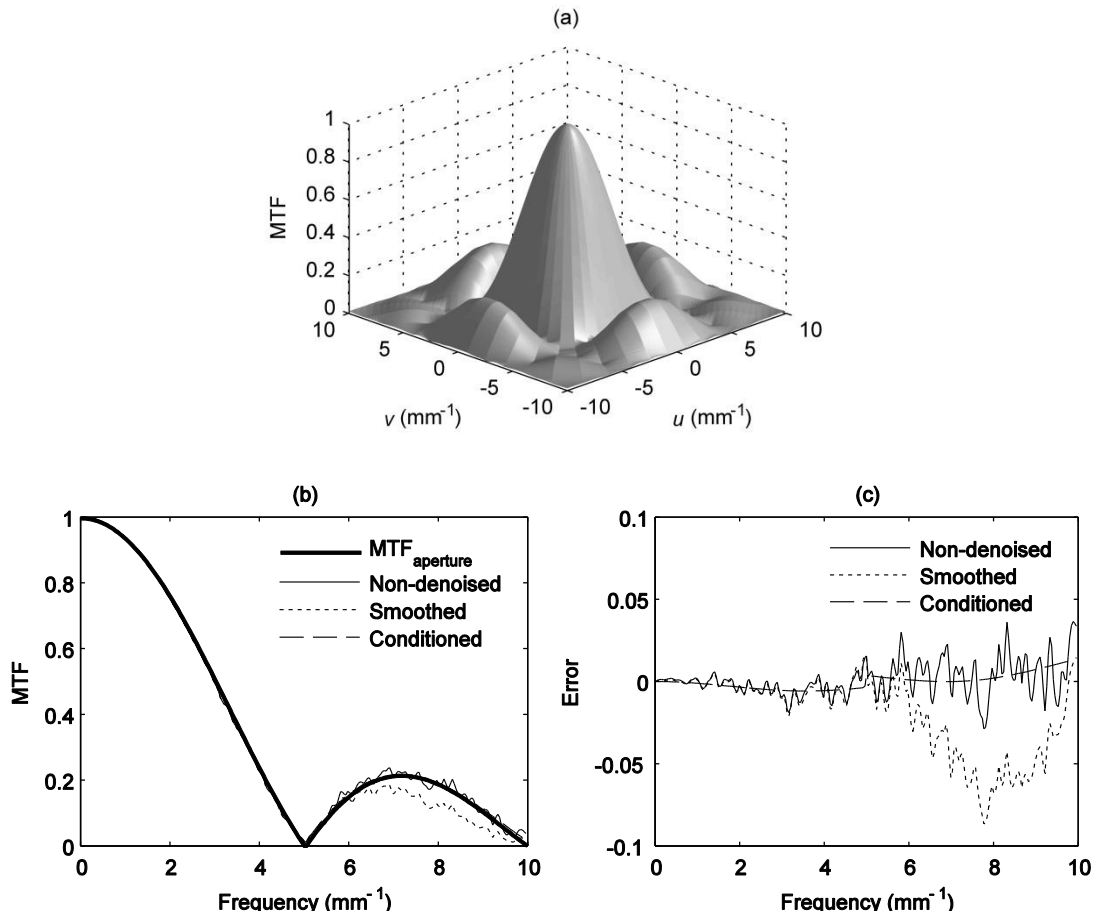


Figure 3.7: 2-D MTF measured from a hypothetical direct-detection device using the proposed edge method.

(a) The 2-D MTF was estimated from ten equally-spaced edge measurements under the assumption of reflective symmetry across the  $u$  and  $v$  axes. Linear interpolation was used to estimate MTF values on a  $512 \times 512$  pixel<sup>2</sup> Cartesian lattice in the range  $\pm 4f_c$ . (b) Using different ESF denoising methods, horizontal profiles through the 2-D MTF are compared to the true MTF. (c) Error associated with (b).

**Table 3.4: Simulation results comparing different ESF denoising techniques and 2-D interpolation methods using absolute relative accuracy averaged over  $u = v = [0, f_c]$ .**

Technique	Interpolation Method		
	Nearest	Linear	Cubic
Non-denoised	0.59%	0.35%	0.42%
Smoothed	0.57%	0.34%	0.40%
Conditioned	0.42%	0.13%	0.20%

**Table 3.5: Simulation results comparing different ESF denoising techniques and 2-D interpolation methods using relative precision error averaged over  $u = v = [0, f_c]$ .**

Technique	Interpolation Method		
	Nearest	Linear	Cubic
Non-denoised	0.51%	0.39%	0.45%
Smoothed	0.51%	0.39%	0.44%
Conditioned	0.12%	0.11%	0.11%

### 3.4.2 Slit Non-Uniformity Correction

Figure 3.8 demonstrates the relative impact of the slit non-uniformity correction on estimation of the MTF when applied to simulated non-uniform slits at  $1.5^\circ$  and  $43.5^\circ$ . Figure 3.8(a) demonstrates the improvement in MTF accuracy when the slit non-uniformity correction is applied to slit data at  $1.5^\circ$ . Figure 3.8(b) plots the associated error. Averaged between DC and  $f_c$ , the relative accuracy error of the corrected MTF is  $-0.06\% \pm 0.05\%$  while that of the uncorrected MTF is  $-0.09\% \pm 0.08\%$ . At  $1.5^\circ$ , the maximum absolute error in the corrected plot is 0.002 while that of the uncorrected plot is 0.044 (both near  $2f_c$ ). Figure 3.8(c) and Figure 3.8(d) show the same comparisons at  $43.5^\circ$ . Averaged between DC and  $f_c$ , the relative accuracy error of the corrected MTF is  $-0.19\% \pm 0.16\%$  while that of the uncorrected MTF was  $-0.27\% \pm 0.24\%$ . At  $43.5^\circ$ , the maximum absolute error in the corrected plot is 0.017 while that of the uncorrected plot is 0.031 (both near  $2f_c$ ).

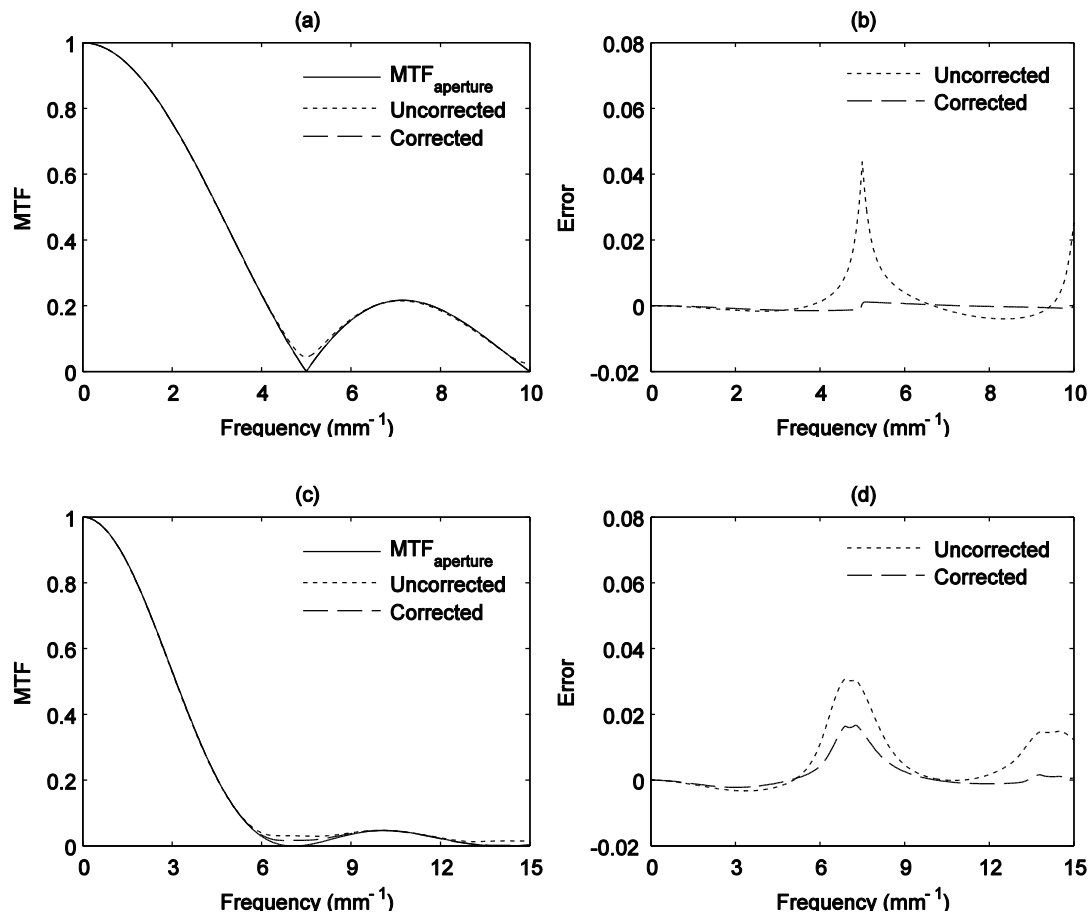


Figure 3.8: Slit-based MTF measurements using synthesized images from a hypothetical direct-detection device.

Results show the impact of slit non-uniformity correction on a non-uniform slit. (a) MTF estimates at  $1.5^\circ$ . (b) Error in MTF estimates at  $1.5^\circ$ . (c) MTF estimates at  $43.5^\circ$ . (d) Error in MTF estimates at  $43.5^\circ$ .

### 3.5 Discussion and Conclusions

Although there is appeal for the use of 2-D MTF test objects, measurement of the 2-D MTF of digital medical imaging devices has traditionally been very difficult to achieve. Point-like test objects (e.g. pinholes) have the challenges of being difficult to machine and having very little transmitted flux. For opaque pinhole test devices, proper alignment may be problematic due to the thickness of the stock material. On the contrary, non-opaque

devices may require background detrending which can affect low-frequency MTF measurements. More complicated point-like test objects (pinhole arrays) have been described in the literature to address some of these challenges, but they are still difficult to manufacture. [83, 86] Disk-test devices have also been described for use in the assessment of 2-D MTF, but reports indicate that they lack accuracy due to signal aliasing. [87-89] Recent advances have yielded promising results for extraction of the 2-D MTF from NPS data, but the precision and accuracy of these results come at the cost of intensive cascaded systems analysis and fitting of measured data to an assumed functional form of the MTF. [85]

By comparison with existing 2-D MTF test objects, namely 2-D arrays of pinholes, [83, 87] our techniques that estimate the 2-D MTF from multiple measurements with 1-D devices have certain benefits. First, 1-D test devices have been used extensively in laboratory and clinical settings, and their use is well-understood and widely accepted. Second, 1-D test devices are generally available, precluding the need for new equipment. Third, the use of an edge-test device in the estimation of 2-D MTF affords a reasonable number of measurements for high precision and practical application. And fourth, our evidence suggests that the use of multiple 1-D assessments of MTF at a wide range of angles is a robust, precise, and accurate method for 2-D interpretation of detector resolution properties. In particular, the edge method is quite tolerant of modest misalignment errors, and we have shown that it provides results similar to those derived using the slit method. [79, 81]

While the edge method for 2-D MTF estimation has several strengths, there are also some limitations to its implementation. First, the number of angles required for accurate representation of the 2-D MTF is highly dependent upon its asymmetry. If the spacing of the

radial (1-D) MTF samples is too coarse, then fine details may be lost during the 2-D interpolation process. Furthermore, if certain assumptions regarding symmetry of the MTF are not valid (e.g. reflective symmetry across the axes), then data collection at angles between  $0^\circ$  and  $90^\circ$  may need to be extended to  $180^\circ$ . Second, if the 2-D MTF at higher frequencies is to be accurately estimated, then finer radial sampling may be required to account for the reduction in radial sample density with increasing frequency. And third, it is well known that the edge method for MTF determination at very high frequencies is limited by lower SNR compared to other methods (e.g. the slit method). [101-104] If these high frequencies are of particular interest, then special care must be taken to ensure that adequate SNR is achieved.

In this work, the qualitative comparisons of the proposed edge method of 2-D MTF assessment to the results of Fetterly *et al.* [83] are noted. Fetterly *et al.* measured the 2-D MTF of the GE Revolution XQ/i using an array of pinholes. They concluded that the 2-D MTF of this indirect-detection FPD is circularly symmetric (out to  $\pm 3.75 \text{ mm}^{-1}$  in the  $u$  and  $v$  directions). Similar conclusion were drawn in this text for this same detector in the same frequency range. However, it should be recognized that the pinhole-based 2-D MTF results of Fetterly *et al.* differ from their edge-based measurements near the vertical and horizontal axes by up to 8% at frequencies between the DC and cutoff components. Fetterly *et al.* speculate that this deviation may be the result of low-frequency glare from neighboring pinholes and from detector exposure near the edges of the test device. [83] Regardless of the source, any error in MTF estimation will be amplified in calculations of the 2-D NEQ and DQE since these quantities are proportional to the square of the MTF. Analyses of the digital NEQ and DQE are limited to  $\pm f_c$  in the Cartesian coordinate plane, [102] and in this range, the proposed edge-based methods provide average relative uncertainty in the presampled

MTF of 0.26% for physically obtained data. According to the accuracy achieved in the simulation studies, it is likely that the average absolute relative accuracy error is of similar magnitude.

The high accuracy of the proposed methods has demonstrated the importance of fully 2-D MTF assessment. Whereas orthogonal 1-D measurements of MTF have traditionally been used to classify system resolution properties, accurate assessment of the 2-D MTF can provide more highly detailed measures of system performance. In particular, the MTF measurements of the indirect-detection FPD in this chapter showed differences in the observed symmetry at low- and high-frequencies. Both slit- and edge-based measurements of the GE Revolution XQ/i suggest approximate circular symmetry of the MTF at frequencies below 4 mm<sup>-1</sup>. However, at frequencies above 4 mm<sup>-1</sup>, slit-based measurements of the GE Revolution XQ/i near 45° suggest that the 2-D separable pixel aperture function dominates the behavior of the MTF. The difference in symmetry at low- and high-frequencies was only observed when using the slit method, likely due to its superior SNR at higher frequencies. [101] While the edge method exhibits higher SNR at lower frequencies, [101] it is subject to positive bias at higher frequencies due to quantum, [81] electronic, and mechanical noise. [80, 104] In addition, high-frequency noise in the ESF is amplified by differentiation (required to compute the LSF). [103, 105] Although the amplitude of the MTF at high-frequencies is quite low for most indirect-detection FPD devices, high accuracy and precision at high frequency has more profound implications when direct-detection devices are considered.

Images from a hypothetical direct-detection FPD were simulated in this work, and they served several purposes. First, the simulations provided introspection into the anticipated performance of the proposed 2-D MTF estimation methods for a detector with



appreciable MTF amplitude beyond  $2f_c$ . This can lead to appreciable aliasing in the response function, and the work in this chapter showed that the proposed methods are likely to perform well, even out to  $\pm 4f_c$  for this type of detector. Second, the simulated device permitted the computation of accuracy and precision figures given that the true 2-D MTF was known exactly (Table 3.4 and Table 3.5). And third, simulations of a non-uniform slit were conducted to investigate the impact of the non-uniformity and corresponding non-uniformity correction in terms of MTF estimation error. Results showed that slit non-uniformity has the greatest effect on the MTF near  $2f_c$  where the amplitude is quite low. At  $1.5^\circ$  and  $43.5^\circ$ , slit non-uniformity correction improved the error in MTF estimation, but some of its limitations should also be noted.

The proposed slit non-uniformity correction corrects for some, but not all, of the effects encountered in imperfect slits. The non-uniformity correction improved measurements of the MTF near  $2f_c$  for both real and simulated slits; however the correction was less impactful at lower frequencies. Furthermore, slits with variable width produce perpendicular intensity profiles which are not only variable in terms of transmitted intensity but also in terms of profile width. Although changes in the profile width are not corrected by the intensity normalization technique, such fluctuations may be of little consequence as the sinc correction used to correct for the width of very narrow slits only adjusts the amplitude of the MTF by a few percent even at high frequencies. Of perhaps greater interest would be an investigation into the effects of high-frequency fluctuations in slit width. These types of variations could introduce large errors in the finely-sampled LSF, especially in regions where the magnitude of its derivative is greatest. Such investigations are deferred to future work.

Given all of these considerations, the edge- and slit-based assessments of 2-D MTF presented here provide very favorable trade-offs between ease-of-implementation and achievable accuracy. Edge-based assessments of MTF are relatively simple and well-established, and many facilities already possess the proper equipment for this type of analysis, while slit-based methods offer better performance beyond the cutoff frequency. Results from imaging studies and simulations show that the proposed methods are not only feasible, but they may provide higher accuracy than some 2-D measurements produced using pinhole- and disk-test devices. Measuring the full 2-D MTF provides details of resolution performance not seen with traditional 1-D methods along only the vertical and horizontal axes thus providing better data for the assessment of 2-D NEQ and DQE.

## **4. Frequency Response and Distortion Properties in Nonlinear Image Processing**

As a component in the medical imaging chain, image processing may impact the resolution performance of an imaging system as a whole. It is therefore important to understand the multi-dimensional resolution properties of these algorithms due to the multi-dimensional nature of imaging and image interpretation. However, the most common metrics for resolution analysis in medical imaging (such as those reviewed in the previous chapter) are valid only for linear and approximately linear systems. While some analogues to these metrics have been used in attempts to describe resolution performance in nonlinear systems, the analysis is incomplete since nonlinear distortion effects are often ignored. Improper use of linear metrology to describe highly nonlinear systems can potentially produce misleading results. Therefore, alternative forms of analysis must be investigated.

This chapter is devoted to the formulation of a new framework for the analysis of nonlinear image processing algorithm resolution response. In particular, a means of analyzing the amplitude modulation and waveform distortion properties of nonlinear systems is developed with specific application to medical image processing algorithms. By examining an algorithm's response to any array of sinusoids at different frequencies and orientations, a complete realization of the 2-D resolution response can be assembled which separately considers the contrast modulation and nonlinear distortion effects associated with a given image processing algorithm.

The work in this chapter has been previously published in the journal *Medical Physics* and was presented at the 2013 International Society for Optics and Photonics (SPIE) Annual Meeting followed by published conference proceedings. [36, 106]

## **4.1 Current Nonlinear Resolution Assessment Strategies**

Modern medical imaging has benefited extensively from the use of nonlinear image processing algorithms. [107, 108] Nonlinear image denoising, [38, 109-111] enhancement, [112-114] and reconstruction [20, 115-117] have all been used to successfully improve image interpretability and diagnostic outcomes or to reduce patient radiation exposure and scan times. In spite of the many benefits from nonlinear processing, a complete, objective, and standardized measure of nonlinear resolution performance has not been universally accepted by investigators in the field. Such metrics are inherently difficult to develop, and attempts have generally not taken into account the confounding influence of signal distortion. Therefore, further work is necessary to better understand and characterize the resolution and distortion properties of nonlinear systems and algorithms.

To achieve objectivity in nonlinear resolution assessment, some authors have described the resolution properties of nonlinear algorithms using analogues to more familiar linear assessment strategies. In an effort to generalize the blurring properties of nonlinear CT reconstruction algorithms, Richard *et al.* [118] and Chen *et al.* [119] reported the radially averaged ESF of disk test objects. They also drew the important conclusion that nonlinear resolution performance varies with task function contrast and noise magnitude. McDonald *et al.* [120, 121] used a slanted edge to measure the small-signal modulation transfer function (MTF) of an imaging system from images with nonlinear post-processing. Both implementations of ESF measurement are useful approximations of resolution performance, but they do not decouple signal amplitude modulation from nonlinear distortion effects.

## ***4.2 Nonlinear Signal Distortion***

When a signal passes through a nonlinear device, signal power may be transferred to other frequencies, most notably to harmonics of the original frequencies; linear analysis techniques do not distinguish this effect from signal amplitude (contrast) modulation. In fact, the signal power from nonlinear waveform distortion may masquerade as contrast modulation of the input signal since linear metrics fail to quantify the effects of system nonlinearity. For example, Figure 4.1 shows how a median filter (a relatively simple nonlinear algorithm) not only modulates the amplitude of a 2-D pure sinusoidal signal, but also transfers power from the original frequency to other (non-principle) spatial frequency components. To adequately characterize this and other types of signal distortion, more complex analysis is necessary.

Volterra analysis, although not often applied to multi-dimensional signals such as images, [122, 123] is recognized as a method for nonlinear systems analysis in circuit, audio, and electrical engineering applications. [124-127] It can be used to characterize nonlinear system resolution response through the production of multiple higher-order impulse response kernels. However, a major weakness of this technique is its complexity which limits its application to weakly nonlinear systems in addition to making it impractical in regular use and interpretation.

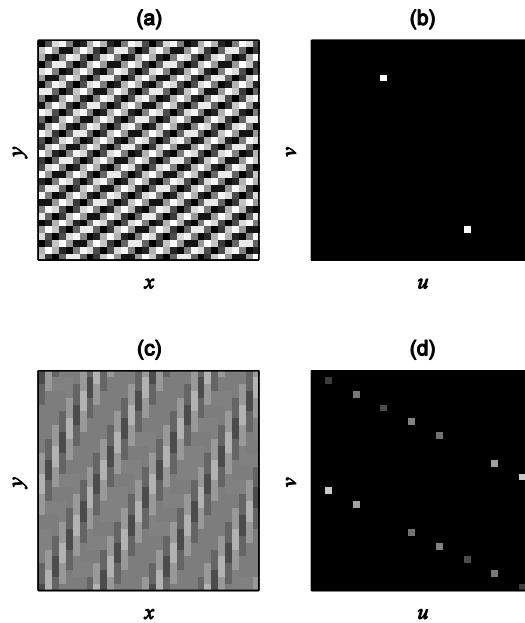


**Figure 4.1: Narrow-band demonstration of algorithm nonlinearity.**

**(a) Original 2-D sinusoid. (b) Magnitude plot of the 2-D FT of (a). (c) Spatial domain result of processing (a) with a 3x3 median filter. (d) Magnitude plot of the 2-D FT of (c) showing distribution of original signal power to harmonic frequencies constituting nonlinear signal distortion. Both the original and processed plots are equally windowed and leveled. Frequency domain plots show logged intensities.**

Alternatively, the engineering community has used total harmonic distortion (THD) as a summary measure of nonlinear waveform distortion. [128-134] In applications such as electrical power systems, circuit design, and audio engineering, THD is used to characterize the nonlinear distortion properties of electronic systems via the system response to 1-D sinusoidal waveforms of various frequencies. Compared to Volterra analysis, THD is far more compact since all higher-order nonlinear effects are summarized using a single measure. Although it is simpler than Volterra analysis, THD has not yet been applied as a nonlinear resolution analysis tool for multi-dimensional systems.

In the following sections, a generalized framework for analyzing the nonlinear resolution properties of multi-dimensional systems is derived in detail. In particular, the

work will demonstrate the use of a novel technique for simplifying the interpretation of the resolution and distortion properties of complex nonlinear systems in contexts relevant to medical imaging (such as performance in the anatomical context). The resolution characteristics of a simple median filter will be presented as an example of this approach in three relevant imaging contexts: uncorrelated background noise, correlated background noise, and an anatomical background. These results will then be compared to the performance of the bilateral filter, wavelet denoising, and CPNR with respect to measurements of contrast resolution and nonlinear signal distortion in the anatomical context. Ultimately, this chapter will demonstrate how the background context and CNR are important factors in assessing the (context-dependent) resolution and distortion properties of nonlinear algorithms.

### ***4.3 Development of Novel Nonlinear Metrology***

The following sections propose methods for separating two distinct components of nonlinear resolution response: signal amplitude modulation and nonlinear waveform distortion. Also proposed are figures of merit which characterize algorithm performance in terms of these components. These metrics are then applied to investigations of the resolution response properties of a median filter to illustrate how the metrics can be used to characterize nonlinear system resolution and distortion performance. Finally, three advanced nonlinear algorithms (bilateral filter, wavelet denoising, and CPNR) are analyzed under the new paradigm.

#### **4.3.1 Sinusoid Response**

Sinusoids are one the most commonly used basis functions in medical imaging as evidenced by the widespread use of Fourier-based analysis. It is therefore useful to

understand the potential of nonlinear image processing algorithms to distort functions of this type. Although more complex task functions are ultimately of interest (as will be discussed below) substantial information on nonlinear algorithms can be obtained from simple sinusoidal object functions. Simple sinusoids also provide a very easy means of distinguishing amplitude modulation from nonlinear distortion effects. A 2-D narrow-band sinusoidal signal can be represented as

$$s_{u_0, v_0, \varphi_0}(x, y) = A \cos[2\pi(u_0x + v_0y + \varphi_0)], \quad (4.1)$$

where the sinusoid is characterized by amplitude  $A$ , respective horizontal and vertical spatial frequencies  $u_0$  and  $v_0$ , respective horizontal and vertical sample locations  $x$  and  $y$ , and phase  $\varphi_0$ .

It is important to consider the impact of imaging context since variations in background noise magnitude, noise correlation, and anatomical variation may all affect the ability of nonlinear algorithms to resolve the signal of interest. In the case of sinusoids as a signal of interest, the spatial domain response to a signal  $s_{u_0, v_0, \varphi_0}(x, y)$  superimposed on an arbitrary background after processing with function  $f$  can be written as

$$t_{u_0, v_0, \varphi_0, b}(x, y) = f(s_{u_0, v_0, \varphi_0} + b)(x, y) - f(b)(x, y), \quad (4.2)$$

where output image  $t_{u_0, v_0, \varphi_0, b}(x, y)$  is the result of processing  $s_{u_0, v_0, \varphi_0}(x, y)$  with function  $f$  in the context of arbitrary background image  $b(x, y)$ . Subtracting  $f(b)(x, y)$  serves to isolate the sinusoid response which is the result of both principle frequency modulation and harmonic distortion.



### 4.3.2 Principle Frequency Response

If the frequency of sinusoid  $s_{u_0, v_0, \varphi_0}$  is defined as the *principle* frequency of the signal of interest, the generalized principle frequency response (PFR) of function  $f$  is defined as

$$PFR(u, v) = \lim_{M, N \rightarrow \infty} \frac{1}{MN} \sum_{m=1}^M \left| \frac{\mathcal{F}_{2D}(\sum_{n=1}^N t_{u, v, \varphi_m, b_n})(u, v)}{\mathcal{F}_{2D}(s_{u, v, \varphi_m})(u, v)} \right|. \quad (4.3)$$

Variables  $M$  and  $N$  indicate the number of samples in the ensemble averages over many phase shifts  $\varphi_m$  and many background samples  $b_n$ , respectively. These averages prevent bias in the computation of  $PFR(u, v)$  which is equivalent to the square root of the fraction of original signal power preserved at the principle frequency after processing. This is analogous to the MTF for linear systems. Figure 4.2 demonstrates that, for linear image processing techniques such a low-pass filtering, the PFR is equivalent to the MTF.

### 4.3.3 Distortion Power Spectrum

To characterize the distortion resulting from nonlinear function  $f$  operating on the sinusoidal signal in the presence of background  $b(x, y)$ , the signal power dispersed to non-principle spatial frequencies must be quantified. To do this, the distortion power spectrum (DPS) metric is defined as

$$DPS(u, v) = \lim_{N_x, N_y \rightarrow \infty} \lim_{M, N \rightarrow \infty} \frac{N_x N_y \Delta x \Delta y}{M} \times \sum_{m=1}^M \sum_{(u_i, v_j) \neq \pm(u, v)} \left| \frac{\mathcal{F}_{2D}(\sum_{n=1}^N t_{u, v, \varphi_m, b_n})(u_i, v_j)}{N} \right|^2, \quad (4.4)$$

where  $N_x$  and  $N_y$  are the ROI array dimensions used for analysis and  $\Delta x$  and  $\Delta y$  are the pixel dimensions. These multiplicative constants convert the output units to reflect signal power.  $DPS(u, v)$  is then the sum of the power at all non-principle frequency components

computed independently for each spatial frequency simulated. This is achieved using the summation  $\sum_{(u_i, v_j) \neq \pm(u, v)}$  which is a notch filter operation that ignores any changes at the principle frequency component. As a simple test of the metric, the DPS of a linear low-pass filter was computed. Figure 4.2 shows that the filter exhibits no nonlinear distortion properties as evidenced by null DPS response at all spatial frequencies.

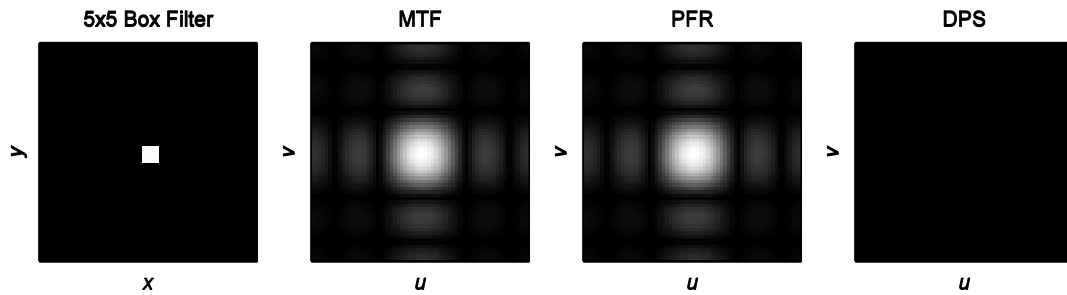


Figure 4.2: MTF, PFR, and DPS analysis of a 5x5 box filter.

The 5x5 box filter in the spatial domain can be convolved with an image to produce the filtered result. The MTF of the box filter (equal to the complex magnitude of the FT of the kernel) produces a 2-D separable sinc function. The PFR of the box filter is equivalent to the MTF.  $DPS = 0$  at all spatial frequencies indicating that the box filter imposes no nonlinear distortion on the processed image, as expected.

#### 4.3.4 Distortion Index

The PFR and DPS can be used in combination to provide a quantitative measure of algorithm performance. The PFR and DPS indicate how power in the original task object (sinusoid) gets modulated at the principle frequency (PFR) and distributed to other frequency bins (DPS) as a result of nonlinear processing. In the case of a linear processing algorithm, the PFR was shown to reduce to the MTF, and the DPS was shown to be zero at all spatial frequencies. As mentioned previously, THD is a metric used historically to describe distortion in electronic systems. The 2-D THD can be written in terms of  $PFR(u, v)$  and  $DPS(u, v)$ :

$$THD(u, v) = \frac{DPS(u, v)}{N_x N_y \Delta x \Delta y |A/2 PFR(u, v)|^2}. \quad (4.5)$$

Operations in the denominator of Eq. (5) convert  $PFR(u, v)$  to a measure of signal power since THD is the ratio of the sum of the powers of all harmonic frequencies to the power at the first harmonic or principle frequency. Although THD has traditionally been used to characterize only 1-D sinusoidal signals, its use as a 2-D figure of merit is seen to be straightforward, and generalization to higher-dimensional analysis is trivial. As a figure of merit, THD is a fine method for quantifying nonlinear signal distortion as a fraction of the power at the principle frequency, but  $THD(u, v)$  approaches infinity at  $PFR(u, v) \approx 0$ . With only slight modification, this problem is avoided by defining the distortion index (DI):

$$DI(u, v) = \frac{DPS(u, v)}{N_x N_y \Delta x \Delta y |A/2 PFR(u, v)|^2 + DPS(u, v)}. \quad (4.6)$$

$DI(u, v)$  restricts the measure of harmonic distortion to a range of [0,1] by computing the total output signal power in the denominator. Therefore,  $DI(u, v)$  is the fraction of nonlinear distortion power to total output signal power.  $DI(u, v) = 0$  indicates no nonlinear waveform distortion at frequency  $(u, v)$ , and  $DI(u, v) = 1$  indicates that 100% of the signal at frequency  $(u, v)$  can be attributed to nonlinear waveform distortion.

### 4.3.5 Summed (Integrated) Distortion Index

A scalar measure of DI can be formulated to summarize algorithm distortion properties over all frequencies of the original sinusoidal task object:

$$\Sigma DI = \frac{\Sigma \Sigma DPS(u, v)}{\Sigma \Sigma [N_x N_y \Delta x \Delta y |A/2 PFR(u, v)|^2 + DPS(u, v)]}. \quad (4.7)$$

$\Sigma DI$  measures the fraction of total output signal power attributed to nonlinear waveform distortion. Like  $DI$ ,  $\Sigma DI$  is bound to the range [0,1] which facilitates inter- and intra-algorithm comparisons of nonlinear distortion performance.

#### **4.4 Experimental Evaluation**

The median filter was chosen to initially demonstrate the utility of the proposed metrics. It is a nonlinear image processing algorithm which has been used extensively in medical imaging as a noise-reducing image filter.[135-138] It was chosen due to its relative simplicity, small parameter-space, and prevalence in medical image processing. Although several novel adaptations of the algorithm exist, this study will explore the most basic version of the algorithm for demonstration purposes. Observations will be made about the characteristics of the algorithm based on  $PFR(u, v)$ ,  $DPS(u, v)$ ,  $DI(u, v)$ , and  $\Sigma DI$  metrics, and strategies for comparing the resolution performance of different algorithms based on these metrics will also be considered.

The algorithm was analyzed in a  $256 \times 256$  pixel<sup>2</sup> region with backgrounds representing three different imaging contexts as shown in Figure 4.3: a flat field with a background of uncorrelated noise, a flat field with a background of white noise correlated using a Gaussian filter ( $\sigma = 1$ ), and an ROI taken from the lung region of an anthropomorphic phantom (Lungman, Kyoto Kakagu, Kyoto, Japan) acquired at one-third of typical clinical exposure using an indirect-detection FPD (Revolution XQ/i, GE Healthcare, Waukesha, WI). These backgrounds were chosen to investigate the effects of increasing levels of correlation on nonlinear algorithm task performance. Sinusoidal task objects were simulated within a  $16 \times 16$  pixel<sup>2</sup> ROI and superimposed at 64 different locations throughout each of the three images. Sinusoids  $s_{u_0, v_0, \phi_0}(x, y)$  were independently simulated at all

discrete spatial frequency combinations  $(u_0, v_0)$  and 16 random phase shifts in order to calculate the PFR and DPS values at each respective spatial frequency.

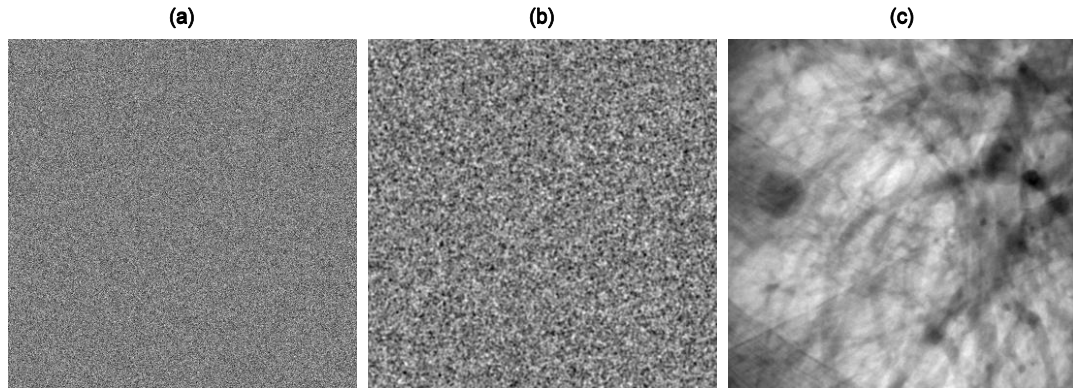


**Figure 4.3: Image backgrounds for nonlinear algorithm resolution analysis.**

**(a) Simulated white (uncorrelated) noise. (b) Gaussian-correlated white noise. (c) Lung ROI from an anthropomorphic phantom image acquired with an indirect-detection FPD. Pixel intensities in all three raw images are proportional to exposure and contain no additional processing.**

Sinusoidal task objects at several different CNR levels were investigated to ascertain potential changes in nonlinear algorithm performance. The amplitudes  $A$  of all simulated sinusoids were adjusted such that the target CNR was achieved (noise in this sense refers to the standard deviation of the stochastic component of the noise).  $PFR(u, v)$ ,  $DR(u, v)$ , and  $DI(u, v)$  were computed at  $CNR = \{0.5, 1.0, 2.0, 5.0, \infty\}$  for each background image in Figure 4.3.  $\Sigma DI$  was computed at various CNR levels in the domain  $[0.1, 5]$  for each background image.

#### **4.4.1 PFR**

PFR analysis revealed changes in the response pattern as a function of CNR and background image. Figure 4.4 shows that the median filter response function has a sinc-like shape at low CNR, and the mid- and high-frequency PFR improves with increasing CNR. At fixed CNR, the median filter response function values tend to increase as the background

changes from white to correlated noise and from correlated noise to anatomical background.

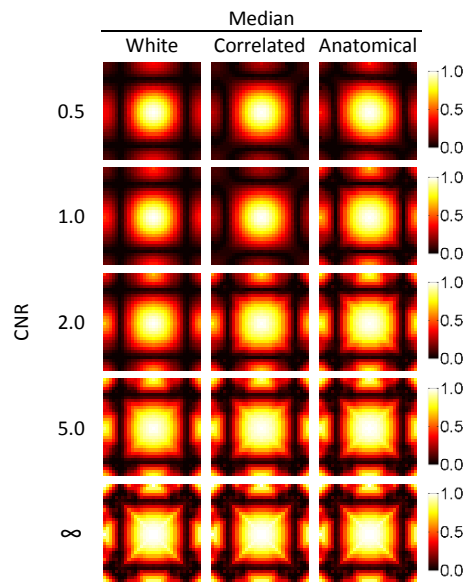


**Figure 4.4: PFR is shown at several combinations of CNR and image background.**

**The median filter exhibits a PFR with shape that changes as function of both CNR and background. All images are equally scaled. Image intensity is unitless.**

#### **4.4.2 DPS**

DPS measurements are shown in Figure 4.5. The DPS response functions exhibit trends similar to those observed in the PFR. Nonlinear distortion in the median filter response increases with increasing CNR. Median filter distortion also increases with increasing correlation of the background image signal.

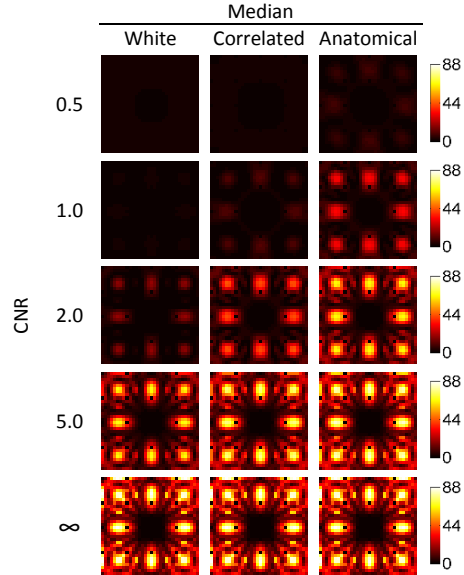
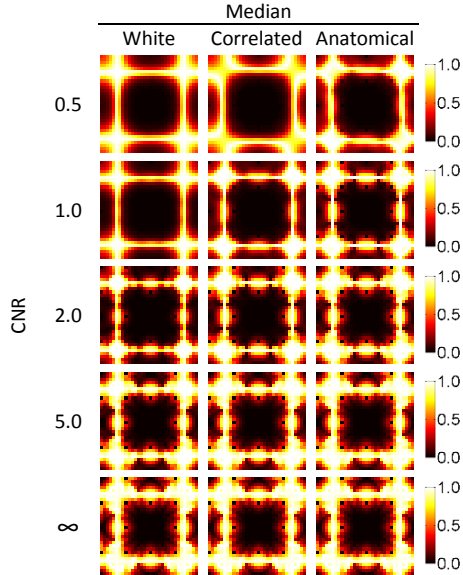


Figure 4.5: DPS of the median filter.

Low DPS is indicative of low levels of nonlinear distortion. For the median filter, DPS increases for objects with increasing CNR and for objects processed on background with increasing amounts of signal correlation. All images are equally scaled with units of  $\text{pixel value}^2 \times \text{pixel area}$ .

#### 4.4.3 DI

$DI(u, v)$ , the fraction of output signal power attributed to nonlinear distortion as a function of spatial frequency, is shown in Figure 4.6. The median filter response shows extensive nonlinear distortion at mid- and high-frequencies. Changes in  $DI(u, v)$  diminish beyond  $\text{CNR} = 5$  for the median filters.



**Figure 4.6: DI varies as a function of CNR and image background.**

**DI(u,v) is highest at frequencies with low PFR(u,v) indicating that most or all of the output signal at those frequencies is attributed to nonlinear signal distortion. All images are equally scaled. Image intensity is unitless.**

#### **4.4.4 $\Sigma DI$**

The plots in Figure 4.7 show  $\Sigma DI(CNR)$ , a summary measure of nonlinear waveform distortion and its impact on waveform fidelity as a function of CNR.  $\Sigma DI$  is a useful measure of algorithm performance which can be used to summarize the range of object contrast levels over which an algorithm exhibits strongly nonlinear characteristics. Each curve corresponding to the median filter contains a local minimum where nonlinear waveform distortion is minimized as a function of CNR in each imaging environment:  $\Sigma DI_{\min} = 0.0499$  at  $CNR = 1.2$  for white noise,  $\Sigma DI_{\min} = 0.0610$  at  $CNR = 0.7$  for Gaussian-correlated noise, and  $\Sigma DI_{\min} = 0.0674$  at  $CNR = 0.3$  for the anatomical background. Beyond  $CNR = 5$ , the median filter curves asymptotically approach an upper bound of  $\Sigma DI = 0.3017$  in the limit as CNR goes to infinity.



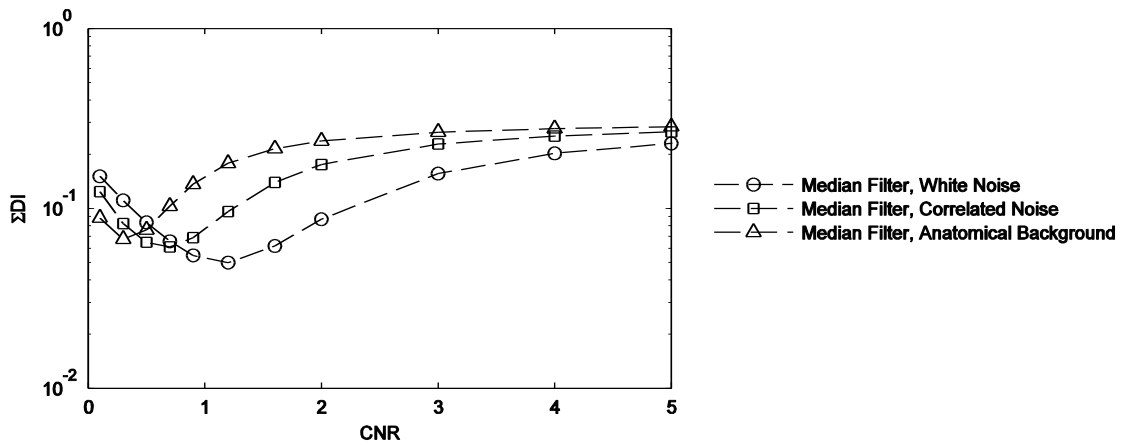


Figure 4.7:  $\Sigma DI$  plotted as a function of CNR for various background images.

$\Sigma DI(CNR)$  indicates the fraction of total output signal power attributed to nonlinear waveform distortion averaged over all spatial frequencies. For the median filter, this changes as a function of both CNR and background image. Local minima in the plots indicate object CNR for which nonlinear distortion is minimized.

#### 4.5 Application of Nonlinear Metrology to the Bilateral, Wavelet, and CPNR Filters

Using the newly developed metrology in this chapter, the nonlinear denoising algorithms from Chapter 2 can be analyzed. For the sake of brevity, only the anatomical background was investigated since this scenario most closely represents the target denoising application. PFR results are provided in Figure 4.8. They show that the bilateral, wavelet, and CPNR algorithms all perform reasonably well at preserving the contrast of sinusoidal test signals at most frequencies for the CNR levels investigated. The bilateral and wavelet filters very nicely preserve the contrast resolution of high CNR structures but resulted in some blurring of high frequency low CNR details. Comparing the PFR results to the images in Figure 2.29, this effect can be observed through the blurring of the low contrast, high frequency trabecular structures in the rib. By comparison, the mid and high frequency performance of CPNR is quite good even for low CNR structures. This is evidenced by the improved preservation of trabecular detail by the CPNR technique. The

low-frequency CPNR optimization ( $\text{CPNR}_{\text{LOW}}$ ) does show some contrast suppression of high frequency structure. But the reader is reminded that only the lowest frequency information from the  $\text{CPNR}_{\text{LOW}}$  results was retained in frequency blending (Figure 2.24). The improved mid and high frequency performance of the  $\text{CPNR}_{\text{MID}}$  and  $\text{CPNR}_{\text{HIGH}}$  optimizations was retained in both  $\text{CPNR}_{\text{BLEND-2}}$  and  $\text{CPNR}_{\text{BLEND-3}}$  frequency blended images.

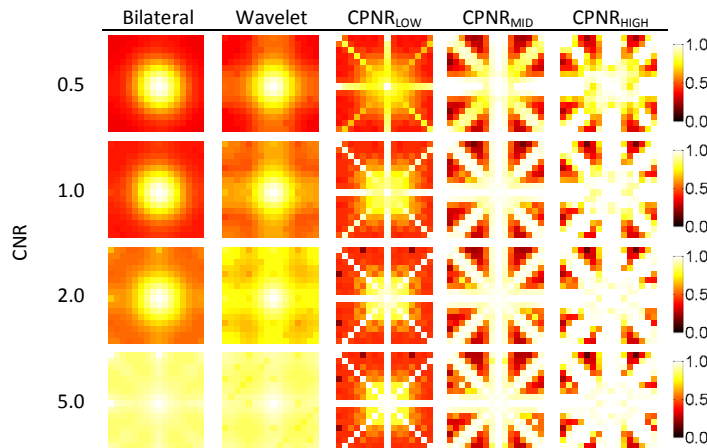


**Figure 4.8: PFR characterization of bilateral, wavelet, and CPNR algorithms.**

**PFR analysis reveals that the bilateral and wavelet filters very nicely preserve the resolution of high CNR details with some blurring of low CNR high frequency details. At low frequencies,  $\text{CPNR}_{\text{LOW}}$  shows similar resolution properties as the bilateral and wavelet filters, but  $\text{CPNR}_{\text{MID}}$  and  $\text{CPNR}_{\text{HIGH}}$  show improved mid- and high-frequency resolution properties for lower CNR task objects. Only results corresponding to the anatomical test background are shown here.**

DPS analysis provided very promising results for the nonlinear algorithms investigated. Figure 4.9 shows that CPNR processing results in very little nonlinear signal distortion. According to the figures, the bilateral, wavelet, and  $\text{CPNR}_{\text{LOW}}$  algorithms produced some distortion in high CNR sinusoidal test signals. However, it is not so much the net amount of signal distortion that is important. The relative amount of signal distortion as a fraction of the total output signal power provides a more informative measure of algorithm nonlinearity. This quantity is measured by DI

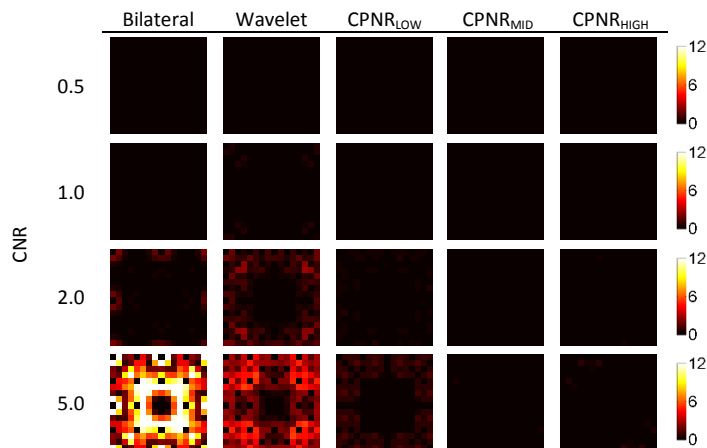


**Figure 4.9: DPS characterization of bilateral, wavelet, and CPNR algorithms.**

**Nonlinear distortion (DPS) analysis shows some signal distortion of high CNR sinusoids for the bilateral, wavelet, and CPNR<sub>LOW</sub> denoising algorithms. Otherwise, the denoising paradigms show negligible nonlinear distortion of the sinusoidal test signals. Only results corresponding to the anatomical test background are shown here.**

DI measures are provided in Figure 4.10. According to the results, nonlinear distortion of the input signal comprised a miniscule fraction of the output signal power for all algorithms investigated. This means that the sinusoidal test signals of various amplitudes overlaid on the anatomical background experienced little to no distortion in the shape after nonlinear processing. Although PFR analysis showed that the contrast of these sinusoidal test signals was somewhat diminished at mid and high frequencies, the sinusoidal shape of the signal was preserved.

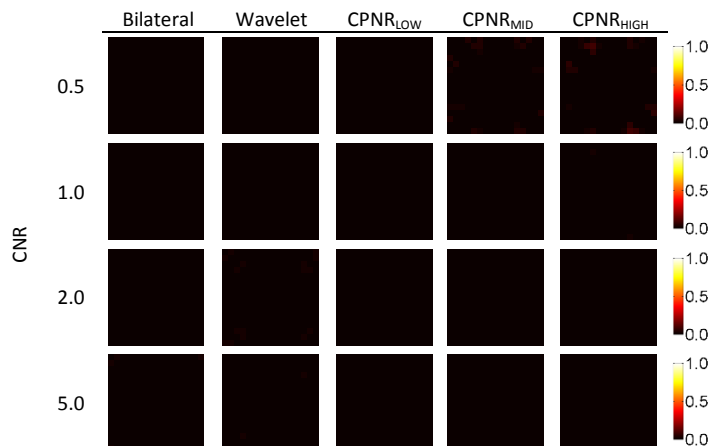


**Figure 4.10: DI characterization of bilateral, wavelet, and CPNR algorithms.**

**Nonlinear signal distortion constitutes a negligible fraction of the total signal output for all algorithms at the CNR levels observed. Only results corresponding to the anatomical test background are shown here.**

$\Sigma DI$  analysis returned the same result as depicted in Figure 4.10: none of the advanced nonlinear algorithms investigated resulted in substantial nonlinear signal distortion. As a fraction of the total signal output, the effects of nonlinear signal distortion were practically unobservable. Therefore, it may be concluded that, in the anatomical context, these algorithms behave in an approximately linear fashion with respect to the resolution response to sinusoidal signals at the CNR levels investigated. Of course, these conclusions may only be valid for sinusoid-like signals. Further testing with other basis objects may reveal more widely interpretable results. Ultimately, this is an important finding which indicates that nonlinear processing with these algorithms does not impart “new” information into the image through nonlinear distortion of the original image signal.

#### ***4.6 Discussion, Benefits, and Limitations***

Nonlinear image processing is a dynamic and expanding area of research in medical imaging. As this area of research continues to grow, critical and thorough algorithm

assessment strategies must be standardized and implemented to ensure high image quality. This work describes the use of several new measures for nonlinear algorithm resolution performance analysis:  $PFR(u, v)$ ,  $DPS(u, v)$ ,  $DI(u, v)$ , and  $\Sigma DI$ . These measures were used to show that signal power may not only be modulated for a given spatial frequency component, but that signal power may also be redistributed to other spatial frequencies as a result of nonlinear processing.

To visualize the effects of principle frequency contrast modulation and nonlinear distortion, an example has been provided in Figure 4.11. The corresponding PFR and DI values have been provided in the figure to demonstrate how these normalized metrics may be used to quantify and compare the contrast response at the principle frequency and the relative impact of nonlinear waveform distortion for sinusoids with different frequencies and orientations. This type of analysis and its conclusions are supported by the widespread use of a similar figure of merit (THD) used to characterize nonlinear system effects on 1-D signals in several engineering applications. As a result, this work has demonstrated for the first time the use of distortion analysis for quantifying nonlinearity in multi-dimensional imaging systems.

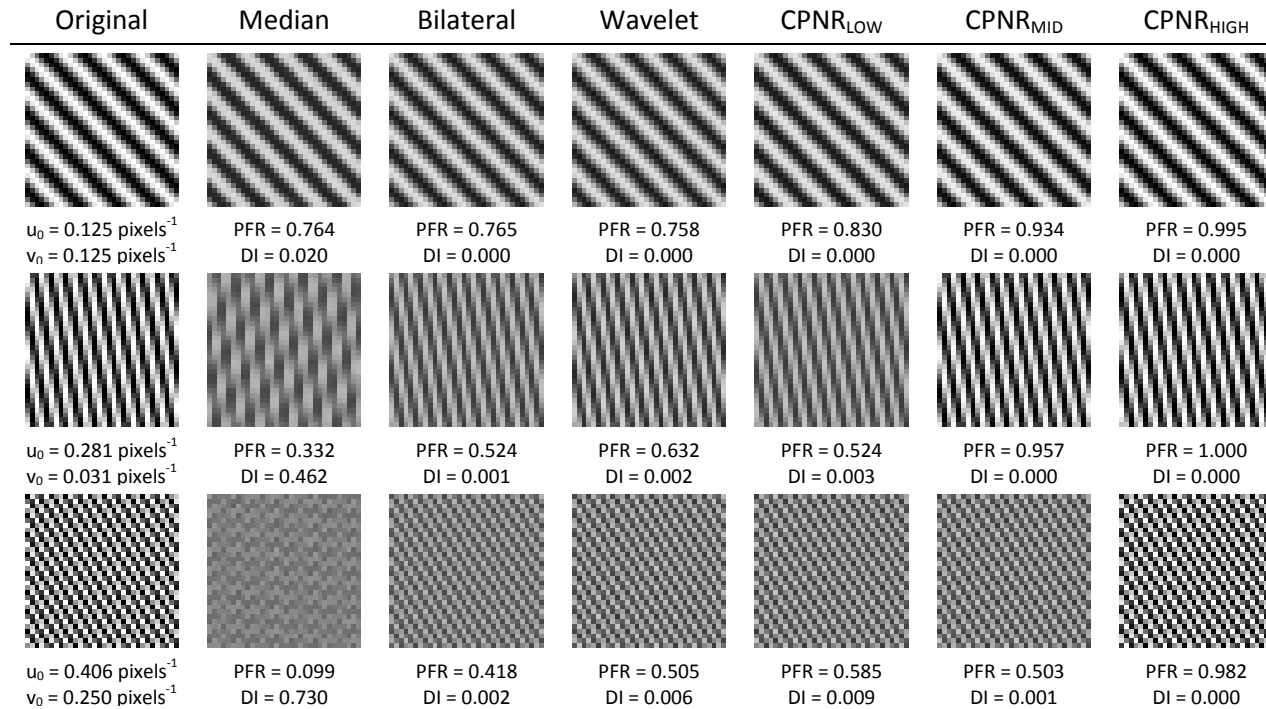


**Figure 4.11: Visualization of principle frequency contrast modulation and nonlinear distortion effects.**

The three sample sinusoids at various frequencies and orientations demonstrate how PFR and DI can be used to describe the algorithm response to sinusoidal signals. The contrast modulation of the sinusoid is described by the PFR value. DI values indicate the fraction of output signal power attributed to distortion. The median filter results demonstrate how a single algorithm can exhibit very little to severe nonlinear distortion of the input signal. By contrast, the other algorithms have quite minimal and stable distortion response at all frequencies. Algorithms differ somewhat in their ability to preserve the amplitude (contrast) of the sinusoidal test signal. CPNR is quite exceptional in this regard. All images are equally scaled.

Quantitative assessment of algorithm nonlinearity has shown that it manifests differently for algorithms employing different nonlinear mechanisms. Several nonlinear denoising algorithms demonstrated very different contrast response patterns. Figure 4.4 and Figure 4.8 showed differences in the shape in  $PFR(u, v)$  as both a function of signal CNR and image context. Comparisons between Figure 4.5 and Figure 4.9 revealed large scale differences between  $DPS(u, v)$  measured for a simple median filter and other more advanced nonlinear denoising filters. The distortion properties of the nonlinear algorithms were also shown to vary over different CNR levels and image contexts. These observations support the conclusions of other authors who showed that nonlinear resolution properties of imaging systems vary with noise magnitude and contrast, [118, 119] but this work reveals that nonlinear resolution is also impacted by noise correlation and image background. This suggests that measurements of nonlinear resolution performance made with test objects against flat backgrounds (as is the current practice for most medical imaging systems) [139, 140] do not necessarily equate to the resolution performance in natural settings. This key finding implies that the most accurate results are achieved when quantitative algorithm performance assessment takes place within an imaging context that closely resembles the natural application.

Quantification of image processing algorithm nonlinearity is an important result of this work with several other implications. It provides two new measures of nonlinear algorithm resolution performance — one which quantifies the impact of desirable algorithm qualities (PFR) and another which quantifies undesirable algorithm qualities (DPS). The separation of these characteristics creates new possibilities for algorithm parameter space optimization. For instance, the optimization of a denoising algorithm should seek to minimize the NPS in addition to DPS minimization while maximizing the PFR. Perhaps most

importantly, the quantification of algorithm nonlinearity can be used to define scenarios where algorithm nonlinearity is more or less negligible. Approximate system linearity is assumed by mathematical models such as those used in human observer performance analysis, and the techniques proposed in this paper can validate the range of algorithm operation over which this assumption is valid. Actual human observer studies will be necessary in future studies to show how the proposed metrics correlate with the effects of algorithm nonlinearity and waveform distortion on observer performance in different imaging tasks.

So far, sinusoidal task functions have been the only waveform analyzed using the proposed techniques. The use of sinusoids in this work was beneficial in that it permitted easy distinction of signal amplitude modulation from nonlinear waveform distortion. The sinusoid serves as the basis object of choice for most medical image processing since it is especially useful for identifying the effects of object scale space, orientation, and periodicity. Since distortion measures are derived from explicit sinusoid analysis, they can be used to exactly describe the resolution response of nonlinear systems to sinusoidal inputs. These same response functions might also be used to describe the nonlinear resolution response properties of other periodic signals such as textures. [141-143] It has been acknowledged that nonlinear image processing affects the appearance of topological texture features in medical images, [20] and this has been shown to affect image perception. This can be problematic if diagnosis and disease monitoring depend heavily on texture-based analysis (e.g. interstitial lung disease). [144, 145] Harmonic distortion analysis could therefore be a useful technique for quantifying image texture distortion so that the fidelity of important image textures can be preserved through nonlinear processing.



Although sinusoids are pervasive in the analysis of medical imaging systems, interpretation of the results gleaned from their explicit analysis may be somewhat limited. In general, for nonlinear systems, it should not be assumed that the sinusoid response function values are equivalent to those of other imaging tasks. Unlike many task objects common to medical imaging, sinusoids lack distinct edges. Imaging tasks such as disks, fibers, and punctate objects contain substantial edge content which is likely to produce task-specific differences in the resolution and distortion response functions. This is especially true of edge-preserving noise reduction filters such as the median filter and bilateral filter. Furthermore, the periodic nature of sinusoids can affect the manner in which they are processed. For instance, although 2-D sinusoids emulate the appearance of linear structures, the periodicity of sinusoids differentiates them from real linear structures like fibers and vasculature. This can result in processing differences, especially at high frequencies. Unfortunately, the absence of a basis function with sufficient likeness to most natural objects makes it difficult to assess their distortion properties: the signal amplitude modulation and nonlinear waveform distortion functions cannot be separately analyzed for objects which do not explicitly serve as basis functions. Future work should investigate methods to extend the analysis metrics presented here to other more complex task functions in addition to generalization of nonlinear distortion analysis for higher-dimensional modalities such as CT and magnetic resonance imaging.

#### ***4.7 Conclusions and Future Directions***

Nonlinear systems analysis is complicated, and this presents challenges in the use of traditional image quality metrics. This work has proposed several metrics which simplify and generalize the quantitative assessment of nonlinear system resolution performance.

Through the analysis of sinusoidal basis objects, the proposed metrics separately consider two distinct components of the nonlinear resolution response: amplitude modulation and nonlinear waveform distortion. Analysis of several image denoising algorithms using the proposed methods in the context of medical imaging revealed patterns and trends in the response functions specific to the algorithms investigated. Image context, test pattern CNR, and nonlinear mechanism were all shown to impact the shape and magnitude of the resolution and distortion response functions.

In the future, it may be beneficial to investigate test signals other than sinusoids. Namely, the wavelet basis set may offer a useful means of signal decomposition for investigating nonlinear resolution response. The localization of wavelets in both time/space and frequency make them well suited for image analysis. And because of their spatial localization, wavelets may provide better introspection into nonlinear algorithm response to structured, finite objects such as lesions. By processing wavelet objects in the spatial domain, the wavelet transform can be used to investigate changes in the spatial frequency content of those wavelets making them amenable to distortion analysis in much the same way as sinusoidal signals. While sinusoids may provide some indication of nonlinear response to textures and extensive patterning in images, wavelets may provide more information about other diagnostically relevant signals including punctate objects, masses, and other localized structures.

In conclusion, nonlinear processing may fundamentally change the information content of medical images through the modulation of signal power at non-principle frequency components. Furthermore, just as object contrast, noise magnitude, noise correlation, and background anatomical signal affect human observer performance,[146-148] nonlinear algorithm resolution performance is likewise affected. This implies that the

nonlinear resolution and distortion properties specific to particular imaging tasks are most accurately measured in the context in which they naturally appear. Therefore, the first- and higher-order resolution effects of medical image processing algorithms should be routinely assessed in a task-specific manner against natural (anatomical) backgrounds within CNR ranges expected in clinical practice, especially as nonlinear processes become more pervasive in medical imaging. The metrics described in this chapter provide a promising avenue for assessing the resolution and distortion effects of nonlinear algorithms.

## 5. CPNR Application to Computed Tomography

It was stated in the first chapter that CT is the single largest contributor of medical imaging radiation dose to the US population as a whole. [3] Radiological CT procedures number over 67 million per year, and multi-detector CT (MDCT) is capable of delivering some of the highest clinical radiation exposures per examination. [1, 4] Some routine radiological CT procedures exceed 15 mSv per study. [2] In terms of the lifetime risk of radiogenic cancer induction associated with a single high-dose CT examination, chances range from 1 in 14,680 (60 year-old male undergoing routine head CT study) up to 1 in 150 (20 year-old woman undergoing coronary CT angiography) with all manner of risk in between. [149] Much higher risks have been estimated in children [150] where up to a ten-fold increase in lifetime cancer mortality from CT can be expected for pediatric patients compared to adults.

Although the added lifetime cancer risk to the individual receiving a single high dose CT examination is in general minimal, the accumulated risk to the population cannot be ignored. According to the US National Cancer Institute's Surveillance Epidemiology and End Results (SEER) Database, the average US male has a lifetime risk of 43.92% and the average US female has lifetime risk of 38.00% for the development of cancer (all invasive sites included). [151] However, certain vulnerable subsets of the population are at higher risk for medically-induced radiogenic cancers (e.g. children and patients receiving multiple scans), and these patients may especially benefit from radiation dose reduction in medical imaging procedures.

In this chapter, CT is identified as a primary target for dose reduction through algorithmic post-processing of lower dose procedures. Two CT applications will be

considered for preliminary CPNR testing: radiographic MDCT and radiotherapy on-board patient positioning cone-beam CT (CBCT). The radiation risks associated with MDCT use have been outlined above. Radiation therapy patients, on the other hand, represent a special subset of the population of people who are the recipients of CT studies. Patients undergoing radiation therapy treatment regimens may receive as many as 42 CBCT examinations at an effective dose of 10-24 mSv per scan. [152] Although highly beneficial, the dose levels associated with daily CBCT for patient positioning have been associated with an estimated 2-4% increase in secondary cancer risk on top of that already assumed through healthy tissue exposure to the treatment beam. Therefore, algorithmic denoising is of potential interest in both CT settings.

To test the efficacy of CPNR in CT, this chapter opens with an XCAT simulation study of the initial investigation of CPNR application to MDCT. The geometry of a clinical MDCT device is used to simulate projection data similar to that obtained through standard radiological chest and abdomen studies. Projection data are denoised with CPNR and reconstructed using a filtered back-projection (FBP) algorithm. [153] NPS measurements from reconstructed data will show the extent of noise reduction achievable by CPNR. A second investigation will study the impact of CPNR denoising on clinically acquired CBCT data from a radiation therapy treatment device. Scans of a quality assurance phantom at different exposure levels will provide data used to measure the NPS and resolution effects of CPNR application in CBCT projection space.

Some of the preliminary results in this chapter were previously presented at the 2013 International Society for Optics and Photonics (SPIE) Annual Meeting followed by published conference proceedings. [154] A second proceedings paper for the same conference is currently in preparation for the 2014 meeting.

## ***5.1 Preliminary Simulation Studies of CPNR Applied to MDCT***

To explore the potential for CT dose reduction with CPNR, XCAT simulation studies were designed to emulate clinical MDCT examinations of the chest and abdomen. Although advanced CT scanner simulation software has recently become available (CATSIM, GE Healthcare, Waukesha, WI), that software was not accessible at the time these simulation were conducted. Instead, this work used dedicated XCAT simulation software and in-house reconstruction algorithms.

### **5.1.1 MDCT and XCAT Simulation**

MDCT projection images were simulated using the XCAT phantom and XCAT CT projector. [48, 50] Scanner geometry was based on that of the GE Discovery 750 HD CT scanner (GE Healthcare, Waukesha, WI). The image quality characteristics of this scanner are described in the literature. [155] The third generation curved detector array contained 64 rows and 888 columns with integrating detection elements of size 1.0915 mm × 1.0239 mm in the row and column directions, respectively. Detector elements had a geometric fill factor of 0.8 in both directions. The source-to-image distance was 947 mm, and the source-to-axis distance was 539 mm. In a slight departure from the typical scan protocol, axial scans were simulated as opposed to the more common helical scan geometry due to the current limitations of the XCAT CT projector. 984 views per 360° rotation provided the complete set of CT projections.

Projection image intensity was directly proportional to exposure, and each projection was simulated with the same average exposure, hence an mA modulation scheme was not implemented. To produce images with noise levels matching the clinical protocols and applications, clinical noise levels from thoracic and abdominal CT studies were

obtained from consultation with a clinical medical physicist. Based on the physicist's experience with FBP reconstructed data under standard reconstruction conditions (standard apodization and 5 mm reconstructed slice thickness), noise standard deviation measurements in normal-sized patients average 13-14 HU in the heart region and 15-20 HU in the liver region. A 120 kV<sub>p</sub> spectrum was simulated and the beam intensity was adjusted to provide identical noise levels in the reconstructed XCAT data. A bowtie filter was not simulated, and no scattered radiation was included. Projection datasets were generated for lung and abdomen studies at normal and half dose.

### **5.1.2 CPNR Optimization in MDCT Projection Space**

In CT imaging, denoising can be performed either in the projection image space, the CT reconstruction space, or both. Other authors have previously reported on their experiences comparing denoising algorithm applications in these two spaces. In particular, Xia *et al.* [38, 156] reported that denoising of dedicated breast CT data was most successful when applied in the CT projection space. Compared to denoising in the CT reconstruction space, projection space denoising achieved better noise magnitude reduction with better residual noise texture while also preserving the resolution of anatomical structures. Furthermore, projection space denoising avoided the confounding effects of reconstruction artifacts (such as streak and beam hardening artifacts) which can remain after denoising due to their highly structured appearance. Overall, up to 60% dose reduction was reported using Xia's partial (anisotropic) diffusion equation-based techniques.

Still other authors have pursued CT projection space denoising from the perspective of sinogram denoising. [27, 39, 157-162] By incorporating information from the angular acquisition dimension, image denoising can be further improved by exploiting redundancies

in the anatomical detail which only slowly changes through the angular dimension. Nonlinear denoising paradigms can be used to exploit this redundancy leading to better suppression of the random noise component while preserving the desired anatomical information. To successfully perform sinogram denoising, a 3-D version of the CPNR algorithm will need to be developed as part of future work. Therefore, the investigation in this chapter will focus exclusively on the 2-D projection space image denoising paradigm.

According to work done in a previous publication, [154] the CPNR settings needed to be re-optimized for denoising the larger (1.0915 mm × 1.0239 mm) pixels used in MDCT simulation. Use of the optimized settings from Chapter 2 for radiographic image denoising resulted in some blurring of anatomical structures when used to denoise the larger pixels in the MDCT projection data, and this was to be avoided. CPNR settings were re-optimized for larger pixels using the techniques outlined in section 2.2 Polarity Estimation, and it was determined that optimum performance could be achieved using  $(p, \ell, t_{EST}, t_W, t_{MAJ}) = (4, 9, 0, 0.75, 0.6)$ . The CPNR algorithm was run for four iterations to achieve total noise variance reduction of 41% in the projection space data with minimal degradation of the anatomical information.

### 5.1.3 FBP Reconstruction from Cylindrical Detector Data

Simulated projection data were reconstructed using the filtered back-projection algorithm of Feldkamp, David, and Kress with geometric adaptations for a cylindrical detector. [153, 163-165] Projection data were first preprocessed to transform the intensity data into line integrals via the logarithm transform:

$$R_\beta = \log_n \left( \frac{I_0}{I_\beta} \right). \quad (5.1)$$



In Eq. (5.1),  $I_\beta$  is the original intensity image at projection angle  $\beta$  (proportional to exposure).  $I_0$  is incident (background) exposure, and  $R_\beta$  is the log transformed image (typically obtained by setting the logarithm base to  $n = e$ ). Data were then reconstructed using the following core algorithm for cylindrical detectors:

$$V(x, y, z) = \int_0^{2\pi} \frac{1}{L^2} \int_{-\gamma_m}^{\gamma_m} R_\beta(\gamma) g(\gamma' - \gamma) \frac{D^2 \cos \gamma}{\sqrt{D^2 + v}} d\gamma d\beta, \quad (5.2)$$

where  $D$  is the source-to-axis distance,  $v$  is the axial- or  $z$ -location of the projected point,  $L$  is the distance from the source to the reconstructed point,  $\gamma$  are the fan beam ray angles, and

$$g(\gamma) = \frac{1}{2} \left( \frac{\gamma}{\sin \gamma} \right)^2 h(\gamma), \quad (5.3)$$

where  $h(\gamma)$  is the Ram-Lak (ramp) filter with optional apodization.

One method for noise reduction currently implemented in clinical FBP reconstruction is the use of apodized filters. Apodization or “removing the foot” is a technical term used to describe a change made to the shape of a mathematical function or signal. In the case of CT, an apodization window is used to suppress high frequency data which is often corrupted by noise and amplified by the ramp filtration step. Figure 5.1 shows some common CT reconstruction filters obtained using different apodization windows.

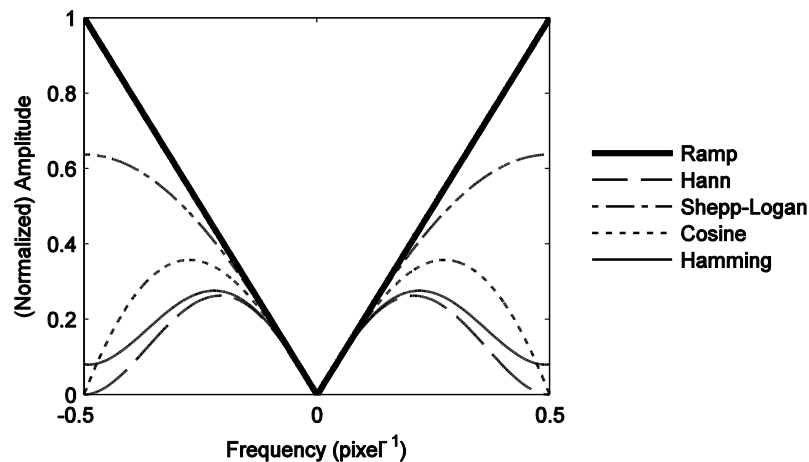


**Figure 5.1: Ramp and apodized reconstruction filters.**

**The ramp filter is required for accurate CT reconstruction. The ramp filter is often apodized to decrease the amount of high-frequency noise in reconstructed images.**

The clinical reference noise levels used to set the XCAT exposure were estimated from clinical images reconstructed with a proprietary “standard” filter. The mathematical definition for this filter was obtained from software licensed to Duke University (CATSIM, GE Healthcare, Waukesha, WI). However, there are clinical scenarios where the standard filter is exchanged for a sharper “detail” filter. The detail filter does not suppress the high frequency content since scans requiring a sharp filter are used for finding fine features such as bone fractures. Images reconstructed with a sharp filter typically have higher noise due to the absence of apodization. This is one scenario where CPNR could have a great impact on noise reduction, so both ramp filtration and standard apodization reconstructions were investigated.

Images from the XCAT MDCT simulation study were reconstructed using a nearest neighbor interpolation scheme onto a 512×512 pixel<sup>2</sup> lattice within a 40×40 cm<sup>2</sup> field of view (0.781×0.781 mm<sup>2</sup> pixels). 32 slices were reconstructed with 0.625 mm slice

thickness. Following reconstruction, four sets of eight adjacent slices were averaged to form four final slices with 5 mm thicknesses (typical slice thickness according to standard clinical protocols). At full dose, the noise standard deviation in the reconstructed XCAT images with standard filtration matched the clinical reference levels.

## **5.1.4 Preliminary Results**

Unprocessed and processed XCAT projection datasets at half and full exposure were reconstructed with ramp and standard filtration. To analyze the impact of noise reduction, the NPS is reported below. Artifacts and edge blurring were analyzed by comparing processed and unprocessed images side-by-side in addition to investigations of difference images.

### **5.1.4.1 NPS Analysis**

The 2-D NPS was measured using Eq. (2.19) and the techniques outlined in section 2.4.1 NPS Analysis. NPS was measured from subtracted images obtained by reconstructing two XCAT datasets with different noise realizations and subtracting the reconstructed images. This was done for half dose, CPNR-processed half dose, and normal dose data. The NPS was estimated from an ensemble of 16 measurements made in the heart region using  $32 \times 32$  pixel<sup>2</sup> ROIs. Data from all four reconstructed slices in a given study were combined to improve the precision of NPS results.

There was notable anisotropy in the 2-D NPS measured from the XCAT phantom data due to the non-uniform (anisotropic) shape of the phantom cross section. This is because the NPS varies in a manner governed by the path length traversed by the beam through the object in the FOV at each projection angle. [166] Due to the anisotropy of the NPS, only vertical 1-D profiles are reported. In Figure 5.2, the vertical 1-D NPS are reported

for half dose, CPNR-processed half dose, and normal dose reconstructed images with ramp filtration and also with standard apodization. Noise measurements from ramp filtered reconstructions with CPNR show 40% noise variance reduction as assessed by the ratio of the integral 2-D NPS with and without processing. The noise reduction benefits of CPNR were somewhat diminished under the apodized reconstruction paradigm where only 33% noise variance reduction was achieved. Since CPNR performs best at mid and high frequencies, suppression of high frequency data by apodization reduces the overall impact of CPNR contributions to noise reduction in this frequency range.

The shape of the CPNR-processed NPS was encouraging. The NPS curves measured from CPNR-processed data in Figure 5.2 have retained the general shape of the original (half dose) NPS. This means that the noise texture in the CPNR-processed images should generally match that of the half and normal dose images (with noise amplitude suppressed to near normal dose levels). The texture of the CPNR residual noise print can be appreciated in Figure 5.3 where the heart detail is compared between the CPNR-processed half dose reconstructions and the normal dose reconstructions.

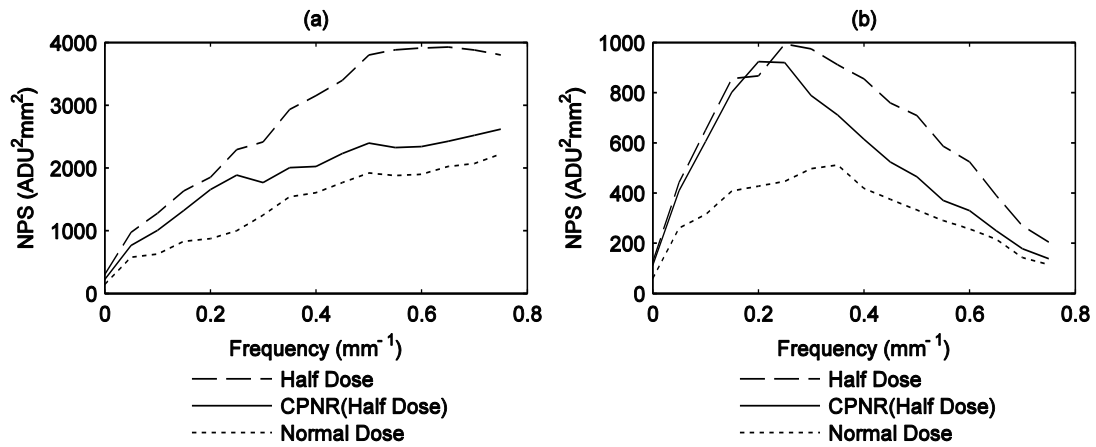


**Figure 5.2: NPS measured from reconstructed XCAT liver images.**

**(a) NPS measured from the liver region of ramp-filtered XCAT images. CPNR processing provides a 40% reduction in total pixel noise variance. (b) NPS measured from the liver region of XCAT images which included standard apodization. CPNR processing provides a 33% reduction in noise variance.**

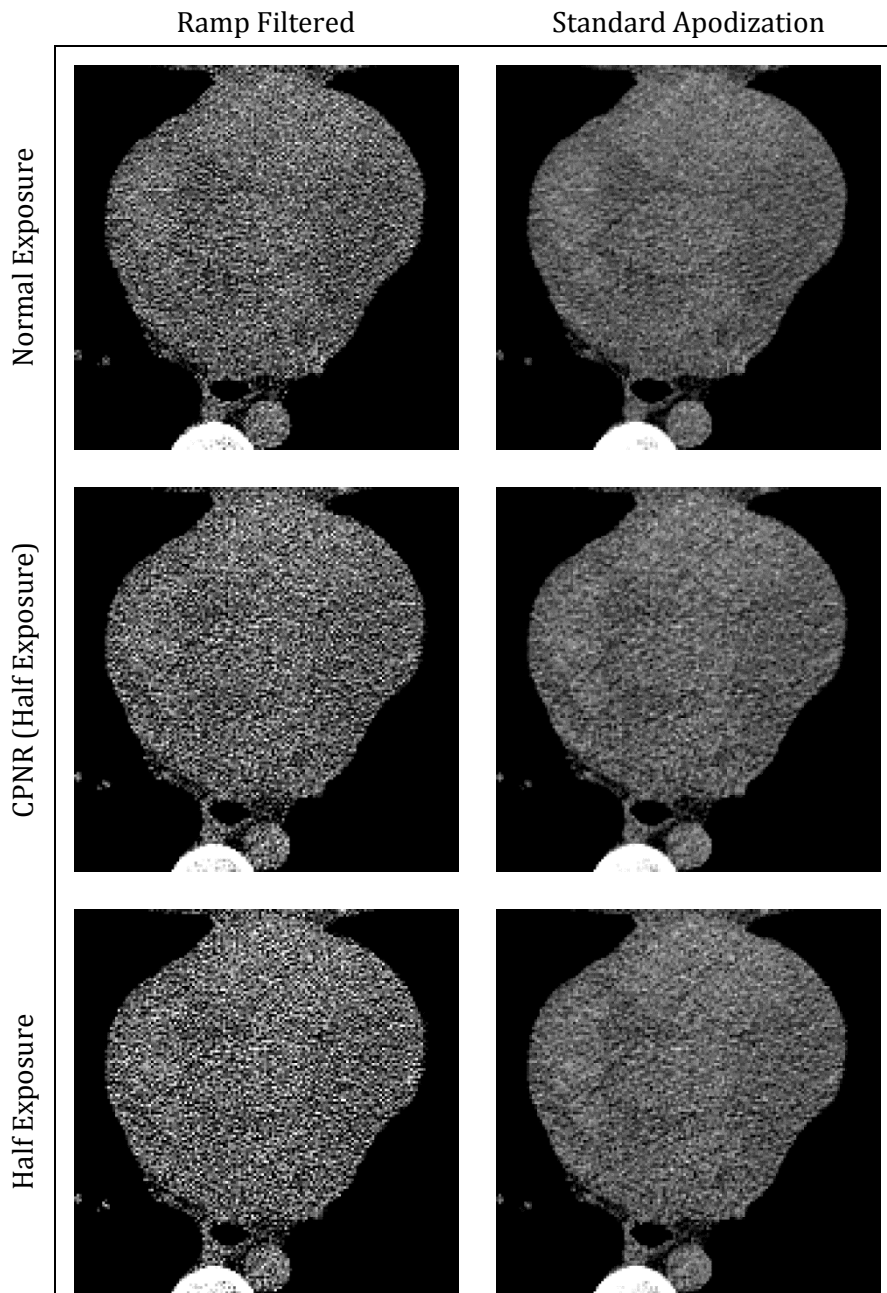
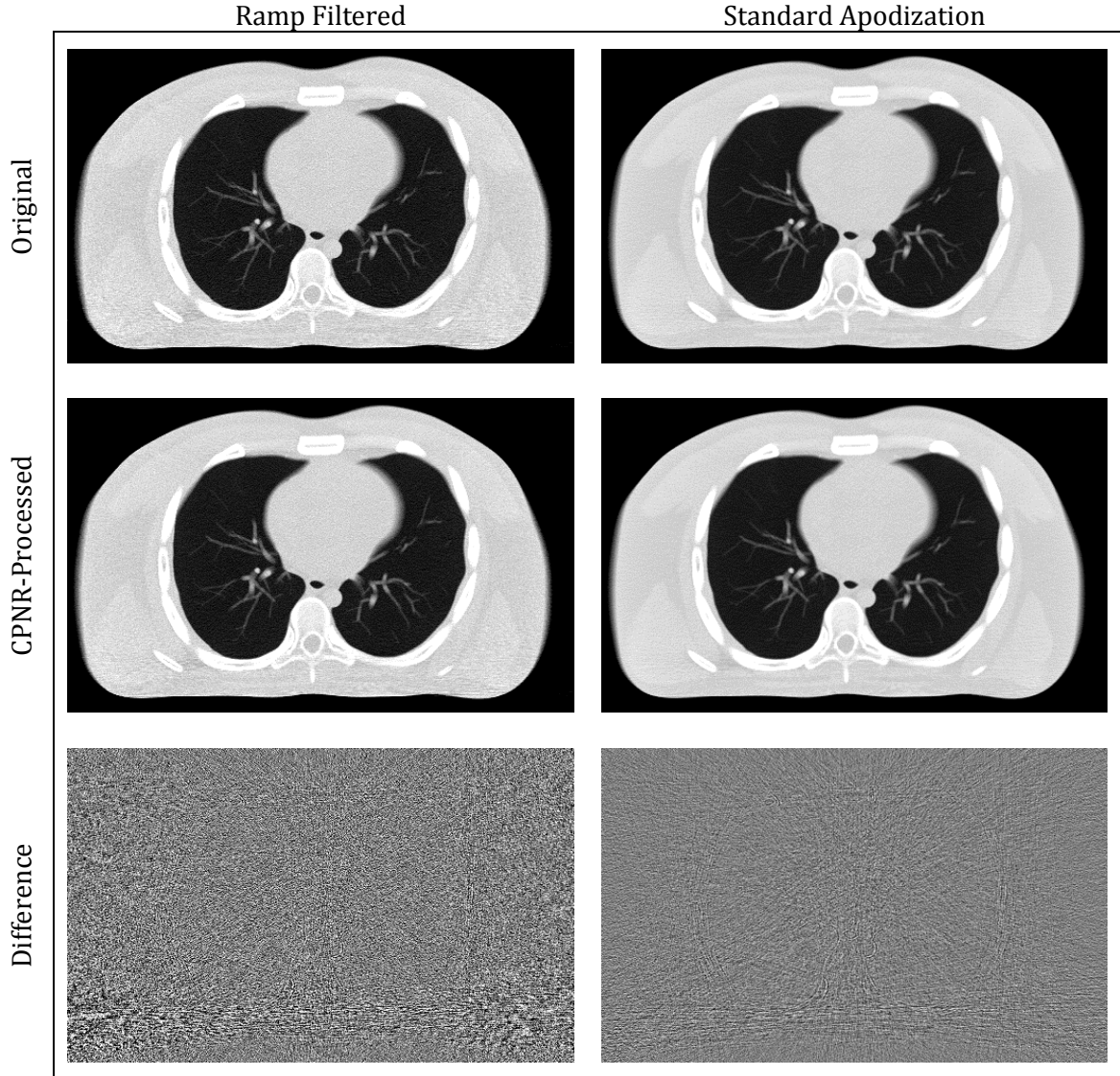


Figure 5.3: Heart detail with and without CPNR processing.

Comparison of unprocessed normal exposure, CPNR-processed half exposure, and half exposure images with tight windowing. Ramp-filtered images exhibit sharper anatomical detail at the expense of higher noise. Apodized reconstruction offers improved noise suppression at the expense of some anatomical blur. Apodization produces a noise print with predominantly mid-frequency noise; the CPNR images show noise which is comparable to that in the unprocessed normal dose images. All images are equally windowed.

#### **5.1.4.2 Artifact Analysis**

Reconstructed lung images are shown in Figure 5.4. The ramp-filtered reconstruction from CPNR-processed data shows good noise reduction with little impact on image edges. Specifically, the fine lung detail shows no apparent blurring, and the crispness of the bony anatomy is retained after CPNR processing. Although the application of an apodizing filter reduces the total noise variance reduction due to CPNR from 40% to 33%, the edge preserving benefits of CPNR are retained as edge effects due to CPNR processing were unobjectionable in both the ramp filtered and apodized images. Only slight edge suppression near the aorta and the vertebral body can be detected in the difference images. Otherwise the anatomical structure is very nicely preserved after appreciable noise suppression by CPNR.



**Figure 5.4: Comparison of XCAT chest CT reconstruction images.**

Images are compared with and without CPNR processing under two different filtration schemes. CPNR applied in the projection image space prior to reconstruction provides 33%-40% total pixel noise variance reduction in the final images with little impact on anatomical edges. Minimal blurring of the aortic and vertebral structures can be observed.



## **5.2 CPNR Application to Cone-Beam CT for Patient Positioning in Radiation Therapy**

After seeing the benefit of CPNR applied to simulated conventional MDCT data, this work also aims to evaluate CPNR applied to physically acquired data. In particular, cone-beam CT (CBCT) application to daily patient positioning for radiation therapy (RT) was chosen as a target for CPNR testing. For nearly a decade, CBCT has been investigated as a clinical tool for daily positioning of patients undergoing RT with medical linear accelerators. [167-169] Volumetric imaging by way of kV CBCT has improved image guidance techniques, [170] and the use of gantry-mounted FPDs for kV imaging has facilitated the integration of advanced imaging systems which provide lower dose to the organs at risk compared to MV CBCT imaging. [171-174]. Although the dose of daily imaging procedures has been lowered through the use of kV imaging technology, the dose per procedure can still be quite high compared to radiological CT applications.

Wen *et al.* [175] studied the dose delivered by a Varian OBI device for a 42 fraction prostate cancer regimen. Although 78 Gy is typically prescribed to the tumor target, the treatment beam delivers far less to the organs at risk. Daily CBCT positioning only contributes  $\approx 2\%$  in additional dose due to imaging, but this dose is spread throughout the entire imaged volume. For example, Wen *et al.* measured cumulative CBCT doses of  $\approx 130$  cGy (central) up to  $\approx 200$  cGy [176] with estimated dose to the femoral heads exceeding 400 cGy (about 12% of the 3400 cGy delivered to the femoral heads by the treatment beam). Other authors also report that it is worth evaluating the costs and benefits of daily CBCT imaging, especially where bony anatomy is concerned. [152, 177] Although the dose due to kV imaging is relatively small compared to the RT treatment dose, there is still considerable interest in the literature for the management of RT imaging dose, [173, 175, 177-180] and

CPNR is investigated here as a competitive method for CBCT dose reduction in image guided radiotherapy.

### **5.2.1 CBCT Data Acquisition**

To investigate the impact of the CPNR algorithm on clinical image quality and the potential for imaging dose reduction in radiation oncology CBCT patient positioning scans, CBCT images of a quality assurance phantom were obtained using a Varian OBI device (Varian Medical Systems, Inc., Palo Alto, CA). The Varian OBI image quality characteristics have been described in detail by Cheng *et al.* [178] The system uses a kV x ray source with nominal tube voltage of 150 kVp with optional bowtie filter. It has a source-to-axis distance of 1000 mm and a source-to-image distance of approximately 1500 mm. The detector is a 397.312 mm x 297.984 mm [512×384 (binned) pixels<sup>2</sup>] indirect-detection FPD with the long dimension perpendicular to the axis of rotation. A scatter rejection grid is installed to improve image contrast. A photograph of the Varian Novalis Tx system to which the OBI device is mounted is provided in Figure 5.5. A schematic of the scan geometry is also provided in Figure 5.6.



**Figure 5.5: Varian OBI system.**

The gantry-mounted kV imaging system is shown with the Catphan phantom in place. The MV treatment head is positioned on top, the kV x ray source is to the left, and the FPD is on the right.

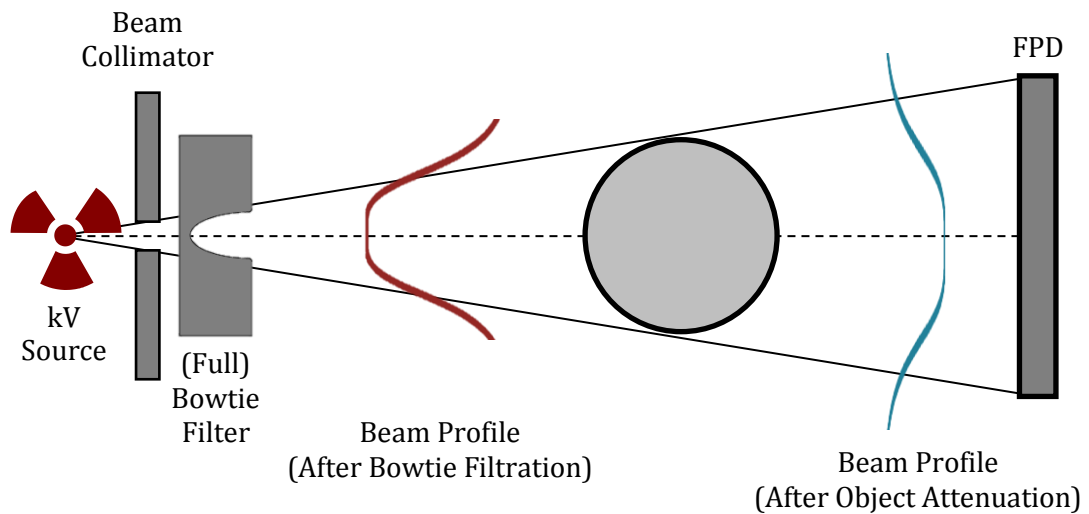


**Figure 5.6: Full fan (half scan) acquisition geometry.**

Using a full fan beam and (full) bowtie filter, data are acquired through  $180^\circ$  plus the fan angle to reduce patient dose. Projection data must be correctly weighted to avoid artifacts due to the short scan acquisition. Sample beam profiles are illustrated to demonstrate the effect of bowtie filtration.

The Catphan® 504 quality assurance phantom (shown in Figure 5.5) was scanned to provide several measures of image quality performance. [181] The Catphan phantom is a standard piece of quality assurance equipment selected by Varian Medical Systems to accompany those linear accelerators equipped with on-board kV imaging capability. The phantom contains four image quality modules: high contrast resolution module; a module for slice width, sensitometry and pixel size; subslice and supra-slice low contrast resolution module; and solid image uniformity module. Each module can be used to assess a different measure of image quality. Images of the phantom were obtained using the default clinical imaging protocols outlined in Table 5.1. Two acquisitions were made using each protocol so that subtracted images could be used for NPS measurements.

**Table 5.1: CBCT clinical protocols and parameters.**

Parameters	Protocol		
	Low Dose Head	Standard Dose Head	High Dose Head
Scan Type	Short Scan	Short Scan	Short Scan
Voltage (kV <sub>p</sub> )	100	100	100
Current (mA)	10	20	80
Pulse length (ms)	20	20	25
Recon. FOV (mm <sup>2</sup> )	250x250	250x250	250x250
Recon. Size (pixels <sup>2</sup> )	512x512	512x512	512x512
Longitudinal Extent (mm)	180	180	180
Slice Thick. (mm)	2.5	2.5	2.5
Convolution Type	RamLak	RamLak	RamLak
Convolution Filter	Standard	Sharp	Sharp

### 5.2.2 Bowtie Filter Images

In CT imaging, compensators (bowtie filters) have been used to reduce patient dose and improve image quality. [18, 19] The bowtie filter, aptly named due to its bowtie shape, is a block of attenuating material which modulates the beam intensity across the projection

FOV. The filter selectively reduces x ray flux by attenuating the x ray beam over areas of the FOV where objects (e.g. patient anatomy) are expected to be thinnest (i.e. less attenuating) and vice versa. Doing so provides three primary benefits. One, patient dose is reduced by preventing over-exposure of the skin and extremities. Two, scattered radiation is reduced by reducing the total amount of radiation incident on the patient. And three, the full dynamic range of digital detectors can be better utilized by reducing the maximum beam intensity in those parts of the beam left otherwise unattenuated by objects in the FOV.

A bowtie filter is regularly used in daily CBCT patient positioning, so one was also used for test data acquisition. This required a second set of images to be acquired with only the bowtie filter in the beam for each imaging procedure listed in Table 5.1. These bowtie filter images were then used to correct for the gross pixel intensity changes across the FOV which resulted from the nonuniform x ray intensity profile created by the filter. The general shape of the bowtie filter and its effect on the x ray beam profile can be appreciated in Figure 5.6 and Figure 5.7. The bowtie correction procedure is explained in full detail in 5.2.4.1 Bowtie Filter and Crescent Artifact Correction.

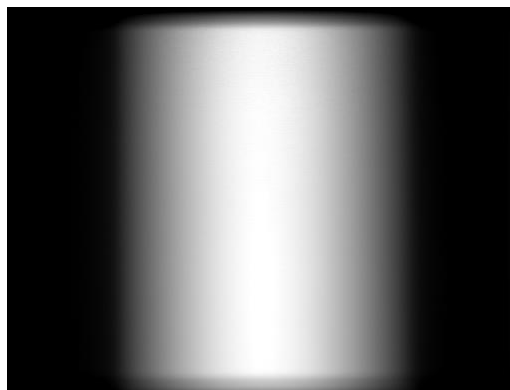


**Figure 5.7: Bowtie filter image.**

**Sample image of a (full) bowtie filter. X ray transmission through the filter is highest at the white pixels and lowest at the black pixels.**

### 5.2.3 CPNR in CBCT Projection Space

Both CPNR optimization settings derived earlier in this dissertation were investigated in application to CBCT projection data: the image blending scheme from Chapter 2 and the CT optimization in section 5.1.2 CPNR Optimization in MDCT Projection Space. The raw projection images were denoised using each CPNR optimization, and it was found that the optimization for MDCT outperformed the optimization from Chapter 2. To eliminate some remaining blur, the  $t_W$  parameter was given a value of  $t_W = 1$  and the algorithm was run for three iterations with settings  $(p, \ell, t_{EST}, t_W, t_{MAJ}) = (4, 9, 0, 1, 0.5)$ . Note that the  $t_{MAJ}$  becomes irrelevant since only a single polarity estimate is made at each pixel when  $t_W = 1$ . Therefore,  $t_{MAJ} = 0.5$ . Data acquired using the Low Dose Head protocol (Table 5.1) were denoised in projection space (prior to the bowtie correction described later). Noise variance reduction was estimated by taking the ratio of pixel variance in a  $16 \times 16$  pixel<sup>2</sup> ROI measured at the center of subtracted images before and after processing. Noise variance reduction of 50% was achieved by CPNR in projection space.

### 5.2.4 FBP Reconstruction from FPD Data

Reconstruction of CBCT images in clinical RT practice continues to routinely employ the fast and efficient algorithm of Feldkamp, David, and Kress. [153, 168, 171, 182] An in-house MATLAB implementation of the algorithm was developed in conjunction with other projects involving the development of a lower cost CT system with similar FPD system geometry. [183, 184]

CT reconstruction is most conveniently performed in a rotated coordinate system. The conventional Cartesian coordinate system is simply rotated about the z-axis to orient

the system according to the acquisition angle of each projection image as it is back-projected into the reconstruction matrix according to the following equations

$$\begin{aligned} s &= -x \sin(\beta) + y \cos(\beta), \\ t &= x \cos(\beta) + y \sin(\beta), \end{aligned} \quad (5.4)$$

where  $x$  and  $y$  are the spatial coordinates and  $\beta$  is the projection view angle. The algorithm core is similar to Eq. (5.2) and is as follows:

$$V(x, y, z) = \int_0^{2\pi} \frac{\rho^2}{(\rho - s)^2} \int_{-\infty}^{\infty} R_{\beta}(p, \xi) W(\theta) f\left(\frac{\rho}{\rho - s} t - p\right) \frac{\rho}{\sqrt{\rho^2 + p^2 + \xi^2}} dp d\beta. \quad (5.5)$$

The reconstruction volume  $V(x, y, z)$  is computed using the following terms. First, Projection data are pre-weighted by the location-dependent factor  $\frac{\rho}{\sqrt{\rho^2 + p^2 + \xi^2}}$  where  $\rho$  is the source-to-axis distance,  $p$  is the projection sample location, and  $\xi$  is the location in the axial ( $z$ ) direction. Log-transformed data  $R_{\beta}(p, \xi)$  [Eq. (5.1)] must then be filtered by a reconstruction kernel  $f\left(\frac{\rho}{\rho - s} t - p\right)$ . As discussed previously, this is typically either a Ram-Lak (ramp) filter or an apodized ramp filter. To emulate the apodization of clinical CBCT data, a cosine filter was chosen. Filtered projection data may then be weighted by a beam weighting function  $W(\theta)$ . Finally, the data are back-projected with weights  $\frac{\rho^2}{(\rho - s)^2}$  which are dependent upon the distance of the reconstruction voxel from the x ray source. Although reconstruction with Eq. (5.5) is straightforward, several corrections to the data needed to be made.

#### 5.2.4.1 Bowtie Filter and Crescent Artifact Correction

Due to the use of a bowtie filter, projection images required bowtie gain correction prior to reconstruction. According to Matsinos *et al.*, [169] the images generated by the

Varian OBI CBCT reconstruction software (Varian Medical Systems, Inc., Palo Alto, CA) use only a single bowtie filter image for bowtie correction at all angles. This is problematic for several reasons. It has been known for some time that the Varian OBI system is prone to “bowtie wobble” or “crescent” artifacts which can be attributed to the use of a single bowtie correction image (Figure 5.8). This artifact has been attributed to detector-source misalignment due to system sag and mechanical instability in the bowtie filter assembly. [185, 186] Both of these issues can cause the default bowtie correction image to be misaligned with the actual bowtie filter position relative to the other imaging system components causing very strong artifacts to appear near image regions where the bowtie filter gradient is steepest.

To solve this problem, Giles, *et al.* [185] proposed the use of many bowtie filter correction images to account for system instabilities which influence bowtie filter positioning. Following their recommendations, 380 bowtie filter images were acquired corresponding to each of the gantry angles used to acquire data in the current study. To account for fluctuations in detector exposure from image-to-image, the average pixel intensity was measured using a 20x20 pixel<sup>2</sup> ROI at field center in each image. The plot of intensities as a function of projection angle was then smoothed using local quadratic fitting. Then each image was normalized through division by the smoothed value. To reduce the influence of noise in the correction images, every bowtie filter image was averaged with its 16 closest neighbors. Once the bowtie filter data were normalized and averaged, every raw projection image requiring bowtie correction was divided by the bowtie filter image acquired at the closest angle. This ensured that system sag and bowtie filter shift properties were very similar between the paired images. The High Dose Head protocol was used to



perform bowtie correction for all reconstructed datasets since those data had the highest SNR.

Comparing reconstructed images from the Varian OBI system to those produced using in-house reconstruction software, it can be seen in Figure 5.8 that the crescent artifacts have been virtually eliminated. By following the recommendations provided above, the use of acquisition angle-dependent bowtie filter correction images accounted for detector-source sag and bowtie filter wobble, both major contributors to crescent artifacts in other more simplistic bowtie correction schemes.

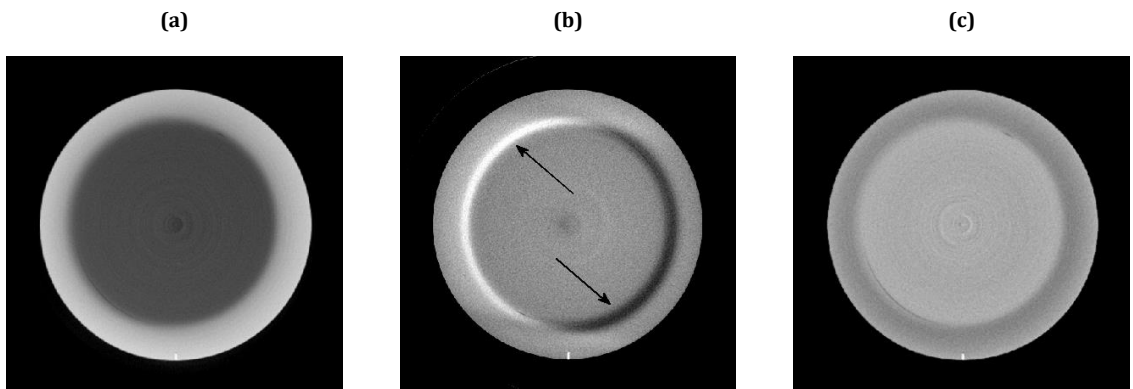


**Figure 5.8: Bowtie and crescent artifact correction.**

**(a) Reconstructed image without bowtie correction. (b) Reconstructed image with simplistic bowtie correction which results in crescent artifacts (indicated by arrows). (c) Reconstructed image with improved bowtie correction which greatly reduces the appearance of crescent artifacts.**

#### **5.2.4.2 Short Scan Weighting Function**

The OBI short scan geometry requires  $180^\circ$  plus the full fan angle to be scanned for complete angular coverage of the scanning FOV. Whereas full ( $360^\circ$ ) scanning results in the acquisition of two complete projection datasets, short scanning results in the acquisition of one complete and one partial projection dataset. Therefore, redundant data (data collected along the same projection line but in opposite directions) must be appropriately weighted

so that the sum of their weights is unity. Several authors have reported on short scan beam weighting functions. [187-189] In this work, the original short scan weighting scheme of Parker was implemented: [190]

$$W(\theta) = \begin{cases} \sin^2 \left[ \frac{\pi(\theta - \gamma_m)}{2\Delta} \right], & \gamma_m \leq \theta < \gamma_m + \Delta \\ 1, & \gamma_m + \Delta \leq \theta < \gamma_m + \pi \\ \cos^2 \left[ \frac{\pi(\theta - \gamma_m - \pi)}{2\Delta} \right], & \gamma_m + \pi \leq \theta < \gamma_m + \Delta + \pi \\ 0, & \text{otherwise.} \end{cases} \quad (5.6)$$

$W(\theta)$  is the data weighting function,  $\theta$  is the projection angle,  $\gamma_m$  is the maximum fan beam half angle, and  $\Delta$  is the acquisition angle in excess of  $180^\circ$  plus the fan angle. The sinusoidal weighting functions produce a weight which smoothly transitions between redundant and single acquisitions which are given unit weight.

#### 5.2.4.3 Rudimentary Scatter Nonuniformity Correction

Due to the use of half scan protocols and the lack of a projection space-based scatter correction, there was asymmetric scatter artifact in the short scan reconstructions. This caused differences in the apparent material density at opposite ends of the phantom in the reconstructed images. To correct this, a 2-D first order polynomial (planar) correction was applied to the data. The 2-D function was fit to 4096 sample points from the center portion of a reconstructed slice through the uniform phantom module. Once the fit was obtained, it was subtracted from all reconstructed slices from the same phantom scan. Figure 5.9 depicts the process by which sample points were selected, fit, and how the correction improved the uniformity of the scatter artifact throughout the reconstructed image. Although this did not correct for the radial component of the scatter artifact [still remaining in Figure 5.9(d)], it did improve the uniformity of the scatter artifact. It is not anticipated

that the residual scatter in the reconstructed images will negatively affect the measurements associated with denoising algorithm performance.

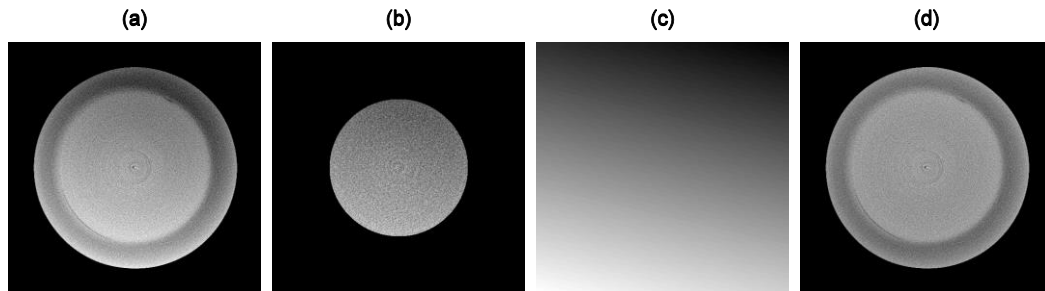


**Figure 5.9: Rudimentary scatter anisotropy correction.**

**(a) Scatter artifact is not radially symmetric due to the short scan acquisition. (b) 4096 points within the central region are selected at random for plane fitting. (c) The first order correction derived from polynomial fitting. (d) The scatter anisotropy has been corrected leaving only the radial component of the scatter artifact.**

## **5.2.5 Catphan Analysis**

Images were reconstructed using a nearest neighbor interpolation scheme onto a  $512 \times 512$  pixel<sup>2</sup> lattice within a  $25 \times 25$  cm<sup>2</sup> field of view ( $0.488 \times 0.488$  mm<sup>2</sup> pixels). For each slice to be reconstructed, thin slices were reconstructed with 0.5 mm slice thickness and five adjacent thin slices averaged to form a 2.5 mm final slice which matched the thickness typically used in the clinic. Several slices were reconstructed through different image quality modules within the Catphan phantom. The uniform, high-contrast, and sensitometry modules were selected to perform NPS and resolution analysis.

### **5.2.5.1 Radial NPS**

NPS was assessed in the uniform region of the Catphan phantom. Although the actual phantom was comprised of a uniform fill material, pixel gain nonuniformities in the FPD produced ring artifacts which corrupted the apparent uniformity of the reconstructed images. In spite of extended efforts to eliminate the ring artifacts, they persisted. According

to other investigators, this problem is not uncommon. To prevent structured noise components such as ring artifacts from contaminating NPS measurements, the 2-D NPS was measured from subtracted images.

Since the Catphan phantom has radially symmetric cross section, the 2-D NPS does not exhibit the anisotropies observed in NPS measured from the XCAT phantom. Therefore, since the 2-D NPS measurements [Eq. (2.19)] taken from the CATPHAN phantom appeared to be radially symmetric, measurement precision was improved through radial averaging of the 2-D NPS: [191]

$$NPS(f) = \frac{1}{N_f} \left[ \sum_{f \leq \sqrt{u^2 + v^2} < f + \Delta f} NPS(u, v) \right]. \quad (5.7)$$

In Eq. (5.7),  $u$  and  $v$  are the respective horizontal and vertical spatial frequency components of the 2-D NPS  $NPS(u, v)$ ;  $f$  is the radial frequency component;  $\Delta f$  is the radial sample spacing; and  $N_f$  is the number of points within the interval  $f \leq \sqrt{u^2 + v^2} < f + \Delta f$ . The 2-D NPS [ $NPS(u, v)$ ] was assessed using 16,  $32 \times 32$  pixel<sup>2</sup> ROIs in the center of the uniform Catphan module as shown in Figure 5.10. Noise measurements from ramp filtered reconstructions showed 49% noise variance reduction as determined by comparing the integral of the 2-D NPS in the reconstructed images before and after processing with CPNR. With apodization, CPNR was able to achieve 42% noise variance reduction with only modest excess of low-frequency noise.

Plots of the 1-D radially averaged NPS measurements are provided in Figure 5.11. They show that CPNR-processing has generally retained the noise texture while providing a possible two-fold reduction in dose. Although there is a small amount of excess low frequency noise left after CPNR-processing, the sample images in Figure 5.12 show that

such a modest change is not objectionable. The residual noise texture in the CPNR-processed Low Dose Head data looks very similar to that in the Standard Dose Head images in the case of both ramp filtered and cosine apodization.

In a bit of a sidebar, the author would like to comment on the NPS plots in Figure 5.11. The ramp filtered results [Figure 5.11(a)] share some similar properties with the measurements made on ramp filtered XCAT data in Figure 5.2(a) with the exception that the plots generated from ramp filtered CBCT data show some apparent suppression at high frequencies. In other words, the plots in Figure 5.11(a) do not exhibit the characteristic ramp shape that is demonstrated by the data in Figure 5.2(a). The reason for this difference is that the noise in the OBI CBCT projections is correlated according to the NPS associated with the indirect-detection FPD whereas the noise in the simulated XCAT MDCT projection images is spatially uncorrelated. The correlations in the OBI projection data propagate through the reconstruction process and into the reconstructed images. The ramp shape may however be restored by prewhitening the projection data. Regardless, the CBCT noise reduction results are very positive and very promising for both ramp and cosine apodization schemes.

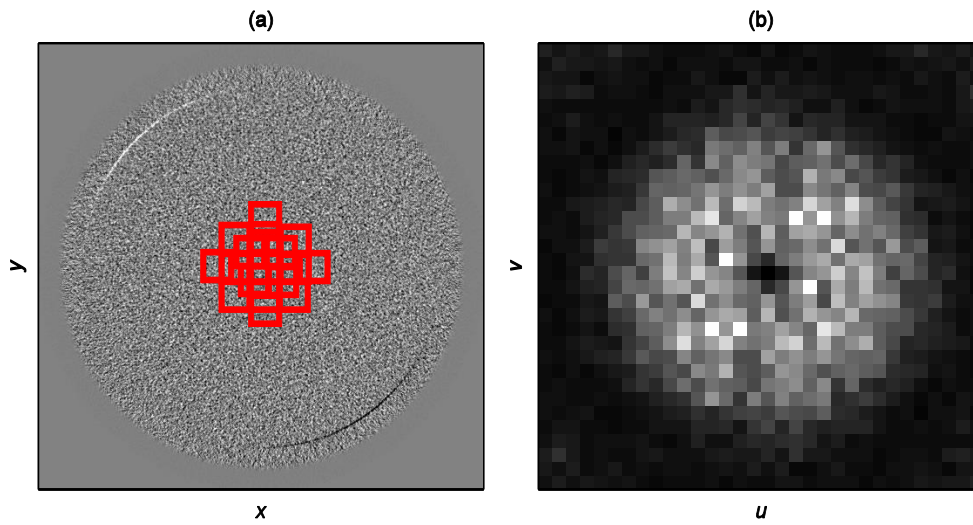


Figure 5.10: 2-D NPS measurement from Catphan data.

(a) The NPS was measured using the red ROIs in the center of the uniform phantom module. Subtracted images were used to avoid the confounding influence of ring artifacts. (b) The 2-D NPS as measured from apodized data is radially symmetric due to the radial symmetry of the phantom.

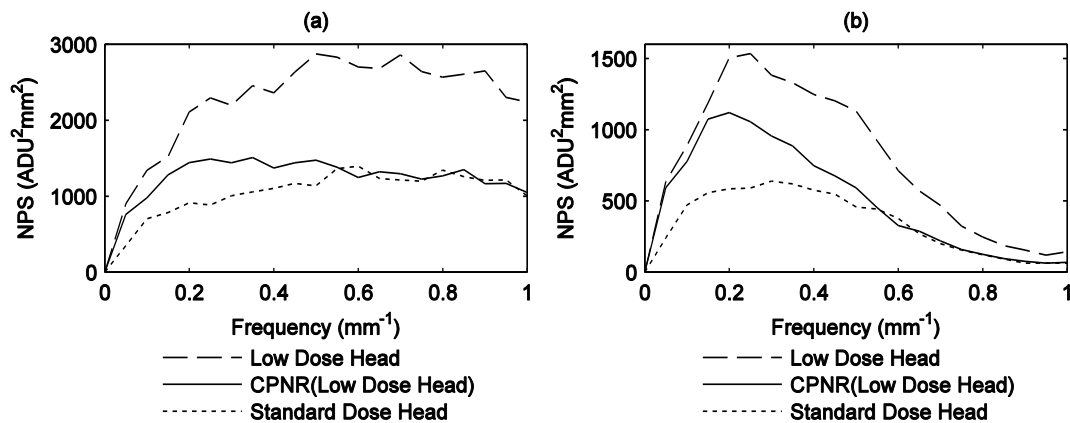


Figure 5.11: NPS measured from uniform module of Catphan phantom.

(a) NPS measured from the uniform module of ramp-filtered Catphan images. CPNR processing provides a 49% reduction in total pixel noise variance. (b) NPS measured from the uniform module of cosine-filtered Catphan images. CPNR processing provides a 42% reduction in noise variance.

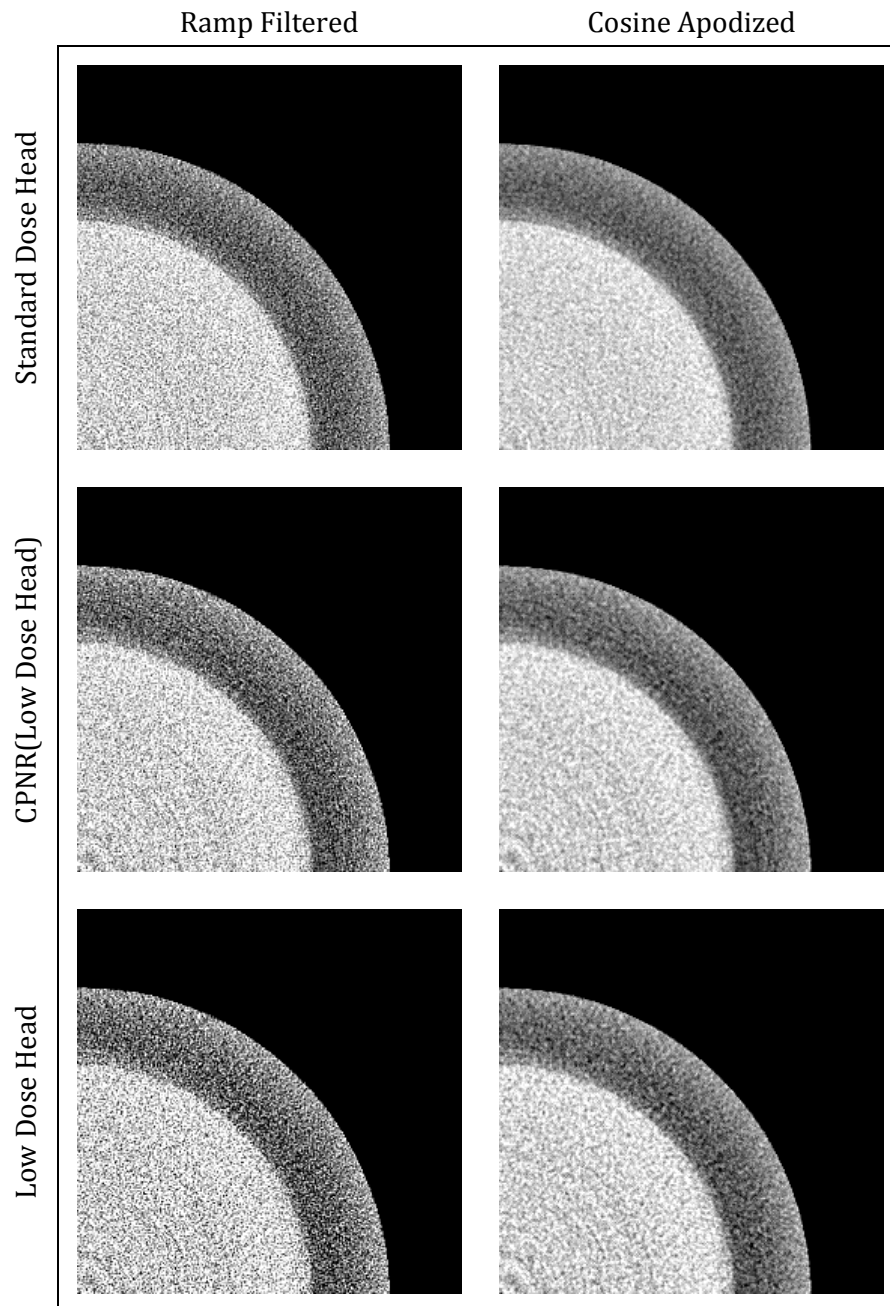


Figure 5.12: Catphan noise textures.

Reconstructed slices from the uniform module of the Catphan phantom show differences in the noise texture as a result of differences in dose, CPNR processing, and apodization. CPNR processing has left a slight excess of low-frequency noise in the residual noise print which is evident in the reconstructed images. All images are equally windowed and leveled.

### 5.2.5.2 High Contrast Resolution

An axial slice was reconstructed through the high contrast resolution module of the Catphan phantom with and without CPNR processing. The high contrast resolution module provides a simple measure of resolution performance through the use of metal bar phantoms with different bar thickness and spacing ranging from 1 line pair (lp) per cm to 21 lp/cm. Reconstructed images with and without CPNR processing can be compared in Figure 5.13 with ramp and cosine filtration. The baseline performance of the system was determined to be 10 lp/cm with ramp filtration and 8 lp/cm with cosine filtration. After CPNR processing, the 10 lp/cm insert was resolved with ramp filtration. Only 7 lp/cm was resolved after CPNR processing with cosine apodization indicating modest loss of high contrast resolution performance. To ensure the accuracy of high contrast resolution results, reconstructed slices from multiple CPNR-processed low dose studies should be averaged to ensure that stochastic noise does not negatively influence the interpretation of results.



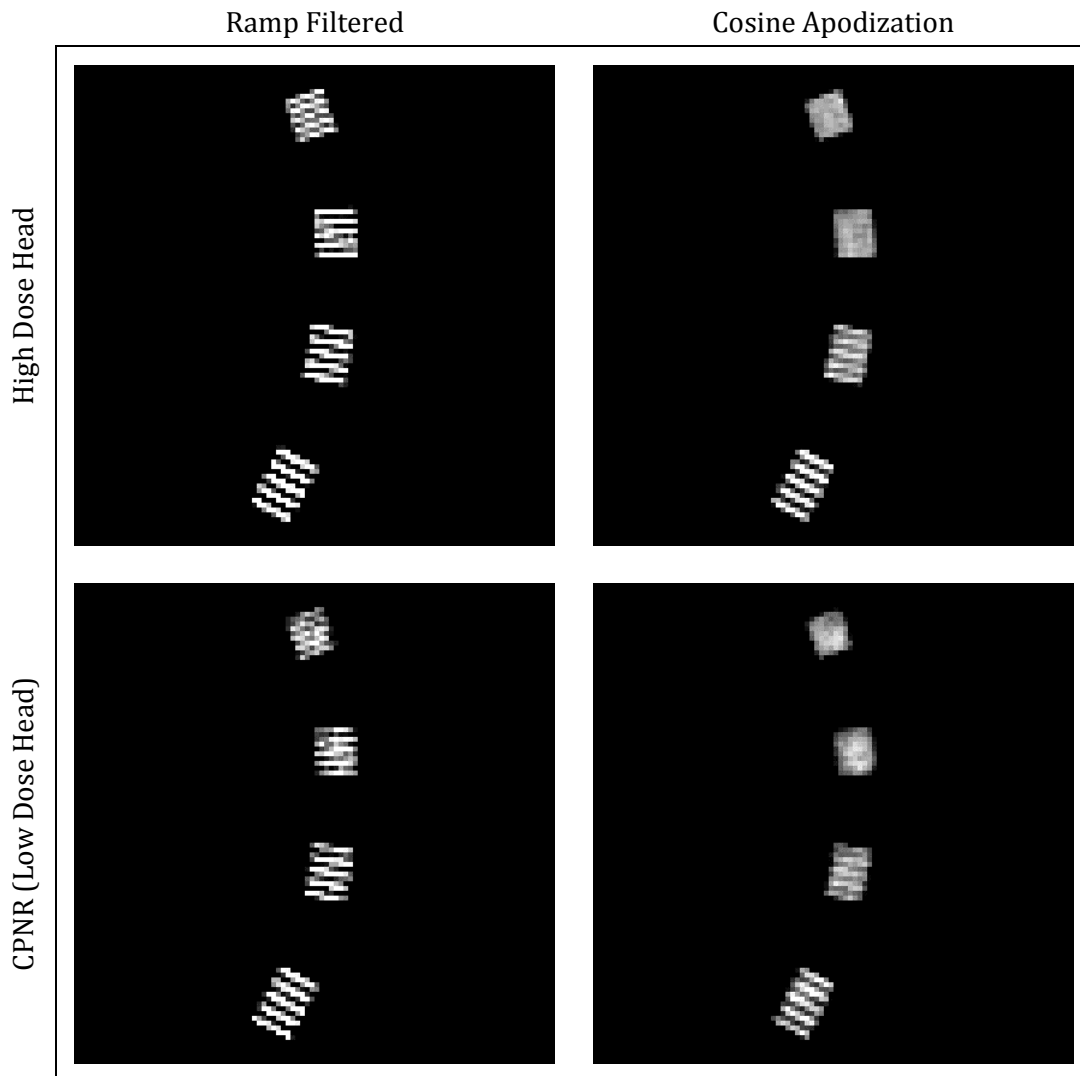


Figure 5.13: High contrast resolution module analysis.

Images show the 7, 8, 9, and 10 lp/cm bar phantoms. Using ramp filtration, 10 lp/cm was resolved for both the unprocessed High Dose Head protocol and the CPNR-processed Low Dose Head (11 lp/cm was unresolved in both instances). With cosine apodization, 8 lp/cm is resolved in the unprocessed image while only 7 lp/cm is clearly resolved after CPNR processing.

### 5.2.5.3 Task Transfer Function

To further measure the effects of denoising on resolution, the task-based modulation transfer function or task transfer function (TTF) was employed. Richard *et al.* [118] showed that a contrast-dependent measure of the radially symmetric ESF can be readily obtained from the sensitometry disks implanted in most quality assurance phantoms; such disks are available in the Catphan phantom. The TTF is derived from radially averaged measures of the ESF according to the equation

$$ESF(r) = \frac{1}{N_f} \left[ \sum_{r \leq \sqrt{(x-x_0)^2 + (y-y_0)^2} < r + \Delta r} E_{DISK}(x, y) \right]. \quad (5.8)$$

$ESF(r)$  is a finely-sampled estimate of the 2-D disk edge function  $E_{DISK}(x, y)$ . In a manner similar to Eq. (5.7), the  $E_{DISK}(x, y)$  samples are organized using a binning operation wherein  $x$  and  $y$  are the respective horizontal and vertical spatial coordinates;  $(x_0, y_0)$  denotes the disk center (obtained from a center-of-mass calculation);  $r$  is the distance of each pixel to the disk center;  $\Delta r$  is the radial sample spacing; and  $N_f$  is the number of sample points within the interval  $r \leq \sqrt{(x - x_0)^2 + (y - y_0)^2} < r + \Delta r$ . Once obtained,  $ESF(r)$  is a rebinned and finely sampled 1-D ESF estimate which can be processed according to the detailed instructions contained in section 3.2.3.4 Edge Image Processing, This includes all denoising considerations and correction factors derived for edge signal processing in Chapter 3.

When measured as a function of different task parameters (e.g. object diameter, noise magnitude, object contrast), the TTF has been shown to vary under nonlinear image processing paradigms such as nonlinear CT reconstruction. [192] By taking ESF measurements of the different material inserts in the Catphan phantom, the TTF can be

determined as a contrast-dependent function of nonlinear algorithm resolution performance Table 5.2 provides the material identities and associated HU estimates from each insert, and Figure 5.14 shows the TTF measured for three Catphan material inserts.<sup>1</sup>

The TTF measured from CPNR-processed Low Dose Head reconstructions was nearly equal to the TTF measured from High Dose Head reconstructions for the air and Teflon inserts. At half the cutoff frequency ( $f_c = 1 \text{ mm}^{-1}$ ), the TTF of CPNR-processed data measured only 1% and 5% lower than the TTF of unprocessed data measured from air and Teflon inserts, respectively. These percentages represent the average TTF reduction due to CPNR from both ramp and cosine reconstructions. To measure the TTF of a lower contrast material, the Delrin insert was selected. The CPNR-processed data showed 13% reduction in TTF at the cutoff suggesting that CPNR performance is indeed contrast dependent. Overall, the TTF measured from CPNR-processed data showed excellent TTF response with contrast-dependent characteristics that merit further investigation.

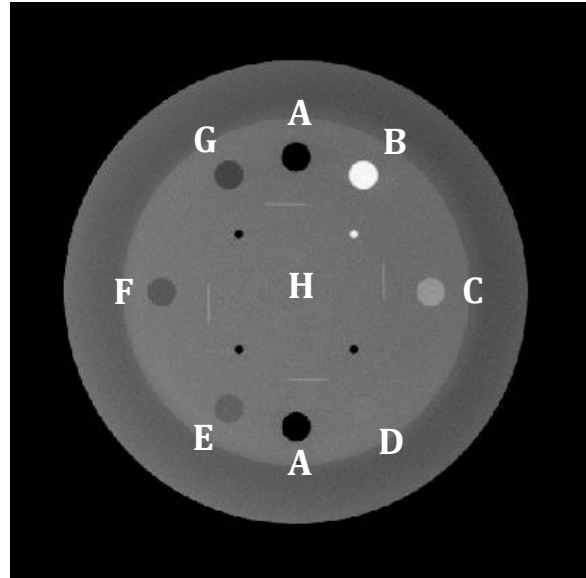
---

<sup>1</sup> Due to the relatively high noise in the Low Dose Head scans combined with the availability of only two datasets, several of the low contrast TTF measurements were simply too noisy to report.

**Table 5.2: Catphan material definitions.**

**Materials were listed in the Catphan user manual. HU estimates were obtained from clinical quality assurance protocols.**

ID	Material	HU
A	Air	-1000
B	Teflon	990
C	Delrin	340
D	Acrylic	120
E	Polystyrene	-35
F	LDPE	-100
G	PMP	-200
H	Background	≈90



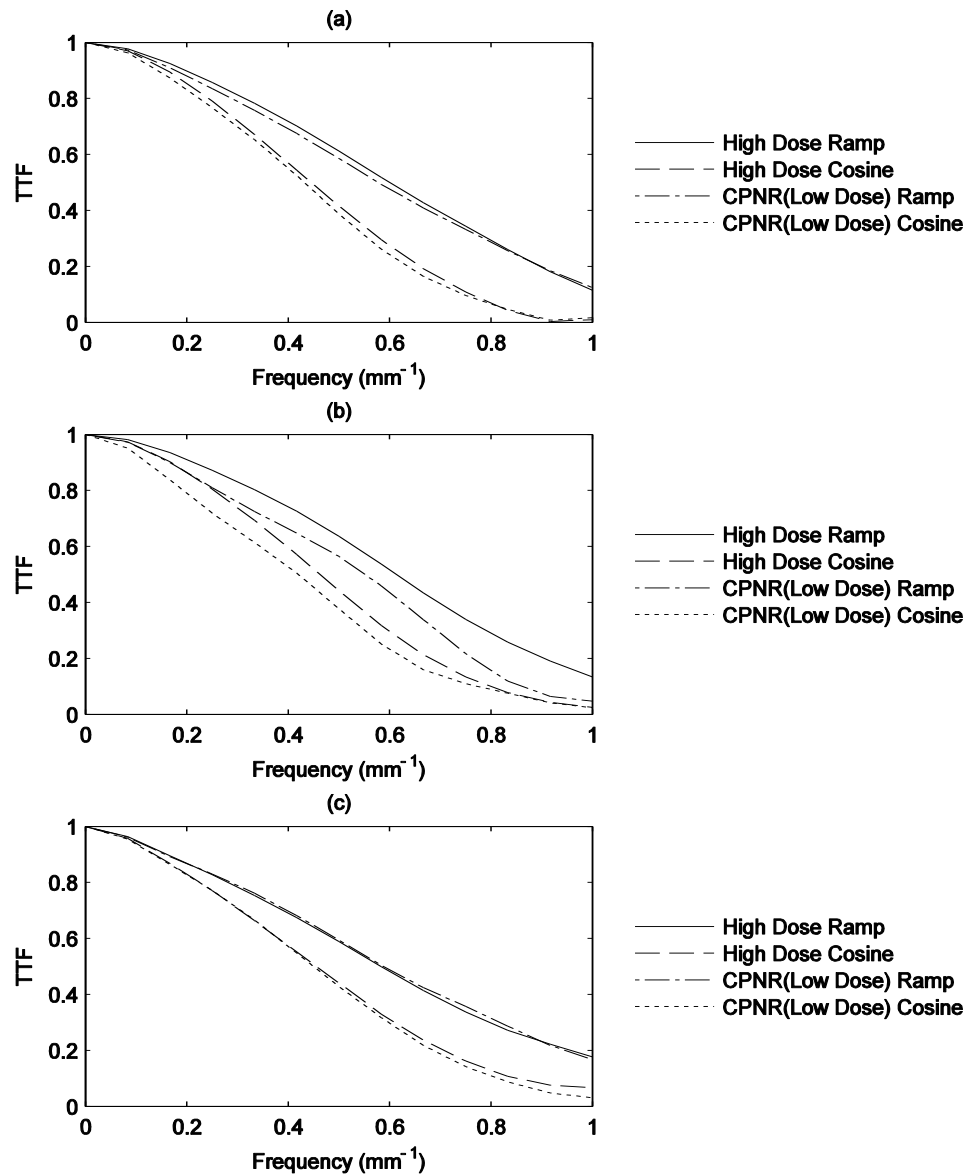


Figure 5.14: TTF measured from three sensitometry inserts.

The TTF was measured from (a) Teflon, (b) Delrin, and (c) Air sensitometry inserts. Only slight differences were observed between TTF measurements from different materials without CPNR processing. TTF measured from CPNR-processed data showed excellent TTF response with contrast-dependent characteristics. At half the cutoff frequency ( $f_c = 1 \text{ mm}^{-1}$ ), the TTF of CPNR-processed data measured only 1%, 13%, and 5% lower than the TTF of unprocessed data measured from air, Delrin, and Teflon inserts, respectively. These percentages represent the average between ramp and cosine reconstructions.

### **5.3 Discussion**

Preliminary application of CPNR to simulated MDCT data showed great promise. When denoising was applied in projection space, pixel noise variance in the reconstructed images was reduced by 40% with almost no blurring of anatomical structures. After reviewing images with and without CPNR processing, no new artifacts were observed. When apodization of the ramp-filtered projection data was applied, noise variance reduction dropped to 33%, still with only minor edge blurring. Although the NPS (Figure 5.2) measured from CPNR-processed images showed modest residual low frequency noise, this was not objectionable in comparisons of processed and unprocessed images in Figure 5.3.

One major area of research in MDCT to which CPNR has not yet been applied is iterative reconstruction. Iterative reconstruction methods such as Adaptive Statistical Iterative Reconstruction [193] and Model-Based Iterative Reconstruction (MBIR) (GE HealthCare, Waukesha, WI) have been commercially popularized, and reports indicate that techniques like ASIR have the ability to practically reduce imaging dose by 23-66% with some authors reporting dose reductions of up to 82%. [22, 194] Other authors have even reported on resolution improvements with the use of iterative and model-based reconstruction methods. [23, 118] There is interest in exploring how projection space denoising and iterative reconstruction methods might be used in combination to provide multiplicative noise reduction benefits since the two methods approach the noise reduction problem from two different perspective. However, such work is left to future endeavors.

In another application, CPNR was used to denoise RT quality assurance phantom data obtained using CBCT. CPNR achieved a 49% reduction in noise variance with ramp filtration and 42% reduction in noise variance with cosine apodization. These noise

reduction levels were accompanied by only minimal edge blurring with no apparent artifacts. High contrast resolution analysis revealed no apparent loss of high contrast resolution under ramp filtration with CPNR and the loss of only 1 lp/cm when cosine apodization was applied. Further resolution analysis using the TTF showed excellent CPNR resolution preservation based measurements made from air and Teflon inserts while the TTF measurement from the lower contrast Delrin insert revealed modest TTF suppression of about 13% due to CPNR processing. Therefore, these results show great promise for CPNR as a possible means of reducing the daily radiation burden from CBCT imaging in RT by a factor of two.

There is reason to believe that a 3-D CPNR implementation could improve upon the proposed projection space denoising paradigm. By including the angular dimension in the denoising process, image denoising could be improved by exploiting redundancies in the anatomical detail which slowly changes through the angular dimension. So called sinogram denoising may have the two-fold effect of improving anatomical edge preservation and improving low frequency noise reduction. Low frequency noise performance might be improved since the noise in the angular dimension is uncorrelated from projection to projection, and the inclusion of this extra information stands to improve the integrity of the noise reduction process. The same can be said for 3-D spatial denoising as well which further emphasizes the need to develop a 3-D CPNR implementation as part of future investigations.

## 6. Concluding Remarks

This dissertation has thoroughly explored the novel CPNR concept in application to radiography and CT. It was developed in the first chapter from fundamental principles into an effective medical image noise reduction tool. In application to digital radiography, CPNR reduced stochastic image noise variance by a factor of three at mid and high frequencies with more modest noise reduction achieved at low frequencies. Its performance was shown to be on par with other noise reduction algorithms in terms of noise variance reduction, but CPNR showed marked benefits in terms of other image quality characteristics. CPNR reduced the amount of edge artifacts and blurring, improved low contrast resolution preservation, and produced a residual noise print with “normal” appearance.

This work provided a new set of tools for assessing the frequency response and distortion properties of nonlinear algorithms. Whereas other more traditional resolution assessment tools fail to explicitly assess the effects of algorithm nonlinearity, this novel contribution to the field of image metrology independently analyzes signal distortion and contrast resolution effects. The work in Chapter 4 showed that, for nonlinear algorithms, this tool can provide a means of quantifying the extent of algorithm nonlinearity through measurement of the nonlinear distortion imposed on sinusoidal signals of interest. A figure of merit (DI) was proposed as a means of quantifying the degree to which nonlinear algorithm effects will impact algorithm performance compared to algorithm contrast resolution effects in the context of normal clinical application – a very important achievement.

Finally, the last chapter showed that CPNR can be used for noise reduction in CT. Through a simulation study of MDCT, 40% reduction in noise variance was demonstrated



with minimal negative effect on reconstructed image resolution. In combination with ramp filter apodization, CPNR reduced noise variance by an additional 33% over the use of apodization alone. In application of CPNR to CBCT data, the algorithm reduced total pixel noise variance by 49% with ramp filtration and 42% with cosine apodization. An investigation of high contrast resolution effects showed minimal resolution degradation. This observation which was supported by TTF analysis of phantom sensitometry inserts in reconstructed CBCT images which revealed only 1%-13% reduction in TTF after CPNR processing. Further optimization of the CPNR parameter space in addition to the development of a 3-D CPNR algorithm may help to further improve the performance of CPNR in CT.

CPNR represents a new noise reduction paradigm which has contributed some improvements to medical image denoising. It represents a substantial leap in the way noise reduction is understood and performed by suggesting that noise polarity assessment combined with random number subtraction can be used to reduce image noise by a factor of two to three with minimal impact on resolution. By subtracting random noise from a suitable distribution, CPNR accomplished the noise reduction objectives set out at the beginning of this dissertation. Overall, resolution was well preserved after CPNR application. It was used to demonstrate improved low-contrast resolution performance over other advanced denoising algorithms. The residual CPNR noise print was also shown to have “normal” characteristics in terms of the residual noise distribution and texture. Although there are improvements which can be made in terms of low-frequency noise processing, this issue is endemic to nearly all noise reduction algorithms applied in the spatial domain. A 3-D implementation of CPNR may help in this regard.

Ultimately, the hope is that the use of denoising algorithms will improve the performance of clinicians in detection, assessment, and quantification tasks. While this work has gone to great lengths to analyze numerical algorithm performance, it has not yet reflected upon observer performance effects. Observer performance studies needed to be conducted to validate the claims and predictions made using analytical metrics. Such studies are left to future endeavors.

## Appendix A: Synthesis of Digitized Slit and Edge Objects with System Blurring Effects

To predict the accuracy of MTF estimates generated from arbitrarily angled resolution test devices, a generalized model was developed for computer simulation purposes. Ideally, 1-D MTF analysis would be conducted using a Dirac delta line impulse object of the form

$$\delta_\ell(x, y) = \delta(x \cos \theta_0 + y \sin \theta_0 - \ell). \quad (\text{A.1})$$

The Dirac delta line impulse is alternatively defined in the following limit derived from the definition of an angled and shifted rectangular function:

$$\delta_\ell(x, y) = \lim_{\omega \rightarrow 0} \frac{1}{\omega} \text{rect}\left(\frac{x \cos \theta_0 + y \sin \theta_0 - \ell}{\omega}\right). \quad (\text{A.2})$$

The test signal is parameterized by width  $\omega$ , unit normal at angle  $\theta_0$ , and distance  $\ell$  from the origin in the direction of the unit normal. For small  $\omega$ , Eq. (A.2) approximates an ideal physical slit imaged using ideal parallel beam geometry (illustrated in Figure A.1). For sufficiently large  $\omega$ , the same model may be used to approximate an edge test function assuming proper assignment of  $\ell$  such that only a single edge is visible in the relevant field of view.

The rectangular function (square strip) of infinite extent  $f(x, y)$  is defined such that the volume per unit length in the “long” dimension is unity in order to ensure that, in the limit as  $\omega \rightarrow 0$ , the integral of the Dirac delta function [Eq. (A.2)] is also unity. Therefore, the unsampled, unblurred signal in the spatial domain is defined as

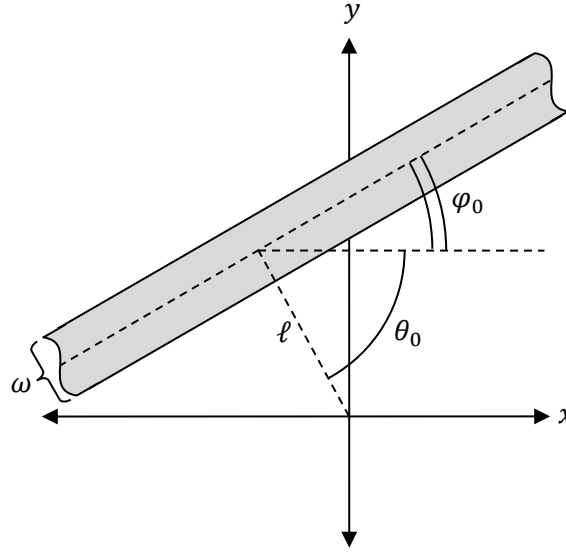


**Figure A.1: Depiction of variables used to define a resolution test object of finite width and infinite length cast onto a Cartesian coordinate system.**

$$f(x, y) = \frac{1}{\omega} \text{rect}\left(\frac{x \cos \theta_0 + y \sin \theta_0 - \ell}{\omega}\right). \quad (\text{A.3})$$

Modification of  $f(x, y)$  by some system PSF is modeled as the convolution of  $f(x, y)$  with the PSF to produce  $g(x, y)$ . To avoid the computational complexities associated with convolution, the signal is converted to its frequency space representation by the Fourier transform as outlined by the convolution theorem (\* denotes convolution):

$$\mathcal{F}_{2D}\{f * \text{PSF}\}(x, y)(u, v) = \mathcal{F}_{2D}\{g\}(x, y)(u, v) = G(u, v) = F(u, v) \text{MTF}(u, v). \quad (\text{A.4})$$

$F(u, v)$  is the FT of  $f(x, y)$ , and it is presented in expanded detail below:

$$F(u, v) = \text{sinc}\left(\frac{u\omega}{\cos \theta_0}\right) e^{\frac{2\pi i u \ell}{\cos \theta_0}} \frac{\delta(v - u \tan \theta_0)}{\cos \theta_0}. \quad (\text{A.5})$$

The Dirac delta line impulse in Eq. (A.5) may be modified for computational convenience:

[195]

$$F(u, v) = \text{sinc}\left(\frac{u\omega}{\cos\theta_0}\right) e^{-2\pi i u \ell / \cos\theta_0} \delta(v \cos\theta_0 - u \sin\theta_0). \quad (\text{A.6})$$

The sifting property of the Dirac delta impulse in Eq. (A.6) can be exploited to greatly simplify the equation, especially when converted to representation in polar coordinates:

$$F(\rho, \theta_0) = \text{sinc}(\rho\omega) e^{-2\pi i \rho \ell}. \quad (\text{A.7})$$

To incorporate the effects of system blur,  $F(\rho, \theta_0)$  must be modified by the MTF to produce  $G(\rho, \theta_0)$ . In turn,  $G(\rho, \theta_0)$  must undergo a 1-D inverse FT to return the problem to the spatial domain via

$$g(x, y) = \mathcal{F}_{1D}^{-1}\{G\}(\rho, \theta_0)(x, y) = \int_{-\infty}^{\infty} \text{sinc}(\rho\omega) \text{MTF}(\rho, \theta_0) e^{2\pi i \rho(x \cos\theta_0 + y \sin\theta_0 - \ell)} d\rho. \quad (\text{A.8})$$

It should be noted that the MTF in Eq. (A.8) involves all (linear) components of detector blur (including signal integration across finite pixel apertures). If the MTF of the system is expressed in analytical form, Eq. (A.8) lends itself readily to straightforward calculation. However, the MTF of real systems are typically computed from measured data which may lack a convenient analytical form. In either case, Simpson's rule for numerical integration can be used to conduct the 2-D inverse FT of  $G(\rho, \theta_0)$ . To verify the accuracy of this derivation, the inverse FT is performed without loss of generality by assuming unit MTF:

$$\begin{aligned} g(x, y) &= \int_{-\infty}^{\infty} \text{sinc}(\rho\omega) e^{2\pi i \rho(x \cos\theta_0 + y \sin\theta_0 - \ell)} d\rho \\ &= \frac{1}{\omega} \text{rect}\left(\frac{x \cos\theta_0 + y \sin\theta_0 - \ell}{\omega}\right) = f(x, y) \blacksquare \end{aligned} \quad (\text{A.9})$$

## Appendix B: Plane Wave Windowing, Sampling, and Integration Over a Rectangular Aperture

In this appendix, the formulation for a 2-D integrated, sampled, and windowed sinusoidal waveform is derived. Analysis begins with the definition of a continuous plane wave of infinite extent:

$$f(x, y) = A \cos[2\pi(u_0x + v_0y + \varphi)]. \quad (\text{B.1})$$

In Eq. (B.1),  $A$  is the sinusoid amplitude,  $u_0$  and  $v_0$  are the horizontal and vertical spatial frequencies (in cycles per unit distance), respectively;  $x$  and  $y$  are Cartesian coordinates in the spatial domain; and  $\varphi$  is the phase shift (in cycles). Such a sinusoid may be sampled on a 2-D digital lattice of infinite extent. The sampling step is modeled as the function

$$s(x, y) = \frac{1}{|\Delta x_s \Delta y_s|} \text{comb}\left(\frac{x}{\Delta x_s}, \frac{y}{\Delta y_s}\right) = \delta_s(x, y; \Delta x_s, \Delta y_s), \quad (\text{B.2})$$

which is referred to as a 2-D Dirac comb or Shah function with sample spacing  $\Delta x_s$  in the horizontal direction and  $\Delta y_s$  in the vertical direction. Multiplication of  $f(x, y)$  by  $s(x, y)$  is the discretization of the continuous function  $f(x, y)$ . However, since  $f(x, y)$  and  $s(x, y)$  are both infinite in extent, they must be windowed to permit practical analysis. This is accomplished through multiplication by the 2-D rectangular function

$$w(x, y) = \text{rect}\left(\frac{x - x_0}{X}, \frac{y - y_0}{Y}\right). \quad (\text{B.3})$$

The function  $w(x, y)$  is a rectangular window with width  $X$  and height  $Y$  centered at  $(x_0, y_0)$ .

In general, it is sufficient to assume a rectangular pixel aperture function defined as

$$a_p(x, y) = \frac{1}{\Delta x \Delta y} \text{rect}\left(\frac{x}{\Delta x}, \frac{y}{\Delta y}\right). \quad (\text{B.4})$$

The sampling aperture width  $\Delta x$  is made distinct from the horizontal sample spacing  $\Delta x_s$ , since the two values are not necessarily equal in all systems. The same distinction is made between aperture height  $\Delta y$  and vertical sample spacing  $\Delta y_s$ . The sampling aperture function is used to integrate  $f(x, y)$  via convolution in the spatial domain. This process is combined with the sampling and windowing steps to form the following equation which describes the digital representation of an integrated, sampled, and windowed 2-D sinusoid function in the spatial domain:

$$g(x, y) = [a_p(x, y) * f(x, y)]w(x, y)s(x, y). \quad (\text{B.5})$$

In Eq. **(B.5)**,  $*$  denotes convolution. Using substitution and expansion of the convolution,  $g(x, y)$  can be represented in a form which is easily programmed using a personal computer. This expansion is provided in detail in Appendix C. By the convolution theorem, Eq. **(B.5)** can be easily represented in the spatial frequency domain as

$$G(u, v) = \mathcal{F}_{2D}\{g\}(x, y)(u, v) = [A_p(u, v)F(u, v)] * W(u, v) * S(u, v). \quad (\text{B.6})$$

The FT of the sinusoidal function is

$$F(u, v) = \frac{A}{2} [e^{-2\pi i \varphi} \delta(u - u_0, v - v_0) + e^{2\pi i \varphi} \delta(u + u_0, v + v_0)]. \quad (\text{B.7})$$

Eq. **(B.7)** is the generalized form of the FT of a plane wave with arbitrary phase shift  $\varphi$ .  $F(u, v)$  is multiplied by the FT of the aperture function, represented in frequency space as

$$A_p(u, v) = \text{sinc}(\Delta x u, \Delta y v). \quad (\text{B.8})$$

If the sampling aperture in the spatial domain is very small (i.e.  $\Delta x$  and  $\Delta y$  approach zero such that  $a_p(x, y)$  approaches a Dirac Delta function), then  $A_p(u, v)$  approaches unity at all frequencies.<sup>1</sup> Otherwise,  $A_p(u, v)$  imposes a multiplicative decrease in signal

---

<sup>1</sup> In the text, it is assumed that the aperture function  $a_p(x, y) = \delta(x, y)$  unless otherwise noted.

amplitude according to Eq. **(B.8)**.  $G(u, v)$  is therefore characterized by the convolution of  $F(u, v)$  by  $S(u, v)$  and  $W(u, v)$  with multiplicative scaling by  $A_p(u, v)$ . For completeness,  $S(u, v)$  is defined here as the FT pair of  $s(x, y)$ :

$$S(u, v) = \text{comb}(\Delta x_s u, \Delta y_s v). \quad (\text{B.9})$$

In Eq. **(B.9)**, the scaling property of the FT has been implemented to yield  $S(u, v)$ . Convolution by  $S(u, v)$  replicates the function  $F(u, v)$  at regular intervals of  $1/\Delta x_s$  in the  $u$ -direction and  $1/\Delta y_s$  in the  $v$ -direction (which indicates the need for band-limitation of the imaged signal to avoid aliasing in accordance with the Nyquist-Shannon Sampling Theorem). Stated another way, any frequency with absolute value exceeding  $1/2\Delta x_s$  in the horizontal direction or  $1/2\Delta y_s$  in the vertical direction will be aliased since those frequencies will be undersampled. These replicates add constructively at all frequencies to produce a result which is replicated at the same intervals. Therefore, it is sufficient to measure the frequency response in the range of  $|u| \leq 1/2\Delta x_s$  and  $|v| \leq 1/2\Delta y_s$  for complete resolution characterization of the system. Although this measure will include the effects of aliasing when frequencies beyond the cutoff contribute to the measured signal, it nonetheless represents the real frequency content of the image. And since our work is not concerned with the realization of a presampled function, the real impact of sampling on the performance of imaging and image processing algorithms can be studied using these methods.

To complete the analysis, the window function is described in frequency space as

$$W(u, v) = |XY| \text{sinc}(Xu, Yv) e^{-2\pi i(x_0 u + y_0 v)}. \quad (\text{B.10})$$

After substituting values into Eq. **(B.6)**, the complete result in frequency space is



$$\begin{aligned}
G(u, v) = & \frac{A|XY|}{2} \operatorname{sinc}(\Delta x u, \Delta y v) [e^{-2\pi i \varphi} \delta(u - u_0, v - v_0) \\
& + e^{2\pi i \varphi} \delta(u + u_0, v + v_0)] * [\operatorname{sinc}(Xu, Yv) e^{-2\pi i(x_0 u + y_0 v)}] \quad (\text{B.11}) \\
& * \operatorname{comb}(\Delta x_s u, \Delta y_s v).
\end{aligned}$$

Solving for the convolution with the window function yields

$$\begin{aligned}
 G(u, v) = \frac{A|XY|}{2} & \left\{ e^{-2\pi i\varphi} \int_{-\infty}^{\infty} \int_{-\infty}^{\infty} \text{sinc}[\Delta x(u - \xi), \Delta y(v - \eta)] \delta(u - u_0 - \xi, v - v_0 - \eta) \text{sinc}(X\xi, Y\eta) e^{-2\pi i(x_0\xi + y_0\eta)} d\xi d\eta \right. \\
 & \left. + e^{2\pi i\varphi} \int_{-\infty}^{\infty} \int_{-\infty}^{\infty} \text{sinc}[\Delta x(u - \xi), \Delta y(v - \eta)] \delta(u + u_0 - \xi, v + v_0 - \eta) \text{sinc}(X\xi, Y\eta) e^{-2\pi i(x_0\xi + y_0\eta)} d\xi d\eta \right\} \\
 & * \text{comb}(\Delta x_s u, \Delta y_s v).
 \end{aligned}$$

(B.12)

The separability of functions in Eq. (B.12) yields

$$\begin{aligned}
 G(u, v) = \frac{A|XY|}{2} & \left\{ e^{-2\pi i\varphi} \int_{-\infty}^{\infty} \text{sinc}[\Delta x(u - \xi)] \delta(u - u_0 - \xi) \text{sinc}(X\xi) e^{-2\pi i x_0 \xi} d\xi \right. \\
 & \int_{-\infty}^{\infty} \text{sinc}[\Delta y(v - \eta)] \delta(v - v_0 - \eta) \text{sinc}(Y\eta) e^{-2\pi i y_0 \eta} d\eta + \\
 & e^{2\pi i\varphi} \int_{-\infty}^{\infty} \text{sinc}[\Delta x(u - \xi)] \delta(u + u_0 - \xi) \text{sinc}(X\xi) e^{-2\pi i x_0 \xi} d\xi \\
 & \left. \int_{-\infty}^{\infty} \text{sinc}[\Delta y(v - \eta)] \delta(v + v_0 - \eta) \text{sinc}(Y\eta) e^{-2\pi i y_0 \eta} d\eta \right\} \\
 & * \text{comb}(\Delta x_s u, \Delta y_s v).
 \end{aligned}$$

(B.13)

Because of the sifting property of the delta function in each integral, the problem is simplified:

$$\begin{aligned}
G(u, v) = & \frac{A|XY|}{2} \left\{ e^{-2\pi i \varphi} \operatorname{sinc}(\Delta x u_0, \Delta y v_0) \operatorname{sinc}[X(u - u_0), Y(v - v_0)] e^{-2\pi i x_0[(u - u_0) + (v - v_0)]} \right. \\
& + e^{2\pi i \varphi} \operatorname{sinc}(-\Delta x u_0, -\Delta y v_0) \operatorname{sinc}[X(u + u_0), Y(v + v_0)] e^{-2\pi i x_0[(u + u_0) + (v + v_0)]} \left. \right\} \\
& * \operatorname{comb}(\Delta x_s u, \Delta y_s v).
\end{aligned} \tag{B.14}$$

Using the “replicating property” of the comb function, Eq. (B.14) can be rewritten as

$$\begin{aligned}
G(u, v) = & \frac{A|XY|}{2|\Delta x_s \Delta y_s|} \left\{ e^{-2\pi i \varphi} \operatorname{sinc}(\Delta x u_0, \Delta y v_0) \right. \\
& \times \sum_{n=-\infty}^{\infty} \sum_{m=-\infty}^{\infty} \operatorname{sinc} \left[ X \left( u - u_0 - \frac{n}{\Delta x_s} \right), Y \left( v - v_0 - \frac{m}{\Delta y_s} \right) \right] e^{-2\pi i \left[ x_0 \left( u - u_0 - \frac{n}{\Delta x_s} \right) + y_0 \left( v - v_0 - \frac{m}{\Delta y_s} \right) \right]} \\
& + e^{2\pi i \varphi} \operatorname{sinc}(-\Delta x u_0, -\Delta y v_0) \\
& \times \sum_{n=-\infty}^{\infty} \sum_{m=-\infty}^{\infty} \operatorname{sinc} \left[ X \left( u + u_0 - \frac{n}{\Delta x_s} \right), Y \left( v + v_0 - \frac{m}{\Delta y_s} \right) \right] e^{-2\pi i \left[ x_0 \left( u + u_0 - \frac{n}{\Delta x_s} \right) + y_0 \left( v + v_0 - \frac{m}{\Delta y_s} \right) \right]} \left. \right\}.
\end{aligned} \tag{B.15}$$

The accuracy of the frequency space derivation can be tested by comparing its computation (and subsequent inverse FT) to the direct simulation of sinusoids in the spatial domain [Eq. (C.5)]. Due to Gibbs ringing artifact, the 2-D inverse FT of the above equation will contain some error near the boundaries of the window function  $w(x, y)$  when sinusoids at arbitrary frequencies are simulated. This error can be minimized by increasing the number of replicates  $n$  and  $m$ . Figure B.1 shows that the accuracy of Eq. (B.15) increases with the inclusion of more frequency space replicate pairs for sinusoids of arbitrary frequency.

Extensive efforts have been taken to represent Eq. (B.15) in frequency space in order to show the importance of sinusoid frequency selection. Since  $g(x, y)$  is discretized through sampling in the spatial domain,  $G(u, v)$  is also discretely represented at all combinations of the following frequencies (measured in cycles per image dimension):

$$u_d = \left\{ \left[ 1 - \left\lceil \frac{(N_x + 1)}{2} \right\rceil \right] / X, \left[ 2 - \left\lceil \frac{(N_x + 1)}{2} \right\rceil \right] / X, \dots, \left[ N_x - \left\lceil \frac{(N_x + 1)}{2} \right\rceil \right] / X \right\} \quad (\text{B.16})$$

$$v_d = \left\{ \left[ 1 - \left\lceil \frac{(N_y + 1)}{2} \right\rceil \right] / Y, \left[ 2 - \left\lceil \frac{(N_y + 1)}{2} \right\rceil \right] / Y, \dots, \left[ N_y - \left\lceil \frac{(N_y + 1)}{2} \right\rceil \right] / Y \right\} \quad (\text{B.17})$$

In Eqs. (B.16) and (B.17),  $u_d$  and  $v_d$  are the discretized spatial frequency locations,  $N_x$  and  $N_y$  are the respective horizontal and vertical image dimensions (measured in pixels), and  $\lceil \cdot \rceil$  is the ceiling operator. If the original sinusoid from Eq. (B.1) is not simulated with frequency  $(u_0, v_0)$  matching one of the specified frequencies  $(u_d, v_d)$ , then the digital representation of that sinusoid cannot be purely represented (i.e. the sinusoid will be represented as an ensemble of superimposed sinusoids of various other

frequencies). This is due to spectral leakage resulting from the window function. If the zeros of  $W(u, v)$  do not align with the sampling lattice, then the sinc function associated with the image window will produce non-zero values at frequencies not equal to  $(u_0, v_0)$ : this constitutes corruption of the representation of the pure sinusoidal signal. Figure B.1 demonstrates this phenomenon by comparing the error associated with computations of Eq. (B.15) for sinusoids at arbitrarily and judiciously selected frequencies.

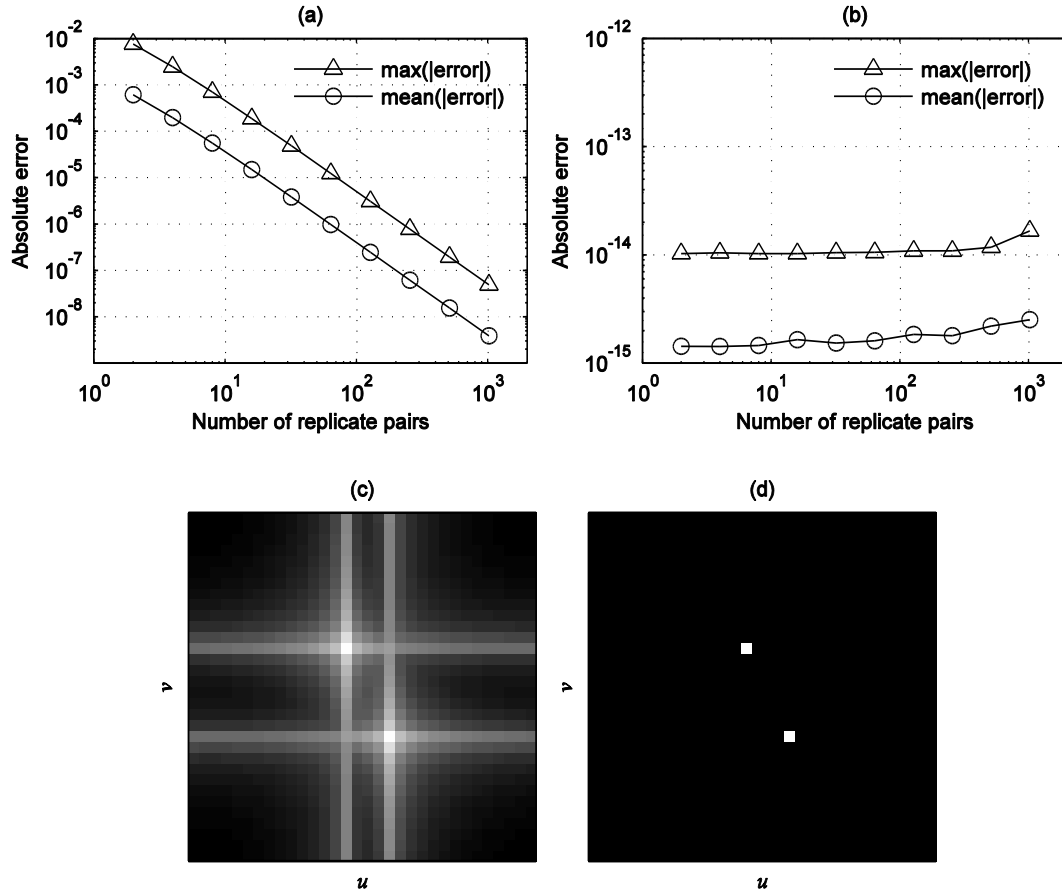


Figure B.1: Absolute error of sinusoid simulations using Eq. B.15.

Both figures show the absolute error associated with comparisons of the results from Eqs. (B.15) and (C.5) using the following parameters:  $A = 1$ ,  $\Delta x = \Delta y = 1$ ,  $\Delta x_s = \Delta y_s = 1$ ,  $X = Y = 32$ ,  $x_0 = y_0 = -0.5$ , and  $\varphi = 0$ . (a) Error associated with the simulation of a sinusoid with frequencies  $u_0 = 1/15$ ,  $v_0 = 2/15$  which do not belong in the subsets defined by Eqs. (B.16) and (B.17). Due to spectral leakage, the simulated sinusoid is not pure, and some error is associated with its simulation. (b) Error associated with the simulation of a sinusoid with frequencies  $u_0 = 1/16$ ,  $v_0 = 1/8$  which belong to the subsets defined by Eqs. (B.16) and (B.17). No spectral leakage has occurred, and the only source of error is due to the precision limits of the double number type. (c) FT of the sinusoid associated with (a). (d) FT of the sinusoid associated with (b). Plots (c) and (d) show logged intensities.

Corruption of the sinusoidal signal will also occur if either  $u_0$  or  $v_0$  is outside of the ranges specified by Eqs. (B.16) and (B.17), respectively. This would constitute a violation of the Nyquist criterion, and aliasing would occur. It is evident from Eq. (B.15) that a single sinusoid with frequency exceeding the cutoff takes on the alias found in the frequency space replicate which results from the convolution by  $S(u, v)$ . However, if the original input is band-limited in such a way that it satisfies the Nyquist criterion [i.e. its frequency exists within the ranges specified by Eqs. (B.16) and (B.17)], then it can be safely assumed that no aliasing has occurred, and the sampled signal sufficiently characterizes the presampled function. Since real medical images may contain the effects of undersampling and aliasing, this work is not necessarily concerned with uncovering the presampled function. The effects of undersampling and aliasing impact the performance of image processing algorithms, and these effects are of high importance in determining the real impact of image processing on real images.

## Appendix C: Expansion of Digital Plane Wave Representation in the Spatial Domain

The equation for an integrated, sampled, and windowed sinusoid has already been derived [Eq. (B.5)]. However, this equation does not readily lend itself to easy computation in its current form. In particular, the convolution in Eq. (B.5) must be expanded:

$$\begin{aligned} g(x, y) &= [a_p(x, y) * f(x, y)]w(x, y)s(x, y) \\ &= \int_{-\infty}^{\infty} \int_{-\infty}^{\infty} a_p(\xi, \eta) f(x - \xi, y - \eta) d\xi d\eta w(x, y) s(x, y). \end{aligned} \quad (\text{C.1})$$

Substitution of values from Appendix B yields

$$\begin{aligned} g(x, y) &= \int_{-\infty}^{\infty} \int_{-\infty}^{\infty} \frac{A}{\Delta x \Delta y} \text{rect}\left(\frac{\xi}{\Delta x}, \frac{\eta}{\Delta y}\right) \cos\{2\pi[u_0(x - \xi) + v_0(y - \eta) + \varphi]\} d\xi d\eta \\ &\quad \times \frac{1}{|\Delta x_s \Delta y_s|} \text{rect}\left(\frac{x - x_0}{X}, \frac{y - y_0}{Y}\right) \text{comb}\left(\frac{x}{\Delta x_s}, \frac{y}{\Delta y_s}\right). \end{aligned} \quad (\text{C.2})$$

The rect function within the integral modifies the integration bounds. Along with some simple rearrangement of terms, Eq. (C.2) is rewritten as

$$\begin{aligned} g(x, y) &= \frac{A}{\Delta x \Delta y |\Delta x_s \Delta y_s|} \text{rect}\left(\frac{x - x_0}{X}, \frac{y - y_0}{Y}\right) \text{comb}\left(\frac{x}{\Delta x_s}, \frac{y}{\Delta y_s}\right) \\ &\quad \times \int_{-\Delta y/2}^{\Delta y/2} \int_{-\Delta x/2}^{\Delta x/2} \cos\{2\pi[u_0(x - \xi) + v_0(y - \eta) + \varphi]\} d\xi d\eta. \end{aligned} \quad (\text{C.3})$$

By the integration rule for cosine,



$$\begin{aligned}
g(x, y) &= \frac{A}{2\pi\Delta x\Delta y|\Delta x_s\Delta y_s|} \text{rect}\left(\frac{x-x_0}{X}, \frac{y-y_0}{Y}\right) \text{comb}\left(\frac{x}{\Delta x_s}, \frac{y}{\Delta y_s}\right) \\
&\quad \times \int_{-\Delta y/2}^{\Delta y/2} \sin\{2\pi[u_0(x - \Delta x/2) + v_0(y - \eta) + \varphi]\} \\
&\quad - \sin\{2\pi[u_0(x + \Delta x/2) + v_0(y - \eta) + \varphi]\} d\eta.
\end{aligned} \tag{C.4}$$

And by the integration rule for sine,

$$\begin{aligned}
g(x, y) &= \frac{A}{4\pi^2\Delta x\Delta y|\Delta x_s\Delta y_s|} \text{rect}\left(\frac{x-x_0}{X}, \frac{y-y_0}{Y}\right) \text{comb}\left(\frac{x}{\Delta x_s}, \frac{y}{\Delta y_s}\right) \\
&\quad \times \langle -\cos\{2\pi[u_0(x - \Delta x/2) + v_0(y - \Delta y/2) + \varphi]\} \\
&\quad + \cos\{2\pi[u_0(x - \Delta x/2) + v_0(y + \Delta y/2) + \varphi]\} \\
&\quad + \cos\{2\pi[u_0(x + \Delta x/2) + v_0(y - \Delta y/2) + \varphi]\} \\
&\quad - \cos\{2\pi[u_0(x + \Delta x/2) + v_0(y + \Delta y/2) + \varphi]\} \rangle.
\end{aligned} \tag{C.5}$$

In the special case where  $u_0 = 0$ , the integral over  $d\xi$  reduces to unity yielding

$$\begin{aligned}
g(x, y) &= \frac{A}{2\pi\Delta x\Delta y|\Delta x_s\Delta y_s|} \text{rect}\left(\frac{x-x_0}{X}, \frac{y-y_0}{Y}\right) \text{comb}\left(\frac{x}{\Delta x_s}, \frac{y}{\Delta y_s}\right) \\
&\quad \times \langle \sin\{2\pi[v_0(y - \Delta y/2) + \varphi]\} - \sin\{2\pi[v_0(y + \Delta y/2) + \varphi]\} \rangle,
\end{aligned} \tag{C.6}$$

and in the special case where  $v_0 = 0$ , the integral over  $d\eta$  reduces to unity yielding

$$\begin{aligned}
g(x, y) &= \frac{A}{2\pi\Delta x\Delta y|\Delta x_s\Delta y_s|} \text{rect}\left(\frac{x-x_0}{X}, \frac{y-y_0}{Y}\right) \text{comb}\left(\frac{x}{\Delta x_s}, \frac{y}{\Delta y_s}\right) \\
&\quad \times \langle \sin\{2\pi[u_0(x - \Delta x/2) + \varphi]\} - \sin\{2\pi[u_0(x + \Delta x/2) + \varphi]\} \rangle.
\end{aligned} \tag{C.7}$$

## References

- [1] D. A. Schauer and O. W. Linton, "National Council on Radiation Protection and Measurements Report Shows Substantial Medical Exposure Increase," *Radiology* **253**, 293-296 (2009).
- [2] F. A. Mettler *et al.*, "Effective Doses in Radiology and Diagnostic Nuclear Medicine: A Catalog1," *Radiology* **248**, 254-263 (2008).
- [3] D. A. Schauer and O. W. Linton, "NCRP Report No. 160, Ionizing Radiation Exposure of the Population of the United States, medical exposure--are we doing less with more, and is there a role for health physicists?," *Health Phys.* **97**, 1-5 (2009).
- [4] D. J. Brenner and E. J. Hall, "Computed Tomography — An Increasing Source of Radiation Exposure," *N. Engl. J. Med.* **357**, 2277-2284 (2007).
- [5] American College of Radiology *et al.*, "Radiation Safety in Adult Medical Imaging - Image Wisely," *Vol. 2011*, (2010).
- [6] M. Goske *et al.*, "The 'Image Gently' campaign: increasing CT radiation dose awareness through a national education and awareness program," *Pediatr. Radiol.* **38**, 265-269 (2008).
- [7] M. J. Goske *et al.*, "The Image Gently Campaign: Working Together to Change Practice," *Am. J. Roentgenol.* **190**, 273-274 (2008).
- [8] S. Sherbini, "ALARA Principle," *Vol. 2011*, (2000).
- [9] D. Brenner *et al.*, "Estimated risks of radiation-induced fatal cancer from pediatric CT," *AJR Am. J. Roentgenol.* **176**, 289-296 (2001).
- [10] L. F. Donnelly *et al.*, "Minimizing radiation dose for pediatric body applications of single-detector helical CT: strategies at a large Children's Hospital," *AJR Am. J. Roentgenol.* **176**, 303-306 (2001).
- [11] X. Li *et al.*, "Patient-specific dose estimation for pediatric chest CT," *Med. Phys.* **35**, 5821-5828 (2008).
- [12] A. Paterson *et al.*, "Helical CT of the body: are settings adjusted for pediatric patients?," *AJR Am. J. Roentgenol.* **176**, 297-301 (2001).
- [13] J. T. Dobbins, III *et al.*, "Chest radiography: optimization of X-ray spectrum for cesium iodide-amorphous silicon flat-panel detector," *Radiology* **226**, 221-230 (2003).

- [14] E. Samei and M. J. Flynn, "An experimental comparison of detector performance for direct and indirect digital radiography systems," *Med. Phys.* **30**, 608-622 (2003).
- [15] M. K. Kalra *et al.*, "Techniques and Applications of Automatic Tube Current Modulation for CT," *Radiology* **233**, 649-657 (2004).
- [16] J. N. Althén, "Automatic tube-current modulation in CT—a comparison between different solutions," *Radiat. Prot. Dosimetry* **114**, 308-312 (2005).
- [17] D. Tack *et al.*, "Dose Reduction in Multidetector CT Using Attenuation-Based Online Tube Current Modulation," *Am. J. Roentgenol.* **181**, 331-334 (2003).
- [18] S. A. Graham *et al.*, "Compensators for dose and scatter management in cone-beam computed tomography," *Med. Phys.* **34**, 2691-2703 (2007).
- [19] N. Mail *et al.*, "The influence of bowtie filtration on cone-beam CT image quality," *Med. Phys.* **36**, 22-32 (2009).
- [20] R. C. Nelson *et al.*, "New iterative reconstruction techniques for cardiovascular computed tomography: How do they work, and what are the advantages and disadvantages?," *Journal of Cardiovascular Computed Tomography* **5**, 286-292 (2011).
- [21] A. K. Hara *et al.*, "Iterative Reconstruction Technique for Reducing Body Radiation Dose at CT: Feasibility Study," *Am. J. Roentgenol.* **193**, 764-771 (2009).
- [22] S. L. Brady *et al.*, "Characterization of adaptive statistical iterative reconstruction algorithm for dose reduction in CT: A pediatric oncology perspective," *Med. Phys.* **39**, 5520-5531 (2012).
- [23] P. Prakash *et al.*, "Diffuse lung disease: CT of the chest with adaptive statistical iterative reconstruction technique," *Radiology* **256**, 261-269 (2010).
- [24] C. Tomasi and R. Manduchi, "Bilateral filtering for gray and color images," *International Conference on Computer Vision* **6**, 839-846 (1998).
- [25] J. A. Lee *et al.*, "Edge-preserving filtering of images with low photon counts," *IEEE Transactions on Pattern Analysis and Machine Intelligence* **30**, 1014-1027 (2008).
- [26] A. Manduca *et al.*, "Projection space denoising with bilateral filtering and CT noise modeling for dose reduction in CT," *Med. Phys.* **36**, 4911-4919 (2009).
- [27] L. Yu *et al.*, "Sinogram smoothing with bilateral filtering for low-dose CT," *Proc. SPIE* **6913**, 691329-691328 (2008).

- [28] M. D. Harpen, "A computer simulation of wavelet noise reduction in computed tomography," *Med. Phys.* **26**, 1600-1606 (1999).
- [29] A. Pizurica *et al.*, "A versatile wavelet domain noise filtration technique for medical imaging," *IEEE Trans. Med. Imaging* **22**, 323-331 (2003).
- [30] Q. Wei and L. P. Clarke, "Adaptive multistage nonlinear filtering and wavelet for medical image enhancement," *IEEE International Conference on Image Processing* **3**, 711-715 (1994).
- [31] J. Zhong *et al.*, "Image denoising based on multiscale singularity detection for cone beam CT breast imaging," *Medical Imaging, IEEE Transactions on* **23**, 696-703 (2004).
- [32] A. Buades *et al.*, "A non-local algorithm for image denoising," **2**, 60-65 vol. 62 (2005).
- [33] Z. S. Kelm *et al.*, "Optimizing non-local means for denoising low dose CT," 662-665 (2009).
- [34] Z. Li *et al.*, "Adaptive non-local means filtering based on local noise level for CT denoising," *Proc. SPIE* **8313**, 83131H (2012).
- [35] C. A. Párraga *et al.*, "The human visual system is optimised for processing the spatial information in natural visual images," *Curr. Biol.* **10**, 35-38 (2000).
- [36] J. R. Wells and J. T. Dobbins, III, "Frequency response and distortion properties of nonlinear image processing algorithms and the importance of imaging context," *Med. Phys.* **40**, 091906 (2013).
- [37] P. Perona and J. Malik, "Scale-space and edge detection using anisotropic diffusion," *Pattern Analysis and Machine Intelligence, IEEE Transactions on* **12**, 629-639 (1990).
- [38] J. Q. Xia *et al.*, "Dedicated breast computed tomography: Volume image denoising via a partial-diffusion equation based technique," *Med. Phys.* **35**, 1950-1958 (2008).
- [39] J. Wang *et al.*, "Sinogram noise reduction for low-dose CT by statistics-based nonlinear filters," **5747**, 2058-2066 (2005).
- [40] A. H. Baydush *et al.*, "Improved Bayesian image estimation for digital chest radiography," *Med. Phys.* **24**, 539-545 (1997).
- [41] A. H. Baydush and C. E. Floyd, Jr., "Bayesian image estimation of digital chest radiography: interdependence of noise, resolution, and scatter fraction," *Med. Phys.* **22**, 1255-1261 (1995).

- [42] A. H. Baydush and C. E. Floyd, Jr., "Spatially varying Bayesian image estimation," *Acad. Radiol.* **3**, 129-136 (1996).
- [43] A. H. Baydush and C. E. Floyd, Jr., "Improved image quality in digital mammography with image processing," *Med. Phys.* **27**, 1503-1508 (2000).
- [44] C. E. Floyd, Jr. *et al.*, "Scatter compensation for digital chest radiography using maximum likelihood expectation maximization," *Invest. Radiol.* **28**, 427-433 (1993).
- [45] C. E. Floyd, Jr. *et al.*, "Bayesian restoration of chest radiographs. Scatter compensation with improved signal-to-noise ratio," *Invest. Radiol.* **29**, 904-910 (1994).
- [46] J. T. Dobbins, III and J. R. Wells, "Correlated-polarity noise reduction: feasibility of a new statistical approach to reduce image noise," *Proc. SPIE* **7961**, 79610A (2011).
- [47] J. T. Dobbins III, "Correlated-polarity noise reduction for dual-energy imaging," 82nd Scientific Assembly and Annual Meeting of the Radiological Society of North America (1996).
- [48] W. P. Segars *et al.*, "4D XCAT phantom for multimodality imaging research," *Med. Phys.* **37**, 4902-4915 (2010).
- [49] W. P. Segars, Ph.D. dissertation, Univeristy of North Carolina, 2001.
- [50] W. P. Segars *et al.*, "Realistic CT simulation using the 4D XCAT phantom," *Med. Phys.* **35**, 3800-3808 (2008).
- [51] J. M. Boone and J. A. Seibert, "An accurate method for computer-generating tungsten anode x-ray spectra from 30 to 140 kV," *Med. Phys.* **24**, 1661-1670 (1997).
- [52] M. J. Black *et al.*, "Robust anisotropic diffusion," *Image Processing, IEEE Transactions on* **7**, 421-432 (1998).
- [53] D. J. Moseley *et al.*, "Comparison of localization performance with implanted fiducial markers and cone-beam computed tomography for on-line image-guided radiotherapy of the prostate," *International Journal of Radiation Oncology\*Biolog\*Physics* **67**, 942-953 (2007).
- [54] H. W. Lilliefors, "On the Kolmogorov-Smirnov Test for Normality with Mean and Variance Unknown," *Journal of the American Statistical Association* **62**, 399-402 (1967).
- [55] P. R. Granfors and R. Aufrichtig, "Performance of a 41X41-cm<sup>2</sup> amorphous silicon flat panel x-ray detector for radiographic imaging applications," *Med. Phys.* **27**, 1324-1331 (2000).

- [56] C. E. Floyd, Jr. *et al.*, "Imaging characteristics of an amorphous silicon flat-panel detector for digital chest radiography," *Radiology* **218**, 683-688 (2001).
- [57] J. T. Dobbins, III, "Image quality metrics for digital systems," in *Handbook of medical imaging: volume 1. physics and psychophysics, Vol. 1*, edited by J. Beutel, H. L. Kundel and R. L. Van Metter (SPIE Press, Bellingham, Wa, 2000), pp. 161-222.
- [58] J. T. Dobbins, III *et al.*, "Intercomparison of methods for image quality characterization. II. Noise power spectrum," *Med. Phys.* **33**, 1466-1475 (2006).
- [59] J. T. Dobbins, III, "Effects of undersampling on the proper interpretation of modulation transfer function, noise power spectra, and noise equivalent quanta of digital imaging systems," *Med. Phys.* **22**, 171-181 (1995).
- [60] Z. Zhou *et al.*, "Techniques to improve the accuracy of noise power spectrum measurements in digital x-ray imaging based on background trends removal," *Med. Phys.* **38**, 1600-1610 (2011).
- [61] F. Durand and J. Dorsey, "Fast bilateral filtering for the display of high-dynamic-range images," *ACM Trans. Graph.* **21**, 257-266 (2002).
- [62] M. Elad, "On the origin of the bilateral filter and ways to improve it," *Image Processing, IEEE Transactions on* **11**, 1141-1151 (2002).
- [63] J. Du *et al.*, "Noise reduction in MR angiography with nonlinear anisotropic filtering," *J. Magn. Reson. Imaging* **19**, 632-639 (2004).
- [64] G. Gerig *et al.*, "Nonlinear anisotropic filtering of MRI data," *IEEE Trans. Med. Imaging* **11**, 221-232 (1992).
- [65] C. S. Anand and J. S. Sahambi, "Wavelet domain non-linear filtering for MRI denoising," *Magn. Reson. Imaging* **28**, 842-861 (2010).
- [66] W. C. K. Wong and A. C. S. Chung, "A nonlinear and non-iterative noise reduction technique for medical images: concept and methods comparison," *International Congress Series* **1268**, 171-176 (2004).
- [67] W. C. K. Wong *et al.*, "Trilateral filtering for biomedical images," *IEEE International Symposium on Biomedical Imaging: Nano to Macro* **1**, 820-823 (2004).
- [68] D. L. Donoho, "Nonlinear Solution of Linear Inverse Problems by Wavelet-Vaguelette Decomposition," *Applied and Computational Harmonic Analysis* **2**, 101-126 (1995).
- [69] D. L. Donoho and I. M. Johnstone, "Adapting to Unknown Smoothness via Wavelet Shrinkage," *Journal of the American Statistical Association* **90**, 1200-1224 (1995).

- [70] D. L. Donoho and I. M. Johnstone, "Minimax Estimation via Wavelet Shrinkage," *The Annals of Statistics* **26**, 879-921 (1998).
- [71] D. L. Donoho *et al.*, "Wavelet Shrinkage: Asymptopia?," *Journal of the Royal Statistical Society. Series B (Methodological)* **57**, 301-369 (1995).
- [72] D. L. Donoho and J. M. Johnstone, "Ideal spatial adaptation by wavelet shrinkage," *Biometrika* **81**, 425-455 (1994).
- [73] D. L. Donoho, "De-noising by soft-thresholding," *Information Theory, IEEE Transactions on* **41**, 613-627 (1995).
- [74] H. Rabbani *et al.*, "Wavelet-Domain Medical Image Denoising Using Bivariate Laplacian Mixture Model," *IEEE Trans. Biomed. Eng.* **56**, 2826-2837 (2009).
- [75] Y. Xiaofeng and F. Baowei, "A wavelet multiscale denoising algorithm for magnetic resonance (MR) images," *Measurement Science and Technology* **22**, 025803 (2011).
- [76] J. C. R. Giraldo *et al.*, "Comparative study of two image space noise reduction methods for computed tomography: Bilateral filter and nonlocal means," 3529-3532 (2009).
- [77] J. R. Wells and J. T. Dobbins, III, "Estimation of the two-dimensional presampled modulation transfer function of digital radiography devices using one-dimensional test objects," *Med. Phys.* **39**, 6148-6160 (2012).
- [78] J. R. Wells and J. T. Dobbins III, "TU-A-218-01: Estimation of the 2-D Presampled MTF of a Digital Flat Panel Detector Using an Edge Test Device," *Med. Phys.* **39**, 3894 (2012).
- [79] E. Samei *et al.*, "Intercomparison of methods for image quality characterization. I. Modulation transfer function," *Med. Phys.* **33**, 1454-1465 (2006).
- [80] H. Fujita *et al.*, "A simple method for determining the modulation transfer function in digital radiography," *IEEE Trans. Med. Imaging* **11**, 34-39 (1992).
- [81] E. Samei *et al.*, "A method for measuring the presampled MTF of digital radiographic systems using an edge test device," *Med. Phys.* **25**, 102-113 (1998).
- [82] J. T. Dobbins, III *et al.*, "DQE(f) of four generations of computed radiography acquisition devices," *Med. Phys.* **22**, 1581-1593 (1995).
- [83] K. A. Fetterly *et al.*, "Measurement of the presampled two-dimensional modulation transfer function of digital imaging systems," *Med. Phys.* **29**, 913-921 (2002).

- [84] W. Zhao and J. A. Rowlands, "Digital radiology using active matrix readout of amorphous selenium: Theoretical analysis of detective quantum efficiency," *Med. Phys.* **24**, 1819-1833 (1997).
- [85] A. Kuhls-Gilcrist *et al.*, "Accurate MTF measurement in digital radiography using noise response," *Med. Phys.* **37**, 724-735 (2010).
- [86] M. Båth *et al.*, "Method for determining the two-dimensional presampling modulation transfer function in digital radiography," *Proc. SPIE* **4320**, 268-279 (2001).
- [87] M. Båth *et al.*, "Determination of the two-dimensional detective quantum efficiency of a computed radiography system," *Med. Phys.* **30**, 3172-3182 (2003).
- [88] D. A. Reimann *et al.*, "Use of Wiener filtering in the measurement of the two-dimensional modulation transfer function," *Proc. SPIE* **3977**, 670-680 (2000).
- [89] D. A. Reimann *et al.*, "Evaluation of a New Technique for the Measurement of the Two Dimensional MTF of Digital Radiographic Systems," *Med. Phys.* **28**, 1187 (2001).
- [90] J. M. Boone, "Determination of the presampled MTF in computed tomography," *Med. Phys.* **28**, 356-360 (2001).
- [91] C. D. Bradford *et al.*, "Performance characteristics of a Kodak computed radiography system," *Med. Phys.* **26**, 27-37 (1999).
- [92] IEC publication, "Medical electrical equipment - Characteristics of digital x-ray imaging devices - Part 1: Determination of the detective quantum efficiency," *Vol. IEC 62220-1*, (Geneva, Switzerland, 2003).
- [93] IEC publication, "Medical diagnostic X-ray equipment - Radiation conditions for use in the determination of characteristics ", *Vol. IEC 61267*, (Geneva, Switzerland, 2005).
- [94] N. T. Ranger *et al.*, "Measurement of the detective quantum efficiency in digital detectors consistent with the IEC 62220-1 standard: practical considerations regarding the choice of filter material," *Med. Phys.* **32**, 2305-2311 (2005).
- [95] T. W. Ridler and S. Calvard, "Picture thresholding using an iterative selection method," *IEEE Trans. System., Man and Cybernetics* **8**, 630-632 (1978).
- [96] J. Canny, "A Computational Approach to Edge Detection," *IEEE Trans. Pattern Analysis and Machine Intelligence* **8**, 679-698 (1986).
- [97] A. D. Maidment and M. Albert, "Conditioning data for calculation of the modulation transfer function," *Med. Phys.* **30**, 248-253 (2003).



- [98] E. Buhr *et al.*, "Accuracy of a simple method for deriving the presampled modulation transfer function of a digital radiographic system from an edge image," *Med. Phys.* **30**, 2323-2331 (2003).
- [99] K. Doi *et al.*, "Truncation errors in calculating the MTF of radiographic screen-film systems from the line spread function," *Phys. Med. Biol.* **17**, 241-250 (1972).
- [100] J. Yorkston *et al.*, "Evaluation of the MTF for a-Si:H imaging arrays," *Proc. SPIE* **2163**, 141-149 (1994).
- [101] I. A. Cunningham and B. K. Reid, "Signal and noise in modulation transfer function determinations using the slit, wire, and edge techniques," *Med. Phys.* **19**, 1037-1044 (1992).
- [102] I. A. Cunningham, "Applied linear-systems theory," in *Handbook of medical imaging: Physics and psychophysics, Vol. 1*, edited by J. Beutel, H. L. Kundel and R. L. Van Metter (SPIE Press, Bellingham, WA, 2000), pp. 79-159.
- [103] I. A. Cunningham and A. Fenster, "A method for modulation transfer function determination from edge profiles with correction for finite-element differentiation," *Med. Phys.* **14**, 533-537 (1987).
- [104] J. C. Dainty and R. Shaw, *Image Science: principles, analysis and evaluation of photographic-type imaging processes*. (Academic Press, San Diego, CA, 1992).
- [105] S. E. Reichenbach *et al.*, "Characterizing digital image acquisition devices," *Optical Engineering* **30**, 170-177 (1991).
- [106] J. R. Wells and J. T. Dobbins, III, "Preliminary investigation of the frequency response and distortion properties of nonlinear image processing algorithms," *Proc. SPIE* **8668**, 86681H (2013).
- [107] I. Bankman, *Handbook of Medical Image Processing and Analysis*, 2nd ed. (Elsevier, Burlington, MA, 2009).
- [108] S. G. Armato *et al.*, "Anniversary Paper: Image processing and manipulation through the pages of Medical Physics," *Med. Phys.* **35**, 4488-4500 (2008).
- [109] A. Buades *et al.*, "A Review of Image Denoising Algorithms, with a New One," *Multiscale Modeling & Simulation* **4**, 490-530 (2005).
- [110] S. M. Smith and J. M. Brady, "SUSAN - A New Approach to Low Level Image Processing," *Int. J. Comput. Vision* **23**, 45-78 (1997).
- [111] R. J. Warp and J. T. Dobbins, III, "Quantitative evaluation of noise reduction strategies in dual-energy imaging," *Med. Phys.* **30**, 190-198 (2003).

- [112] I. Crooks and B. G. Fallone, "A novel algorithm for the edge detection and edge enhancement of medical images," *Med. Phys.* **20**, 993-998 (1993).
- [113] K. W. Leszczynski *et al.*, "The enhancement of radiotherapy verification images by an automated edge detection technique," *Med. Phys.* **19**, 611-621 (1992).
- [114] M. Stahl *et al.*, "Digital radiography enhancement by nonlinear multiscale processing," *Med. Phys.* **27**, 56-65 (2000).
- [115] P. T. Lauzier *et al.*, "Prior image constrained compressed sensing: Implementation and performance evaluation," *Med. Phys.* **39**, 66-80 (2012).
- [116] C. A. Mistretta, "Sub-Nyquist acquisition and constrained reconstruction in time resolved angiography," *Med. Phys.* **38**, 2975-2985 (2011).
- [117] S. Vandenberghe *et al.*, "Iterative reconstruction algorithms in nuclear medicine," *Comput. Med. Imaging Graph.* **25**, 105-111 (2001).
- [118] S. Richard *et al.*, "Towards task-based assessment of CT performance: System and object MTF across different reconstruction algorithms," *Med. Phys.* **39**, 4115-4122 (2012).
- [119] B. Chen *et al.*, "CT performance as a variable function of resolution, noise, and task property for iterative reconstructions," *Proc. SPIE* **8313**, 83131K (2012).
- [120] M. C. McDonald *et al.*, "A novel method to measure the zero-frequency DQE of a non-linear imaging system," *Proc. SPIE* **7961**, 79610C (2011).
- [121] M. C. McDonald *et al.*, "A robust approach to measuring the detective quantum efficiency of radiographic detectors in a clinical setting," *Proc. SPIE* **8313**, 831315 (2012).
- [122] G. H. Cottet and M. E. Ayyadi, "A Volterra type model for image processing," *IEEE Transactions on Image Processing* **7**, 292-303 (1998).
- [123] M. O. Franz and B. Schölkopf, "Implicit Wiener series for higher-order image analysis," in *Advances in Neural Information Processing Systems 17*, edited by L. K. Saul, Y. Weiss and L. Bottou (MIT Press, Cambridge, MA, 2005), pp. 465-472.
- [124] L. Carassale and A. Kareem, "Modeling Nonlinear Systems by Volterra Series," *Journal of Engineering Mechanics* **136**, 801-818 (2010).
- [125] J. A. Cherry, M.S. thesis, Carleton University, 1995.
- [126] Z. Q. Lang *et al.*, "Output frequency response function of nonlinear Volterra systems," *Automatica* **43**, 805-816 (2007).

- [127] M. Schetzen, *The Volterra and Wiener Theories of Nonlinear Systems*. (John Wiley & Sons, New York, 1980).
- [128] J. Arrillaga and N. R. Watson, *Power System Harmonics*, 2nd ed. (Wiley, West Sussex, England, 2003).
- [129] A. E. Emanuel, "Powers in nonsinusoidal situations-a review of definitions and physical meaning," *IEEE Transactions on Power Delivery* **5**, 1377-1389 (1990).
- [130] D. A. Gonzalez and J. C. McCall, "Design of Filters to Reduce Harmonic Distortion in Industrial Power Systems," *IEEE Transactions on Industry Applications* **23**, 504-511 (1987).
- [131] G.-Y. Hwang *et al.*, "Analysis of harmonic distortion due to uneven magnetic field in a microspeaker used for mobile phones," *IEEE Transactions on Magnetics* **38**, 2376-2378 (2002).
- [132] IEEE, "IEEE Recommended Practices and Requirements for Harmonic Control in Electrical Power Systems," in *IEEE Standard 519-1992, Vol. 519-1992*, (IEEE, New York, 1993).
- [133] G. D. MohanRaj, "A need to review total harmonic distortion measurement in power systems," *Power Quality* **1998**, 151-155 (1998).
- [134] D. Shmilovitz, "On the definition of total harmonic distortion and its effect on measurement interpretation," *IEEE Transactions on Power Delivery* **20**, 526-528 (2005).
- [135] R. B. Paranjape, "Fundamental enhancement techniques," in *Handbook of Medical Image Processing and Analysis*, edited by I. Bankman (Elsevier, Burlington, MA, 2009), pp. 3-18.
- [136] A. R. Sawant *et al.*, "Adaptive median filter algorithm to remove impulse noise in x-ray and CT images and speckle in ultrasound images," *Proc. SPIE* **3661**, 1263-1274 (1999).
- [137] A. Toprak and İ. Güler, "Impulse noise reduction in medical images with the use of switch mode fuzzy adaptive median filter," *Digital Signal Processing* **17**, 711-723 (2007).
- [138] Y. Zhao *et al.*, "Performance enhancement and analysis of an adaptive median filter," 2007 Second International Conference in Communications and Networking in China, Vols 1 and 2, 912-914 (2007).

- [139] C. H. McCollough *et al.*, "The phantom portion of the American College of Radiology (ACR) Computed Tomography (CT) accreditation program: Practical tips, artifact examples, and pitfalls to avoid," *Med. Phys.* **31**, 2423-2442 (2004).
- [140] D. J. Goodenough *et al.*, "Development of phantoms for spiral CT," *Comput. Med. Imaging Graph.* **22**, 247-255 (1998).
- [141] L. Fang and R. W. Picard, "Periodicity, directionality, and randomness: World features for image modeling and retrieval," *Pattern Analysis and Machine Intelligence, IEEE Transactions on* **18**, 722-733 (1996).
- [142] H.-C. Lin *et al.*, "Extracting periodicity of a regular texture based on autocorrelation functions," *Pattern Recognition Letters* **18**, 433-443 (1997).
- [143] J. Zhou *et al.*, "Scale-orientation histogram for texture image retrieval," *Pattern Recognition* **36**, 1061-1063 (2003).
- [144] H. F. Boehm *et al.*, "Automated classification of normal and pathologic pulmonary tissue by topological texture features extracted from multi-detector CT in 3D," *Eur. Radiol.* **18**, 2745-2755 (2008).
- [145] M. B. Huber *et al.*, "Performance of topological texture features to classify fibrotic interstitial lung disease patterns," *Med. Phys.* **38**, 2035-2044 (2011).
- [146] F. O. Bochud *et al.*, "Estimation of the noisy component of anatomical backgrounds," *Med. Phys.* **26**, 1365-1370 (1999).
- [147] A. E. Burgess *et al.*, "Human observer detection experiments with mammograms and power-law noise," *Med. Phys.* **28**, 419-437 (2001).
- [148] A. E. Burgess and P. F. Judy, "Signal detection in power-law noise: effect of spectrum exponents," *J. Opt. Soc. Am. A* **24**, B52-B60 (2007).
- [149] R. Smith-Bindman *et al.*, "Radiation dose associated with common computed tomography examinations and the associated lifetime attributable risk of cancer," *Arch. Intern. Med.* **169**, 2078-2086 (2009).
- [150] D. J. Brenner *et al.*, "Estimated Risks of Radiation-Induced Fatal Cancer from Pediatric CT," *Am. J. Roentgenol.* **176**, 289-296 (2001).
- [151] N. Howlader *et al.*, "SEER Cancer Statistics Review, 1975-2010," (National Cancer Institute, Bethesda, MD, 2013).
- [152] M. W. K. Kan *et al.*, "Radiation Dose From Cone Beam Computed Tomography for Image-Guided Radiation Therapy," *International Journal of Radiation Oncology\*Biophysics* **70**, 272-279 (2008).

- [153] L. A. Feldkamp *et al.*, "Practical Cone-Beam Algorithm," *Journal of the Optical Society of America A* **1**, 612-619 (1984).
- [154] J. T. Dobbins *et al.*, "Dose reduction in CT with correlated-polarity noise reduction: comparable image quality at half the dose with projection space processing," 866810-866810 (2013).
- [155] D. Zhang *et al.*, "Objective characterization of GE Discovery CT750 HD scanner: Gemstone spectral imaging mode," *Med. Phys.* **38**, 1178-1188 (2011).
- [156] Q. Xia, Dissertation, Duke University, 2007.
- [157] W. Jing *et al.*, "Multiscale Penalized Weighted Least-Squares Sinogram Restoration for Low-Dose X-Ray Computed Tomography," *Biomedical Engineering, IEEE Transactions on* **55**, 1022-1031 (2008).
- [158] W. Jing *et al.*, "Noise reduction for low-dose single-slice helical CT sinograms," *Nuclear Science, IEEE Transactions on* **53**, 1230-1237 (2006).
- [159] W. Jing *et al.*, "Penalized weighted least-squares approach to sinogram noise reduction and image reconstruction for low-dose X-ray computed tomography," *Medical Imaging, IEEE Transactions on* **25**, 1272-1283 (2006).
- [160] T. Li *et al.*, "Nonlinear sinogram smoothing for low-dose X-ray CT," *Nuclear Science, IEEE Transactions on* **51**, 2505-2513 (2004).
- [161] A. Maier *et al.*, "Three-dimensional anisotropic adaptive filtering of projection data for noise reduction in cone beam CT," *Med. Phys.* **38**, 5896-5909 (2011).
- [162] P. J. L. Riviere, "Penalized-likelihood sinogram smoothing for low-dose CT," *Med. Phys.* **32**, 1676-1683 (2005).
- [163] A. C. Kak and M. Slaney, *Principles of computerized tomographic imaging*. (Society for Industrial and Applied Mathematics, Philadelphia, 2001).
- [164] J. Zhao *et al.*, "Feldkamp-type reconstruction algorithms for spiral cone-beam CT with variable pitch," *Journal of X-Ray Science and Technology* **15**, 177-196 (2007).
- [165] H. Turbell, Linköpings Universitet, 2001.
- [166] G. J. Gang *et al.*, "Modeling and control of nonstationary noise characteristics in filtered-backprojection and penalized likelihood image reconstruction," 86681G-86681G (2013).
- [167] B. A. Groh *et al.*, "A performance comparison of flat-panel imager-based MV and kV cone-beam CT," *Med. Phys.* **29**, 967-975 (2002).

- [168] D. A. Jaffray *et al.*, "Flat-panel cone-beam computed tomography for image-guided radiation therapy," *International Journal of Radiation Oncology\*Biology\*Physics* **53**, 1337-1349 (2002).
- [169] E. Matsinos, "Current status of the CBCT project at Varian Medical Systems," **5745**, 340-351 (2005).
- [170] M. A. Hawkins *et al.*, "Assessment of residual error in liver position using kV cone-beam computed tomography for liver cancer high-precision radiation therapy," *International Journal of Radiation Oncology\*Biology\*Physics* **66**, 610-619 (2006).
- [171] T. Li *et al.*, "Four-dimensional cone-beam computed tomography using an on-board imager," *Med. Phys.* **33**, 3825-3833 (2006).
- [172] M. Oldham *et al.*, "Cone-beam-CT guided radiation therapy: A model for on-line application," *Radiother. Oncol.* **75**, 271.E271-271.E278 (2005).
- [173] M. K. Islam *et al.*, "Patient dose from kilovoltage cone beam computed tomography imaging in radiation therapy," *Med. Phys.* **33**, 1573-1582 (2006).
- [174] J. M. Schallenkamp *et al.*, "Prostate position relative to pelvic bony anatomy based on intraprostatic gold markers and electronic portal imaging," *Int. J. Radiat. Oncol. Biol. Phys.* **63**, 800-811 (2005).
- [175] N. Wen *et al.*, "Dose delivered from Varian's CBCT to patients receiving IMRT for prostate cancer," *Phys. Med. Biol.* **52**, 2267 (2007).
- [176] D. J. Brenner *et al.*, "Cancer risks attributable to low doses of ionizing radiation: Assessing what we really know," *Proceedings of the National Academy of Sciences* **100**, 13761-13766 (2003).
- [177] G. X. Ding and C. W. Coffey, "Radiation Dose From Kilovoltage Cone Beam Computed Tomography in an Image-Guided Radiotherapy Procedure," *International Journal of Radiation Oncology\*Biology\*Physics* **73**, 610-617 (2009).
- [178] H. C. Y. Cheng *et al.*, "Evaluation of Radiation Dose and Image Quality for the Varian Cone Beam Computed Tomography System," *International Journal of Radiation Oncology\*Biology\*Physics* **80**, 291-300 (2011).
- [179] G. X. Ding *et al.*, "Characteristics of kilovoltage x-ray beams used for cone-beam computed tomography in radiation therapy," *Phys. Med. Biol.* **52**, 1595 (2007).
- [180] G. X. Ding *et al.*, "Accurate patient dosimetry of kilovoltage cone-beam CT in radiation therapy," *Med. Phys.* **35**, 1135-1144 (2008).

- [181] D. J. Goodenough, "Catphan 504 Manual," (The Phantom Laboratory Incorporated, Salem, NY, 2012), pp. 32.
- [182] J. Wang *et al.*, "Dose reduction for kilovoltage cone-beam computed tomography in radiation therapy," *Phys. Med. Biol.* **53**, 2897 (2008).
- [183] J. T. Dobbins, III *et al.*, "Initial investigation into lower-cost CT for resource limited regions of the world," *Proc. SPIE* **7622**, 76223C (2010).
- [184] J. R. Wells *et al.*, "Refinement of motion correction strategies for lower-cost CT for under-resourced regions of the world," *Proc. SPIE* **7961**, 796133 (2011).
- [185] W. Giles *et al.*, "Crescent artifacts in cone-beam CT," *Med. Phys.* **38**, 2116-2121 (2011).
- [186] D. Zheng *et al.*, "Bow-tie wobble artifact: Effect of source assembly motion on cone-beam CT," *Med. Phys.* **38**, 2508-2514 (2011).
- [187] Y. Liu *et al.*, "Half-scan cone-beam CT fluoroscopy with multiple x-ray sources," *Med. Phys.* **28**, 1466-1471 (2001).
- [188] C. Maaß *et al.*, "A new weighting function to achieve high temporal resolution in circular cone-beam CT with shifted detectors," *Med. Phys.* **35**, 5898-5909 (2008).
- [189] G. Wang *et al.*, "Exact and Approximate Cone-Beam X-ray Microtomography," in *Modern Microscopies, Vol. 1*, edited by P. C. Cheng, P. P. Huang, J. L. Wu, G. Wang and H. Kim (Springer, New York, 1999), pp. 233-261.
- [190] D. L. Parker, "Optimal short scan convolution reconstruction for fan beam CT," *Med. Phys.* **9**, 254-257 (1982).
- [191] J. Hangyi *et al.*, "Techniques to improve the accuracy and to reduce the variance in noise power spectrum measurement," *Biomedical Engineering, IEEE Transactions on* **49**, 1270-1278 (2002).
- [192] J. M. Wilson *et al.*, "A methodology for image quality evaluation of advanced CT systems," *Med. Phys.* **40**, 031908 (2013).
- [193] R. Fazel *et al.*, "Exposure to Low-Dose Ionizing Radiation from Medical Imaging Procedures," *N. Engl. J. Med.* **361**, 849-857 (2009).
- [194] Y. Sagara *et al.*, "Abdominal CT: Comparison of Low-Dose CT With Adaptive Statistical Iterative Reconstruction and Routine-Dose CT With Filtered Back Projection in 53 Patients," *Am. J. Roentgenol.* **195**, 713-719 (2010).
- [195] R. L. Easton, *Fourier methods in imaging*. (Wiley, Chichester, West Sussex, 2010).

## Biography

Name Jered R Wells  
Date of Birth August 11, 1986  
Place of Birth Des Moines, Iowa, USA

### EDUCATION

Duke University Ph.D. in Medical Physics  
December 2013  
Durham, North Carolina, USA

Central College B.A. in Physics (*Summa Cum Laude*)  
May 2008  
Pella, Iowa, USA

### PEER-REVIEWED PUBLICATIONS

**J. R. Wells** and J. T. Dobbins, III, "Frequency response and distortion properties of nonlinear image processing algorithms and the importance of imaging context," *Med. Phys.* 40, 091906 (2013).

**J. R. Wells** and J. T. Dobbins, III, "Estimation of the two-dimensional presampled modulation transfer function of digital radiography devices using one-dimensional test objects," *Med. Phys.* 39, 6148-6160 (2012).

S. K. Lemieux, C. A. Smith-Bell, **J. R. Wells**, N. M. Ezerioha, J. S. Carpenter, D. L. Sparks and B. G. Schreurs, "Neurovascular changes measured by time-of-flight MR angiography in cholesterol-fed rabbits with cortical amyloid beta-peptide accumulation," *J. Magn. Reson. Imaging* 32, 306-314 (2010).

### CONFERENCE PROCEEDINGS AND PRESENTATIONS

**J. R. Wells**, W. P. Segars, and J. T. Dobbins, III, "TH-A-103-10: Improved segmentation of low-contrast fibroglandular structures in high-noise breast CT volumes for XCAT modeling," AAPM 55<sup>th</sup> Annual Meeting, Indianapolis, IN (2013). (Oral presentation)

**J. R. Wells** and J. T. Dobbins, III, "Preliminary investigation of the frequency response and distortion properties of nonlinear image processing algorithms," *Proc. SPIE* 8668, 86681H (2013). (Oral presentation)

J. T. Dobbins, III, **J. R. Wells**, and W. P. Segars, "Dose reduction in CT with correlated-polarity noise reduction: comparable image quality at half the dose with projection space processing," *Proc. SPIE* 8668, 866810 (2013). (Oral presentation)

**J. R. Wells** and J. T. Dobbins, III, "TU-A-218-01: Estimation of the 2-D Presampled MTF of a Digital Flat Panel Detector Using an Edge Test Device," AAPM 54<sup>th</sup> Annual Meeting, Charlotte, NC (2012). (Oral presentation)



**J. R. Wells**, W. P. Segars, C. J. N. Kigongo, and J. T. Dobbins, III, "Refinement of motion correction strategies for lower-cost CT for under-resourced regions of the world," Proc. SPIE 7961, 796133 (2011). (Poster presentation)

J. T. Dobbins, III and **J. R. Wells**, "Correlated-polarity noise reduction: feasibility of a new statistical approach to reduce image noise," Proc. SPIE 7961, 79610A (2011). (Oral presentation)

**J. R. Wells**, W. P. Segars, C. J. N. Kigongo, and J. T. Dobbins, III, "A new approach to motion correction applied to lower-cost CT for the developing world," 2010 Memphis Bioimaging Symposium, Memphis, TN (2010). (Poster presentation – **Honorable Mention**)

J. T. Dobbins, III, **J. R. Wells**, W. P. Segars, C. M. Li, and C. J. N. Kigongo, "Initial investigation into lower-cost CT for resource limited regions of the world," Proc. SPIE 7622, 76223C (2010). (Poster presentation)

#### **FELLOWSHIPS**

Carey E. Floyd Graduate Fellowship (Duke University, Medical Physics)	2012
NIH Cross-disciplinary Training Grant (TG32 EB007185)	2009-2011
PhD Fellowship (Duke University, Medical Physics)	2008-2009

#### **HONORS AND AWARDS**

Certificate in College Teaching (Duke University)	2013
Director's Award for Exemplary Service (Duke University, Medical Physics)	2013
Excellence in Teaching Assistantship (Duke University, Medical Physics)	2011, 2012

#### **PROFESSIONAL MEMBERSHIP**

Member, International Society for Optics and Photonics (SPIE)  
Member, American Association of Physicists in Medicine (AAPM)  
Member, Southeastern Chapter of the AAPM (SEAAPM)